

Resolving the ionizing photon budget crisis with JWST/NIRCam H II clumping constraints at $z \simeq 6$

DUNCAN AUSTIN ¹, THOMAS HARVEY ¹, CHRISTOPHER J. CONSELICE ¹, NATHAN J. ADAMS ¹, VADIM RUSAKOV ¹,
QIONG LI ¹, LEWI WESTCOTT ¹, CAIO GOOLSBY ¹, KAI MADGWICK¹, JAMES ARCIDIACONO¹, MASSIMO RICOTTI ²,
SOPHIE L. NEWMAN ³, LOUISE T. C. SEEYAVE ⁴, JAMES TRUSSLER ⁵, BRENDA FRYE ⁶, NORMAN A. GROGIN ⁷,
ROLF A. JANSEN ⁸, ANTON M. KOEKEMOER ⁷, NOR PIRZKAL ⁷, MICHAEL RUTKOWSKI ⁹ AND
ROGIER A. WINDHORST ⁸

¹Jodrell Bank Centre for Astrophysics, Alan Turing Building, University of Manchester, Oxford Road, Manchester M13 9PL, UK

²Department of Astronomy, University of Maryland, College Park, 20742, USA

³Institute of Cosmology and Gravitation, University of Portsmouth, Burnaby Road, Portsmouth PO1 3FX, UK

⁴Astronomy Centre, University of Sussex, Falmer, Brighton BN1 9QH, UK

⁵Center for Astrophysics, Harvard & Smithsonian, 60 Garden St., Cambridge MA 02138, USA

⁶Department of Astronomy/Steward Observatory, University of Arizona, 933 N Cherry Ave, Tucson, AZ, 85721-0009, USA

⁷Space Telescope Science Institute, 3700 San Martin Drive, Baltimore, MD 21218, USA

⁸School of Earth and Space Exploration, Arizona State University, Tempe, AZ 85287-1404, USA

⁹Minnesota Institute for Astrophysics, Minnesota State University, Mankato, MN 56001-6062, USA

ABSTRACT

We present a comprehensive study of the ionizing properties of 1721 galaxies at $5.6 < z < 6.5$ using deep JWST/NIRCam photometric imaging from the NEP, JADES, and PRIMER surveys spanning an unmasked area ~ 550 arcmin² across UV magnitudes $-22 \lesssim M_{\text{UV}} \lesssim -17.5$. Our 90% stellar mass complete sample suggests little relation of UV slope with magnitude, $\beta_{\text{UV}} = (-0.040 \pm 0.022)M_{\text{UV}} - 2.88_{-0.44}^{+0.43}$, implying $f_{\text{esc}}^{\text{LyC}} \simeq 5\%$ based on calibrations from the Low-redshift Lyman Continuum Survey (LzLCS). We measure a constant ionizing photon production efficiency with UV magnitude, $\log_{10}(\xi_{\text{ion},0}/\text{Hz erg}^{-1}) = -0.006_{-0.017}^{+0.019} M_{\text{UV}} + 25.05_{-0.34}^{+0.39}$, consistent with HST canonical values. The total production rate of photons escaping into the IGM is computed as $\log_{10}(\dot{n}_{\text{ion}}/s^{-1}\text{Mpc}^{-3}) = 50.31_{-0.06}^{+0.07}$, for $M_{\text{UV}} < -17$ galaxies from our star forming and smouldering UV luminosity functions (UVLFs), which differ in the faint-end slope ($\alpha_{\text{SFG}} = -2.2 \pm 0.2$; $\alpha_{\text{sm}} = -1.7 \pm 0.2$). Extrapolating to the latest UVLF turnover limits from the massive lensing galaxy cluster Abell S1063 ($M_{\text{UV,lim}} = -13.5$) implies that a recombination-weighted H II clumping factor $C_{\text{HII,rec}} = 6.2_{-2.1}^{+4.1}$ is required to produce fully stably reionized at $z \simeq 6$. A clumping factor of this magnitude resolves the ionizing photon budget crisis. Our methodology paves the way for indirect clumping measurements from galaxies which will provide insight into earlier stages of the EoR when the Ly α -forest becomes saturated and more direct quasar measurements become impossible.

Keywords: galaxies:high-redshift — galaxies:photometry — galaxies:intergalactic medium — cosmology:reionization

1. INTRODUCTION

The Epoch of Reionization (EoR) is the period between the formation of the first stars and galaxies and the complete ionization of the previously neutral intergalactic medium (IGM) by Lyman continuum (LyC) photons. Its midpoint is constrained to be $z = 7.7 \pm 0.7$ (Planck Collaboration et al. 2020), and observations of

the Gunn-Peterson (GP) trough (J. E. Gunn & B. A. Peterson 1965) and damping wings in quasar spectra define the end of the hydrogen EoR to be $z \sim 5 - 6$ (e.g. L. C. Keating et al. 2020; S. E. I. Bosman et al. 2022; L. C. Keating et al. 2024; Y. Zhu et al. 2024).

While the contribution of active galactic nuclei (AGN) to the total production rate of photons ionizing the IGM remains unclear (R. Maiolino et al. 2024; E. Lambrides et al. 2024; D. Jiang et al. 2025), simulations have shown that their contribution is subdominant ($\lesssim 10 - 30\%$;

L. Y. A. Yung et al. 2021; S. Asthana et al. 2024; P. Dayal et al. 2025) and that massive, short lived O/B main-sequence stars dominate the total production of ionizing photons from galaxies (e.g. J. Rosdahl et al. 2018; M. Trebitsch et al. 2021). In the early Universe, it has been proposed that globular clusters are the dominant source (M. Ricotti 2002; C.-C. He et al. 2020). To determine the total rate of photon injection into the IGM from star-forming galaxies, \dot{n}_{ion} , three main ingredients are required: 1) the UV luminosity function (UVLF; Φ_{UV}); 2) the rate (\dot{N}_{ion}) and efficiency (ξ_{ion}) of ionizing photon production; and 3) measurement of the LyC escape fraction, $f_{\text{esc}}^{\text{LyC}}$, defined as the fraction of LyC photons escaping the interstellar medium (ISM) of their host galaxies.

The UVLF in the EoR at $z > 6.5$ was measured using deep photometric imaging with the Hubble Space Telescope (HST; P. A. Oesch et al. 2014; R. J. Bouwens et al. 2015b; S. L. Finkelstein et al. 2015; D. J. McLeod et al. 2015, 2016; P. A. Oesch et al. 2018) and more recently with JWST/NIRCam (e.g. C. T. Donnan et al. 2023; Y. Harikane et al. 2023; N. J. Adams et al. 2024; C. T. Donnan et al. 2024; D. J. McLeod et al. 2024) down to $M_{\text{UV}} \simeq -17/18$ mag. Promising future avenues exploit the magnification from strong-lensing clusters in the Ultra Deep NIRSpect and NIRCam Observations before the Epoch of Reionization survey (UNCOVER; PIs: I. Labbe & R. Bezanson; PID: 2561; R. Bezanson et al. 2024) and Gravitational Lensing & NIRCam IMaging to Probe early galaxy formation and Sources of reionization (GLIMPSE; PIs: H. Atek & J. Chisholm; PID: 3293; H. Atek et al. 2025) programs. These surveys probe fainter magnitudes down to $M_{\text{UV}} \simeq -12$, albeit over increasingly small areas, and even though photometric candidates have been found down to $M_{\text{UV}} \sim -13.5$, for example in the Sunrise Arc (E. Vanzella et al. 2023), no strong evidence for a turnover has yet been found.

The ionizing photon production efficiency is an intrinsic galaxy property which is commonly calculated from the ratio of either the [O III] $\lambda 5007$ (K. Nakajima et al. 2016; M. Tang et al. 2019; Y. I. Izotov et al. 2021) or Balmer recombination lines with the UV luminosity, tracing the burstiness of star formation. Canonical values are taken to be $\log_{10}(\xi_{\text{ion}}/\text{Hz erg}^{-1}) = 25.2$ supported by measurements from the Hubble Ultra Deep Field (HUDF; B. E. Robertson et al. 2013), Spitzer/IRAC at $3.6 \mu\text{m}$ and $4.4 \mu\text{m}$ for $z = 4-5$ galaxies (R. J. Bouwens et al. 2016), and the MOSFIRE Deep Evolution Field (MOSDEF; M. Kriek et al. 2015; N. A. Reddy et al. 2018), although attenuation by dust may reduce observed values by $\sim 0.2 - 0.3$ dex (I. Shivaee

et al. 2018). Several studies have found an increasing trend of ξ_{ion} with redshift (e.g. S. L. Finkelstein et al. 2019; M. Stefanon et al. 2022; R. Begley et al. 2025a), where harder ionizing spectra and burstier star formation histories (SFHs) are expected. In addition, larger ξ_{ion} values have been observed in Ly α emitters (LAEs; J. Matthee et al. 2017; Y. Harikane et al. 2018; M. V. Maseda et al. 2020; Z. Chen et al. 2024; A. Saxena et al. 2024). Much current discussion in the literature surrounds the burstiness of UV luminous sources at $z \gtrsim 6$, with several studies suggesting a positive trend in $\xi_{\text{ion}} - M_{\text{UV}}$ such that fainter galaxies have larger ionizing photon production efficiencies (e.g. G. Prieto-Lyon et al. 2023; C. Simmonds et al. 2024a; M. Llerena et al. 2025). More recent studies, however, suggest that the enhanced selectability of faint bursty galaxies biases this trend, and that the underlying distribution is either flatter or negatively sloped such that brighter galaxies have larger ξ_{ion} values (e.g. R. Endsley et al. 2024; R. Begley et al. 2025a; A. J. Pahl et al. 2025a; C. Simmonds et al. 2024b).

The fraction and escape mechanisms of ionizing photons from the ISM and into the IGM is widely debated. Theories include escape from density bounded nebulae where small ISM neutral gas reservoirs become saturated by the large amount of ionizing photons (E. Zackrisson et al. 2013; K. Nakajima & M. Ouchi 2014; H. Katz et al. 2020) or escape via holes punched through the ISM either by outflows of stellar or AGN origin (S. Gazagnes et al. 2020; H. Katz et al. 2023a). Either way, these $f_{\text{esc}}^{\text{LyC}}$ values are challenging to measure in the EoR at $z \gtrsim 6$ due to the complete absorption of LyC photons by the ionized IGM along the line-of-sight. Promising indirect tracers of $f_{\text{esc}}^{\text{LyC}}$ exist, including from the Low-redshift Lyman Continuum Survey (LzLCS; S. R. Flury et al. 2022a,b), where β_{UV} measurements are seen to correlate with $f_{\text{esc}}^{\text{LyC}}$ (J. Chisholm et al. 2022), albeit with a large scatter. In addition to β_{UV} , trends of escape fraction have been observed with the [Mg II]- $\lambda\lambda 2796, 2804$ doublet (A. Henry et al. 2018; J. Chisholm et al. 2020; X. Xu et al. 2022; H. Katz et al. 2022), O_{32} ratios ([O III] $\lambda 5007$ /[O II] $\lambda\lambda 3726, 3728$, e.g. A. E. Jaskot & M. S. Oey 2013; K. Nakajima & M. Ouchi 2014; Y. I. Izotov et al. 2018a,b), Ly α velocity offset (A. Verhamme et al. 2015, 2017; Y. I. Izotov et al. 2020) or equivalent width (EW; C. C. Steidel et al. 2018; A. J. Pahl et al. 2021), [S II] deficits (F. Wang et al. 2019; B. Wang et al. 2021), and SFR surface density (Σ_{SFR} ; R. P. Naidu et al. 2020). Tracing $f_{\text{esc}}^{\text{LyC}}$ in the EoR is clearly a complex procedure, and modern advancements in deep learning methods have allowed for multivariate models to be built based on LzLCS observations at low-

redshift (A. E. Jaskot et al. 2024a,b) and the SPHINX simulation (J. Rosdahl et al. 2022; N. Choustikov et al. 2024a,b).

Even with conservative estimates for the average $f_{\text{esc}}^{\text{LyC}} \sim 10\%$ and $M_{\text{UV,lim}} \sim -16$ for SFGs at $z \gtrsim 6$, the high ξ_{ion} values measured by JWST imply that the Universe is fully reionized earlier than $z \simeq 6$ even without any contribution from AGN, leading to the so-called “ionizing photon budget problem” (J. B. Muñoz et al. 2024). One possible solution to this would be an increasingly clumpy IGM which would reduce the average recombination timescale meaning more ionizing photons are required to stably ionize the Universe at a given ionized hydrogen content, x_{HII} (e.g. F. B. Davies et al. 2024).

In this study, we use deep photometric data from JWST/NIRCam to produce samples of star-forming and smouldering¹⁰ galaxies at $5.6 < z < 6.5$, split by star-formation burstiness ($\Phi = \text{SFR}_{10\text{Myr}}/\text{SFR}_{100\text{Myr}}$) as measured by the Bagpipes SED fitting code (A. C. Carnall et al. 2018). Specifically, our smouldering sample is defined as galaxies with a recent downturn in recent star formation, i.e. $\Phi < 1$ or equivalently $\text{SFR}_{10\text{Myr}} < \text{SFR}_{100\text{Myr}}$. At these redshifts, the optical continuum is traced by F410M (the only medium band common to these blank fields) and the $\text{H}\alpha + [\text{NII}]$ emission line complex falls within F444W. $\dot{N}_{\text{ion}} - M_{\text{UV}}$ and $f_{\text{esc}}^{\text{LyC}} - M_{\text{UV}}$ scaling relations, as well as UVLFs, from each subsample are combined to calculate the total ionizing photon production rate, \dot{n}_{ion} .

We assume a flat Λ CDM cosmology with $H_0 = 70 \text{ kms}^{-1}\text{Mpc}^{-1}$, $\Omega_{\Lambda,0} = 0.7$ and $\Omega_{\text{m},0} = 0.3$ a helium mass fraction, $Y = 0.25$, and present-day cosmic baryon fraction $\Omega_{\text{b},0} = 0.05$. The AB magnitude system (J. B. Oke 1974; J. B. Oke & J. E. Gunn 1983) is used throughout.

2. DATA AND SAMPLE

2.1. EPOCHS-v2 data and surveys

In this work, we use deep photometric imaging from both JWST/NIRCam and HST/ACS WFC to produce a robust sample of galaxies at $5.6 < z < 6.5$. We use blank field JWST/NIRCam data, combined with ancillary HST/ACS WFC imaging, produced using the same GALFIND pipeline as those in the EPOCHS series (N. J. Adams et al. 2024; D. Austin et al. 2024; C. J. Conselice et al. 2025; T. Harvey et al. 2025), with cata-

logues and further description of the methods presented in the EPOCHS-v2 data release (Austin et al. in prep). In short, these catalogues provide forced photometry in $0.32''$ diameter circular apertures, with aperture corrections derived from WebbPSF PSFs (M. D. Perrin et al. 2012, 2014), with source detection and deblending performed by SExtractor (E. Bertin & S. Arnouts 1996) in a weighted stack of the JWST/NIRCam LW widebands (F277W+F356W+F444W). Photometric uncertainties are determined empirically from the local depth.

Five of the widest and deepest blank field areas with deep JWST/NIRCam photometry are used, covering $550''^2$ across UV magnitudes $-22 \lesssim M_{\text{UV}} \lesssim -17.5$. Note that we do not include data from the Cosmic Evolution Early Release Science (CEERS; PID: 13445; PI: S. Finkelstein M. B. Bagley et al. 2023a) or Next Generation Deep Extragalactic Exploratory Public (NGDEEP; PID 2079; PIs: Papovich, Pirzkal M. B. Bagley et al. 2023b) surveys since they do not include the F090W filter crucial for robust photometric redshift estimates at $z \simeq 6$.

The faint end is probed by data from the JWST Advanced Deep Extragalactic Survey (JADES; D. J. Eisenstein et al. 2023, see also A. J. Bunker et al. (2023) and K. N. Hainline et al. (2024)) in the Great Observatories Origins Deep Survey (GOODS) North ($78.6''^2$) and South ($123.5''^2$) fields, with the UVLF “knee” covered by North Ecliptic Pole Time Domain Field (NEP-TDF; R. A. Jansen & R. A. Windhorst 2018; R. O’Brien et al. 2024) imaging ($54.5''^2$) taken from the Prime Extragalactic Areas for Reionization and Lensing Science (PEARLS; PIDs: 1176, 2738; PIs: R. Windhorst & H. Hammel; R. A. Windhorst et al. 2023). The bright end data is dominated by PRIMER (PI: J. Dunlop, PID: 1837) in the Ultra Deep Survey (UDS; $163.7''^2$) and Cosmological Evolution Survey (COSMOS; $129.3''^2$).

Ancillary data from the Hubble Legacy Fields (HLF G. Illingworth et al. 2016; K. E. Whitaker et al. 2019) and the Cosmic Assembly Near-IR Deep Extragalactic Legacy Survey (CANDELS A. M. Koekemoer et al. 2011; N. A. Grogin et al. 2011) are used to provide optical coverage at $0.4 - 0.8\mu\text{m}$.

2.2. Sample selection criteria

To robustly select a sample of $5.6 < z < 6.5$ galaxies, we have modified the EPOCHS selection criteria from C. J. Conselice et al. (2025) to account for the fact that, post reionization, the Ly α break is no longer a step-function at $z \lesssim 6.5$; depending on the line-of-sight, some Lyman-series photons may remain unabsorbed by the fully ionized IGM. We run Eazy-py (G. B. Brammer et al. 2008) with the “fspi.larson” template set

¹⁰ Terminology adopted from J. A. A. Trussler et al. (2024). Note that their definition stems from NIRCam colours probing rest-optical emission lines, and not an estimate of star formation burstiness.

(R. L. Larson et al. 2023) to calculate fiducial photometric redshifts (both with redshift free as well as constrained at $z < 4.0$ for low-redshift comparisons), which includes the damped Ly α (DLA) photo- z correction procedure using the average N_{HI} column densities given in Y. Asada et al. (2025). A 10% minimum flux error is applied to the photometry during the SED fitting procedure. The sample selection criteria using the photo- z PDFs from Eazy-py are as follows.

1. All bands entirely bluewards of the Lyman limit at $\lambda_{\text{rest}} < 912 \text{ \AA}$ should be non-detected at the 2σ level and all bands entirely redwards of the Lyman limit but bluewards of Ly α should be $< 3\sigma$ detected
2. The first two bands entirely redwards of Lyman- α should be $> 8\sigma$ detected, and all other redwards widebands should be $> 3\sigma$ detected
3. The best-fitting EAZY template should be reasonably well fitting $\chi_{\text{red}}^2 < 3.0$, which is sufficiently better fitting than the low-redshift EAZY run, $\Delta\chi^2 = \chi_{z_{\text{max}}=4.0}^2 - \chi_{z_{\text{free}}}^2 > 4.0$
4. The best-fitting EAZY redshift PDF should be tightly constrained such that $> 60\%$ of the PDF lies within $\pm 0.1(1+z)$ of the redshift at maximum likelihood
5. SExtractor half light radii, $R_{50} > 45\text{mas}$ (1.5 pix) in every selection band (F277W, F356W, F444W) to remove any potential hot pixels
6. Unmasked in at least 2 ACS bands and 6 NIR-Cam bands, which must include F090W, F277W, F356W, F410M, and F444W

It is worth noting that we use the redshift of maximum likelihood as our photometric redshift, and that the wavelength limits of the photometric filters are taken to be the wavelengths at which there is 50% filter transmission. The band ordering surrounding the break used in selection criteria 1 and 2 is complicated by the extended nature of the F850LP filter transmission profile, which overlaps both F814W and F090W; we thus exclude F850LP from use in the sample selection criteria outlined above.

In addition to these criteria, we fit the sonora bobcat (M. Marley et al. 2021), cholla (T. Karalidi et al. 2021), diamondback (C. V. Morley et al. 2024), elf owl (S. Mukherjee et al. 2024) and LOWZ (A. M. Meisner et al. 2021) Y, L, and T-type brown dwarf templates using

the BD-Finder package¹¹, removing 18 suspected brown dwarfs with $\chi_{\text{BD,red}}^2 \lesssim \chi_{\text{gal,red}}^2$ which appear compact in the JWST/NIRCam cutouts. An improved procedure for brown dwarf removal, including a full proper-motion search, and morphological fitting for size estimates is expected in the EPOCHS-v2 release paper (Austin et al. in prep.). We remove 10 compact “little red dots” (LRDs) with red F277W – F444W > 0.7 colours (see e.g. J. E. Greene et al. 2024; V. Kokorev et al. 2024, for photometric LRD selection) from the sample, and an additional 18 spurious candidates are removed by eye, which largely fall within stellar diffraction spikes missed by our automated masking procedure. This leaves us with a final sample consisting of 1721 $5.6 < z < 6.5$ galaxies across $549.6'{}^2$ of unmasked sky area.

2.3. Photometric properties

2.3.1. Calculating UV properties

The rest-frame UV properties, including UV continuum slopes, β_{UV} , and absolute magnitudes, M_{UV} , for our $5.6 < z < 6.5$ galaxy sample are calculated directly from the rest-frame UV photometry rather than the best-fitting SED from either Eazy-py or Bagpipes in the same way as D. Austin et al. (2024). While this makes only a minor difference for measurements of M_{UV} , the SED fitting β_{UV} measurements are strongly impacted by the parameter space covered by the SED template set being fitted, excluding the extreme blue β_{UV} results seen at high redshift (e.g. F. Cullen et al. 2023; M. W. Topping et al. 2024; D. Austin et al. 2024; F. Cullen et al. 2024).

To calculate β_{UV} for our sample, we adopt the methodology from D. Austin et al. (2024), which fits a $f_{\lambda} \propto \lambda^{\beta_{\text{UV}}}$ power law to the photometric fluxes lying entirely within $1250 < \lambda_{\text{rest}}/\text{\AA} < 3000$, as determined by wavelengths corresponding to their upper and lower 50% filter throughput. We measure M_{UV} from these power law fits using a 100\AA -wide tophat filter centered at $\lambda_{\text{rest}} = 1500\text{\AA}$.

Since our β_{UV} measurements are used only for the calculation of $f_{\text{esc}}^{\text{LyC}}$, we do not correct our β_{UV} measurements for the biases discussed in D. Austin et al. (2024). While these biases may have an impact on the shape of our $\beta_{\text{UV}} - M_{\text{UV}}$ relation, the 8σ detection limit and availability of the F162M, F182M, and F210M medium band filters in a subset of our sample will limit this.

¹¹ <https://github.com/tHarvey303/BD-Finder>

2.3.2. SED fitting with Bagpipes

We perform Bayesian SED fitting with a modified version of `Bagpipes` v1.2.0 (A. C. Carnall et al. 2018)¹² adopting a Gaussian redshift prior centred on the “fspi.larson” `EaZy-py` redshift with width corresponding to $3\sigma_{z,\text{EAZY}}$, where $\sigma_{z,\text{EAZY}}$ is the standard deviation of the `EaZy-py` redshift PDF. We use `BPASS` v2.2.1 stellar population synthesis models (J. J. Eldridge et al. 2017; E. R. Stanway & J. J. Eldridge 2018) with an assumed P. Kroupa (2001) IMF and a standard D. Calzetti et al. (2000) dust attenuation curve with no additional dust contribution from birth clouds. The “continuity bursty” non-parametric star formation history (SFH) 6-bin prescription from J. Leja et al. (2019); S. Tacchella et al. (2022), with an additional low-age bin from 0 – 3 Myr and 3 – 10 Myr is included. We follow the prescription of A. K. Inoue et al. (2014) for the attenuation of Lyman-series photons by the IGM. Log-linear priors are set for the dust attenuation, $A_V \in [10^{-4}, 10^2]$, and metallicity, $Z \in [10^{-3}, 3]$, and a flat uniform prior on the logarithm of the ionization parameter ($-4 < \log U < 0$) is assumed. The upper limit of this $\log U$ range is expanded relative to the default `Bagpipes` BC03 setup informed by `CLOUDY` modelling (G. J. Ferland et al. 2017).

Since the aperture fluxes are input into `Bagpipes`, the output M_{UV} and M_* properties require an extended source correction. This factor is computed as the ratio of the `SExtractor` “AUTO_FLUX” to “APER_FLUX” in the reddest F444W band, and is clipped to the range (1, 10). This prevents over-correction in cases where `SExtractor` produces catastrophic R. G. Kron (1980) aperture sizes, while also ensuring that fluxes for compact, point-like sources are not reduced.

2.4. Spectroscopic comparison

To determine the robustness of our photometric redshifts and sample selection procedure, we compile a PRISM/CLEAR spectroscopic catalogue from the most up-to-date version (v4.2) of the Dawn JWST Archive (DJA)¹³ by cross-matching our photometric catalogue to sources with “grade 3” (i.e. the highest quality) with a maximum $0.3''$ separation. Several programs comprise our spectroscopic dataset, including from JADES (PI: N. Lützgendorf; PIDs: GTOs 1210, 1212, 1286 (GOODS-South), 1214 (COSMOS), 1215 (UDS) + PI: K. Isaak; PID: GTO 1211 (GOODS-North; M. V. Maseda et al. 2024) + PI: D. Eisenstein; PIDs:

GTO 1180 (GOODS-South; F. D’Eugenio et al. 2025), 1181 (GOODS-North), GO 3215 (D. J. Eisenstein et al. 2023)), UDS CAPERS (PID: GO 6368, PI: M. Dickinson) and RUBIES (PID: GO 4233; PI: A. de Graaff; A. de Graaff et al. 2024), COSMOS DDT 6585 (PI: D. Coulter), GO 2565 (PI: K. Glazebrook; T. Nanayakkara et al. 2025) in COSMOS and UDS, as well as DDT 6541 (PI: E. Egami) and GO 2198 (PI: L. Barrufet; L. Barrufet et al. 2025) in GOODS-South. No spectroscopic observations with JWST/NIRSpec are available in the NEP field.

A comparison of photometric and spectroscopic redshifts is presented in Figure 1. Our full catalogue has a total 2725 cross-matches across the entire redshift range, with 1169 in UDS, 427 in COSMOS, 355 in GOODS-North, and 774 in GOODS-South. Of these, 39 make our $5.6 < z < 6.5$ selection criteria as outlined in subsection 2.2 (8 in UDS, 4 in COSMOS, 4 in GOODS-North, and 23 in GOODS-South). There are 102 PRISM/CLEAR spectra in the full catalogue at $5.6 < z < 6.5$, although after cropping to just those sources with rest-frame UV $\text{SNR}_{\text{F115W}} > \{8, 10\}$, 44 and 39 spectra are retained respectively. This implies a $\gtrsim 90\%$ completeness level for our sample which is primarily selected with an 8.0σ detection limit redwards of $\text{Ly}\alpha$, however this is strongly dependent on the selection function for the highly incomplete spectroscopic sample, and hence this number should perhaps be loosely interpreted. A more thorough discussion regarding the completeness of our sample is presented in subsection 2.6.

We quantify the robustness of our photometric redshift estimates by computing both the normalized median absolute deviation (NMAD; $\text{NMAD} = 1.483 \times \text{median}(|\Delta z / (1 + z_s)|)$, where $\Delta z = z_p - z_s$) and the outlier fraction, f_{out} , defined as the fraction of galaxies with $|\Delta z / (1 + z_s)| > 0.15$. As can be seen in Figure 1, our sample has $f_{\text{out}} = 5.1\%$ and $\text{NMAD} = 0.003$. We note that just a small change in the photo- z posterior for the COSMOS source at $(z_s, z_p) \simeq (4.8, 5.6)$ towards lower photo- z would halve our f_{out} value as a result of our small sample size.

We find $f_{\text{out}} = 28.3\%$ and $\text{NMAD} = 0.016$ for our catalogue cropped to $\text{SNR}_{\text{F444W}} > 8.0$, and $f_{\text{out}} = 1.5\%$ and $\text{NMAD} = 0.004$ at $5.6 < z_s < 6.5$. These photo- z estimates are clearly better suited to higher redshift ($z \gtrsim 5$) studies. Improving lower-redshift estimates would require additional bluer filters either from *HST* or ground-based optical instruments such as Canada-France-Hawaii Telescope’s (CFHT) MegaCam (O. Boulade et al. 2003) or Subaru’s HyperSuprimeCam (HSC; S. Miyazaki et al. 2018; Y. Komiyama et al. 2018).

¹² This now includes a prescription for $\xi_{\text{ion},0}$ and $\dot{N}_{\text{ion},0}$, among other more minor updates, and is available at <https://github.com/tHarvey303/bagpipes>.

¹³ <https://dawn-cph.github.io/dja/>

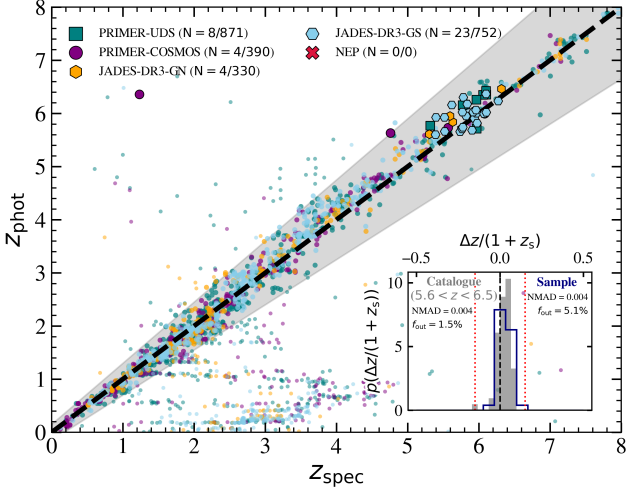


Figure 1. Comparison of Eazy-py photo- z 's derived from the R. L. Larson et al. (2023) template set with spec- z 's collated from the DJA (v4.2). Colours indicate the photometric origin survey, where the larger markers show galaxies that are selected in the photometric sample, of which there are 39. The lower right inset panel shows the probability distribution in $\Delta z/(1+z_s)$ for the catalogue (shaded grey) and sample (navy blue outline), with NMAD and outlier fraction (defined as $|\Delta z/(1+z_s)| > 0.15$; dotted red lines in inset, and shaded grey in main plot) displayed. The $z_p = z_s$ line is shown in dashed black.

2.5. Bursty and mini-quenched subsamples

We divide our sample into both “star forming” and “smouldering” subsamples to analyze the contribution of each to reionization independently by the inferred *Bagpipes* star formation burstiness, $\Phi = \text{SFR}_{10}/\text{SFR}_{100}$, such that SFGs have $\Phi > 1$ (comprising 62% of the full sample) and vice-versa for smouldering galaxies. In Figure 2, we show example *Bagpipes* SED fitting outputs for star forming (left) and smouldering (right) galaxies taken from the JADES GOODS-South (our “East” imaging data) survey.

The relation between our burstiness and $\xi_{\text{ion},0}$ estimates is clear from these two systems, where the source in the left-panel with larger $\xi_{\text{ion},0}$ has a stronger upturn in its recent star formation. Converting the SFRs measured directly from the $\text{H}\alpha$ and UV continuum luminosities combined with the conversion factors in R. C. Kennicutt (1998) to a burstiness estimate, $\Phi_{\text{H}\alpha/\text{UV}} = \text{SFR}_{\text{H}\alpha}/\text{SFR}_{\text{UV}}$, yields an exact relation with $\xi_{\text{ion},0}$ given by $\log_{10}(\xi_{\text{ion},0}/\text{Hz erg}^{-1}) = 25.11 + \log_{10}(\Phi_{\text{H}\alpha/\text{UV}})$.

2.6. Sample completeness

We use a single realization of the JWST Extragalactic Mock Catalog (JAGUAR; C. C. Williams et al. 2018) to assess the completeness of our sample in terms of

both M_{UV} and stellar mass, M_* . The relevant catalogue fluxes are scattered by 1σ mock photometric errors determined from the median depth in each band in each survey with a 10% minimum flux error as per our real photometric catalogues. For the JADES-GS survey we repeat this procedure for the deeper JADES-DR1 survey area and JOF which contains deep medium band imaging. Since the PRIMER-UDS and PRIMER-COSMOS fields have tiered NIRCcam exposure times we divide these surveys into Deep and Wide regions, producing a separate catalogue for each.

We run our catalogues through Eazy-py and the following selection procedure (excluding the masking criteria) outlined in subsection 2.2, with M_{UV} and M_* completeness curves for each survey shown in Figure 3. It is noteworthy that we do not determine stellar masses using our *Bagpipes* setup due to computational limitations; recovered *BPASS* stellar masses may show a systematic difference compared to the JAGUAR masses which are determined from *BEAGLE* templates as a result of a differing assumed IMF's (JAGUAR assumes G. Chabrier (2003) compared to the *Bagpipes* P. Kroupa (2001) IMF), SFHs, or assumed dust content.

Assuming that the stellar masses are robustly recovered, we find that our photometric sample is 90% mass complete between $\log_{10}(M_*/M_\odot) = 8.1$ (JADES-DR1 and JOF) and $\log_{10}(M_*/M_\odot) = 9.3$ (PRIMER-UDS Wide). The more step-function like M_{UV} completeness curves show that we are 90% complete between $M_{\text{UV}} = -17.6$ (JADES-DR1 and JOF) and $M_{\text{UV}} = -19.7$ (PRIMER-UDS and PRIMER-COSMOS Wide regions). All scaling relations in this work (presented in subsection 3.3, subsection 4.3, and subsection 4.2) are computed with a 90% stellar mass complete sample as in C. Simmonds et al. (2024b) to ensure the relations remain unbiased from faint blue galaxies bursting into the selected sample.

3. THE IONIZING PHOTON PRODUCTION EFFICIENCY

3.1. Calculating ξ_{ion}

To determine the contribution of our galaxy sample to reionization, it is useful to compute both the ionizing photon production rate,

$$\dot{N}_{\text{ion}} = \frac{7.28 \times 10^{11}}{(1 - f_{\text{esc}}^{\text{LyC}})} L_{\text{H}\alpha} \quad [\text{Hz}], \quad (1)$$

and efficiency,

$$\xi_{\text{ion}} = \frac{\dot{N}_{\text{ion}}}{L_{\nu,\text{UV}}} \quad [\text{Hz erg}^{-1}], \quad (2)$$

where $L_{\text{H}\alpha}$ is the $\text{H}\alpha$ luminosity and $L_{\nu,\text{UV}}$ is the UV continuum luminosity density, which are both dust cor-

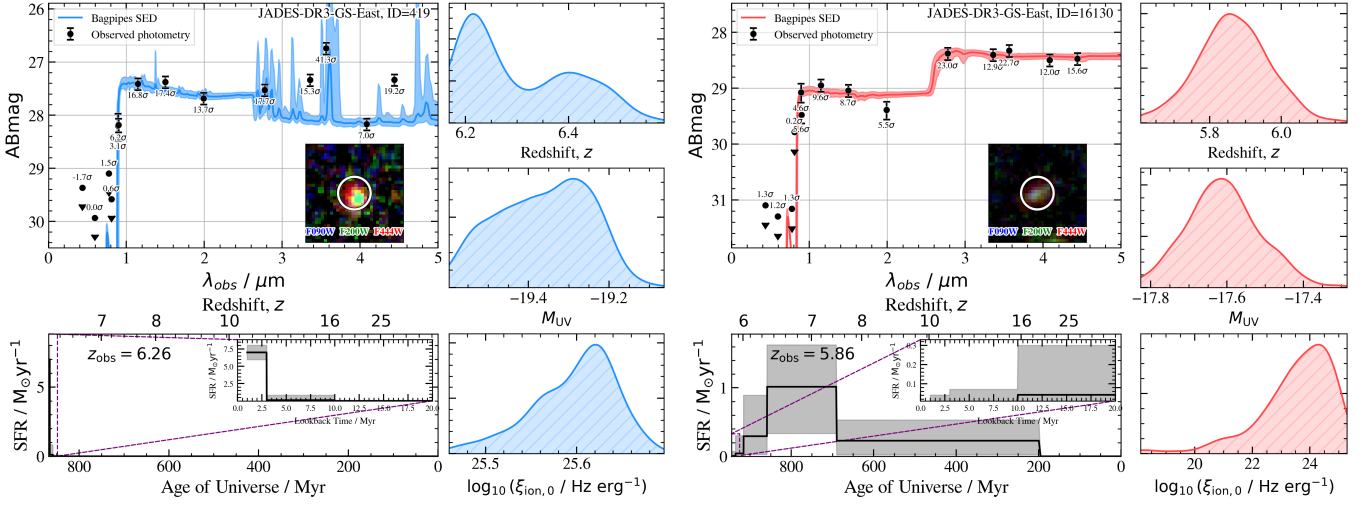


Figure 2. Example SED fits for star forming (left figure, light blue) and smouldering galaxies (right figure, light red) in the JADES GOODS-South (within our “East” imaging) using the fiducial *Bagpipes* setup as outlined in subsection 2.3.2. In the main panel of each figure, we show as the best-fit SED with shaded 16th – 84th percentiles. An F090W/F200W/F444W false-colour cutout is shown in the lower right. The photometric magnitudes and SNRs are shown for each observed band; fluxes with SNR < 2 are shown as upper limits. Posterior redshift, M_{UV} , and $\xi_{ion,0}$ PDFs are shown in the right hand panels and the star formation histories are shown in the lower left.

rected. The conversion factor in Equation 1 assumes case B recombination and a standard nebular electron temperature and density (see D. E. Osterbrock & G. J. Ferland 2006). These properties, however, are not independent of f_{esc}^{LyC} and it is more common to instead compute \dot{N}_{ion} and ξ_{ion} whilst assuming $f_{esc}^{LyC} = 0$, such that

$$\dot{N}_{ion,0} = (1 - f_{esc}^{LyC})\dot{N}_{ion}; \quad \xi_{ion,0} = (1 - f_{esc}^{LyC})\xi_{ion}. \quad (3)$$

Our modified *Bagpipes* calculates both $\xi_{ion,0}$ and $\dot{N}_{ion,0}$ for each source from the full posterior fitting distributions, assuming $f_{esc}^{LyC} = 0$. To calculate the rates/efficiencies of escaping ionizing photon production, we must multiply these observed (f_{esc}^{LyC} independent, but dust corrected) values output by *Bagpipes* by a factor $f_{esc}^{LyC}/(1 - f_{esc}^{LyC})$. In addition, we note that we also perform extended source corrections for $\dot{N}_{ion,0}$ in the same manner as the stellar mass correction factors explained in subsection 2.3.2. This $\dot{N}_{ion,0}$ is not to be confused with the *total* rate of ionizing photon production, \dot{n}_{ion} , introduced in section 4 and given by Equation 6.

3.2. Robustness of our *Bagpipes* $\xi_{ion,0}$ results

We test the priors for our fiducial *Bagpipes* setup explained above, finding that the possible values for $\xi_{ion,0}$ strongly depend upon both the SPS model used and the SFH. In the left-hand panel of Figure 4 we show the *Bagpipes* priors for the setup used in this work (orange red) and compare to the priors from two additional setups. The first alternative setup assumes a BC03 SPS

and “continuity bursty” SFH without the low-age bins (sea green), whereas the second adopts a BPASS SPS with lognormal SFH (blue). All other fiducial parameters remain fixed. It is apparent that while the stellar emission from our fiducial *Bagpipes* setup does the best, the intrinsic values still cannot match the large $\langle \log_{10}(\xi_{ion}/\text{Hz erg}^{-1}) \rangle = 25.8 \pm 0.14$ measured for lensed galaxies in the UNCOVER survey at $6 < z < 8$ with $-17 < M_{UV} < -15$ by H. Atek et al. (2024) due to the limited parameter space explored by the stellar template set run through CLOUDY.

To determine the robustness of our individual ξ_{ion} measurements, we produce a secondary spectroscopic catalogue from v4.2 of the DJA, finding 663 “grade 3” PRISM/CLEAR spectra at $5.6 < z < 6.5$. We perform continuum SNR cuts at the rest-frame $H\alpha$ wavelength at 2σ as well as a 5σ cut at $\lambda_{rest} = 1500 \text{ \AA}$, leaving 83 remaining spectra, 8 of which fail the selection criteria outlined in subsection 2.2. The $H\alpha$ lines in these 75 spectra were fit with a Gaussian profile using the *specFitMSA*¹⁴ python package. UV magnitudes were calculated using the same tophat filter as for our photometry to determine *observed* (i.e. not dust corrected) ξ_{ion} values spectroscopically.

A comparison of spectroscopic and photometric *observed* $\xi_{ion,0}$ measurements are shown in the right-hand panel of Figure 4, where we additionally remove 4 sources with broad $H\alpha$. The intrinsic $\xi_{ion,0}$ upper prior

¹⁴ <https://github.com/vadimrusakov/specFitMSA>

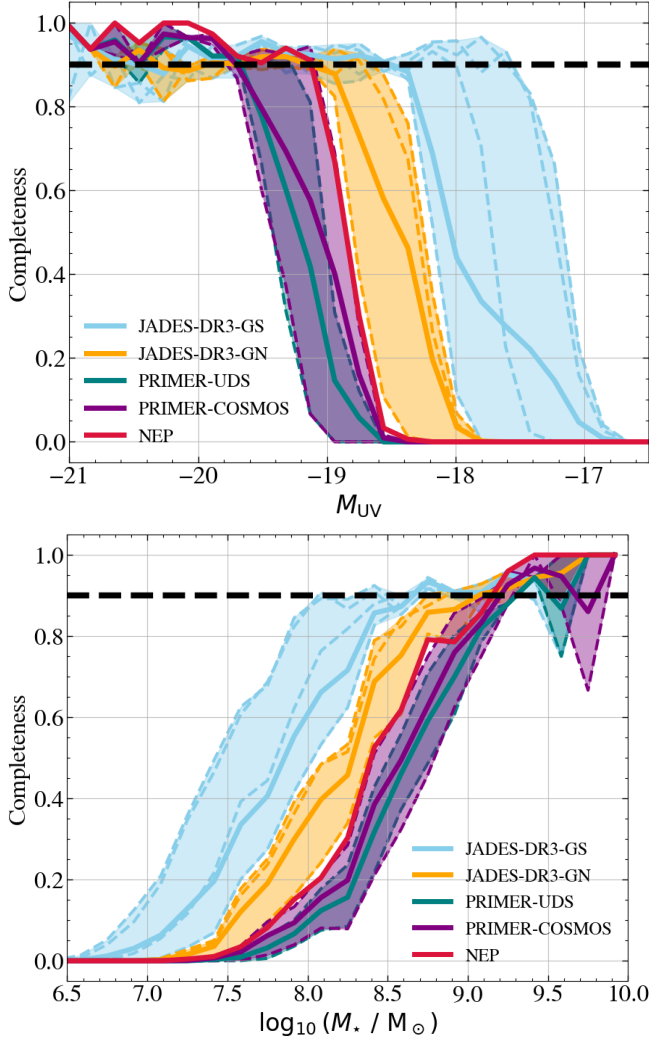


Figure 3. Sample completeness curves from our mock JAGUAR catalogues (C. C. Williams et al. 2018) coloured by EPOCHS v2 survey. Solid coloured lines show the average completeness of the combined catalogue for a particular survey and the thinner dashed lines show the results for each individual catalogue. The thick, dashed, black horizontal line shows the 90% completeness limit. We note that the brightest and most massive bins have a reduced sample size, and more JAGUAR realizations are required to average over this variance. **Upper panel)** Completeness defined in terms of M_{UV} . **Lower panel)** Completeness curves defined in terms of input BEAGLE stellar mass, M_* .

limit is plotted as the horizontal dashed grey line; this comparison plot shows that when *Bagpipes* can match the observed $H\alpha$ fluxes with a dust-free stellar population it does so, and in the case of $\xi_{ion,obs} > \xi_{ion,intr}$, *Bagpipes* instead assigns increasing amounts of dust until the F444W $H\alpha$ flux is reached. This will bestow large A_V (as much as ~ 0.6 mag) values to the youngest, most highly star forming systems, which are likely dust-

free due to the timescales required for asymptotic giant branch (AGB) stars to produce copious amounts of dust.

As explored in Appendix B, there also exists a limiting sensitivity to which we can detect a flux boost in F444W compared to the continuum as measured in F410M. Below this sensitivity limit ($\log_{10}(\xi_{ion,0}/\text{Hz erg}^{-1}) = 25.0$ at 1σ), the SED fitting becomes biased towards lower photometric $\xi_{ion,0}$. A bootstrapped Kolmogorov-Smirnov (KS) goodness-of-fit test is performed over 100,000 steps, from which we measure $KS = 0.25^{+0.06}_{-0.07}$ and $p = 0.02^{+0.17}_{-0.02}$. This low p -value suggests that systematics do indeed exist in the SED fitting process, in part due to the prior limit imposed by limitations of modeling the youngest stars and the $\xi_{ion,0}$ sensitivity limit.

3.3. Ionizing photon production efficiency as a function of M_{UV}

The M_{UV} dependence of our $\xi_{ion,0}$ estimates for our 90% stellar mass complete sample is presented in Figure 5. In the upper panel we split by survey origin; the bright end is dominated by our widest PRIMER-UDS and PRIMER-COSMOS surveys and the faint end is dominated by the deepest JADES-DR3-GS data. White stars correspond to measurements from the DJA v4.2 spectroscopic sample of 71 sources outlined in subsection 3.2. These spectroscopic $\xi_{ion,0}$ values are dust-corrected with A_{UV} determined via conversion from β_{UV} (measured directly from the PRISM spectra in the 10 D. Calzetti et al. (1994) filters) assuming the G. R. Meurer et al. (1999) conversion factor, and hence show characteristically larger values than in the right-hand panel of Figure 4. The clear trend of *Bagpipes* burstiness with measured $\xi_{ion,0}$ is clear to see in the lower panel of Figure 5, where we plot results from both the star forming and smouldering subsamples.

We utilize Monte Carlo Markov Chain (MCMC) sampling techniques to fit a power law using the *emcee* python package (D. Foreman-Mackey et al. 2013). Wide uniform priors on the amplitude and slope are adopted with limits $\pm 10\sigma$ from the median value of a preliminary linear least squares fit. Our results suggest that the flat relation

$$\log_{10}(\xi_{ion,0}/\text{Hz erg}^{-1}) = -0.006^{+0.019}_{-0.017} M_{UV} + 25.05^{+0.39}_{-0.34} \quad (4)$$

is most appropriate, consistent with *HST* canonical values at $M_{UV} \simeq -19$ (B. E. Robertson et al. 2013). Best-fit parameters and errors for our SFG and smouldering subsamples are shown in Table 3 in Appendix A.

Bootstrap-binned data points are additionally shown for the combined, SFG, and smouldering subsamples using the following methodology. First we sample from the

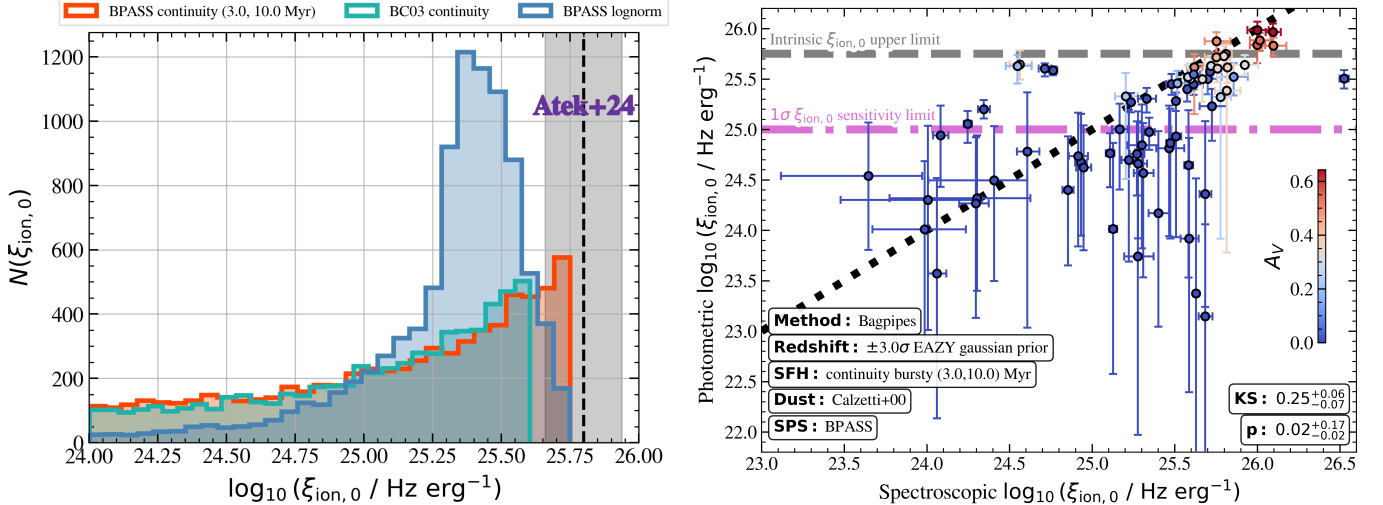


Figure 4. **Left panel)** Bagpipes $\xi_{\text{ion},0}$ priors for our fiducial setup (orange red), with BC03 and the standard *S. Tacchella et al. (2022)* “continuity bursty” SFH (sea green) and BPASS lognormal SFH (blue) also shown. Mean $\xi_{\text{ion},0}$ results from UNCOVER by *H. Atek et al. (2024)* are shown for comparison. **Right panel)** Comparison of spectroscopic *observed* $\xi_{\text{ion},0}$ measured from narrow H α fits to 71 $5.6 < z < 6.5$ NIRSpc PRISM/CLEAR spectra from the DJA against mock photometric measurements computed using our fiducial Bagpipes setup. The intrinsic (i.e. dust free) $\xi_{\text{ion},0}$ upper prior limit from the left-hand panel is shown as a dashed grey line and the 1σ $\xi_{\text{ion},0}$ sensitivity limit at $\log_{10}(\xi_{\text{ion},0}/\text{Hz erg}^{-1}) = 25.0$ is shown in purple. We colour the $\xi_{\text{ion},0}$ measurements by the photometrically determined V-band dust attenuation, A_V . The result of a bootstrapped KS goodness-of-fit test and corresponding p -value is shown in the lower right.

M_{UV} and $\xi_{\text{ion},0}$ PDFs before splitting into evenly spaced 1 dex M_{UV} bins. The $\xi_{\text{ion},0}$ values in each bin are then resampled using the wild bootstrapping scheme

$$\xi'_{\text{ion},0,i} = f(M_{\text{UV},i}; \hat{\theta}) + \hat{\epsilon}_i \mathfrak{R}, \quad (5)$$

for each value, i , where f is the power law model evaluated with best-fit parameters $\hat{\theta}$, and $\hat{\epsilon}_i = \xi_{\text{ion},0,i} - f(M_{\text{UV},i}; \hat{\theta})$ is the $\xi_{\text{ion},0}$ residual to the best-fit model. Since $\sigma_{\xi_{\text{ion},0}}$ scale with $\xi_{\text{ion},0}$, we multiply the residuals by a Rademacher distribution (\mathfrak{R} , with probability density $p(k) = \frac{1}{2}(\delta(k-1) + \delta(k+1))$) to account for the heteroscedasticity.

3.4. Scatter in the $\xi_{\text{ion},0} - M_{\text{UV}}$ relation

From [Figure 5](#), it is clear that our measurement errors on $\xi_{\text{ion},0}$ are non-Gaussian and therefore that our data is heteroscedastic. We thus model the asymmetric scatter in the distribution as $\sigma(\xi_{\text{ion},0}) = |\sigma_c + \sigma_{\xi_{\text{ion},0}} \xi_{\text{ion},0}|$, where the variance on $\xi_{\text{ion},0}$ in the log-likelihood function is calculated as the quadrature sum of this scatter with the Bagpipes measurement uncertainties for each source. Wide uniform priors of $\sigma_c \in [10^{-6}, 100]$ and $\sigma_{\xi_{\text{ion},0}} \in [-100, 0]$ are adopted so as to break the bimodality between negative and positive scatter solutions.

The posterior scatter parameters are $\sigma_c = 18.98^{+1.13}_{-1.07}$ and $\sigma_{\xi_{\text{ion},0}} = -0.754^{+0.043}_{-0.045}$, indicating that the scatter reduces with increasing $\xi_{\text{ion},0}$. These results high-

light the uniformity of $\xi_{\text{ion},0}$ measurements for star-forming galaxies which are currently in a burst phase; smouldering galaxies, which are *on average* older, may have greater diversity in galaxy properties, such as stellar masses or sSFRs. The scatter parameters $\Theta = \{\sigma_c, \sigma_{\xi_{\text{ion},0}}\}$ for our star forming and smouldering subsamples are shown in [Table 3](#).

3.5. Literature comparison of $\xi_{\text{ion},0} - M_{\text{UV}}$

We compare our $\xi_{\text{ion},0} - M_{\text{UV}}$ results to the recent literature in [Figure 6](#). Our results are in contrast with the most recent photometric results, which suggest that $\xi_{\text{ion},0}$ increases towards brighter UV magnitudes.

3.5.1. Photometric studies

Early JWST-derived results from [C. Simmonds et al. \(2024a\)](#) suggest a strong positive trend in the opposite direction at $z \simeq 6$, mitigated by [C. Simmonds et al. \(2024b\)](#) who perform a 90% completeness cut in stellar mass to remove faint low-mass SFGs, which are inherently more detectable than their less bursty counterparts at the same M_* , “star bursting into the sample”. Since [C. Simmonds et al. \(2024b\)](#) report a 90% mass completeness limit at $M_* \simeq 10^{7.5} M_\odot$, which is 0.5–1.5 dex lower than ours in GOODS-North/South (see [Figure 3](#) in [subsection 2.6](#)), we might expect our stellar mass cut to provide a significantly steeper slope, however this is not what is observed. Perhaps the difference stems more from the Prospector SED fitting procedure, which is-

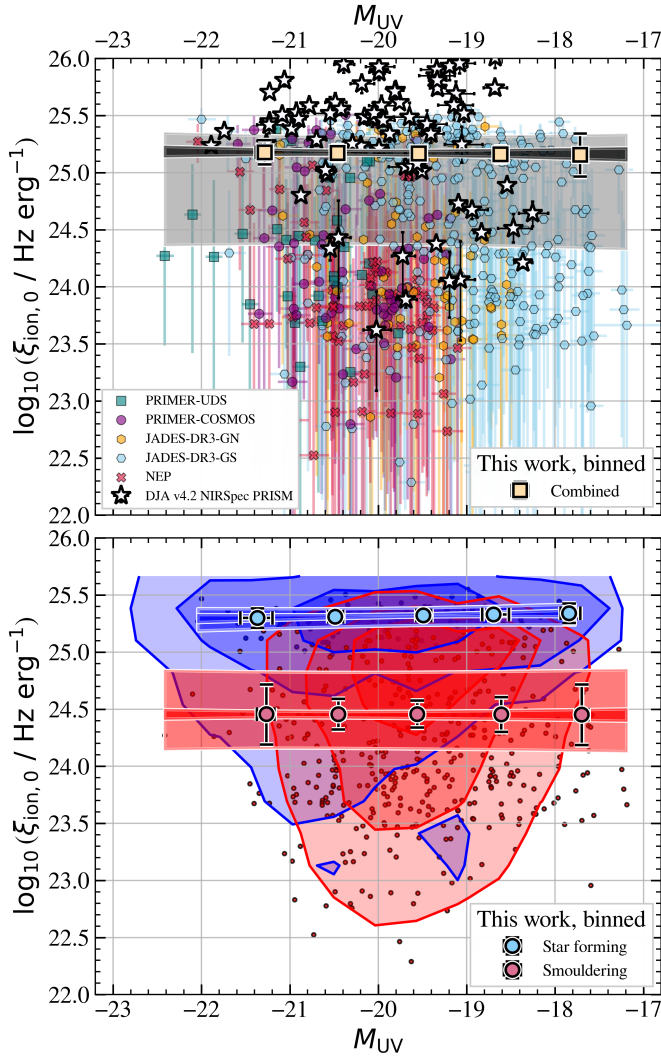


Figure 5. $\xi_{\text{ion},0} - M_{\text{UV}}$ derived from our 90% stellar mass complete sample. Darker shaded regions show the 16th–84th percentiles of the linear fit, with lighter shaded regions showing the scatter in the data. Fitting parameters are given in Table 3. Wild bootstrap-binned data points calculated using Equation 5 are displayed in 1 dex M_{UV} bins. **Upper panel)** Results are coloured by photometric origin field, with white stars showing measurements from our 71 selected NIRSpec/PRISM spectra. **Lower panel)** Results obtained for star forming (blue) and smouldering (red) subsamples. The respective contours show $\{1, 2, 3\}\sigma$ confidence intervals.

used by C. Simmonds et al. (2024a) and C. Simmonds et al. (2024b), compared to *Bagpipes*.

The R. Begley et al. (2025a) $6.9 < z < 7.6$ sample derived from $[\text{O III}]+\text{H}\beta$ uses the same *Bagpipes* setup as us, using data from PRIMER and JADES, and report a similar $M_{\star} \simeq 10^{7.6} M_{\odot}$ 90% mass completeness limit and $\xi_{\text{ion},0} - M_{\text{UV}}$ slope to C. Simmonds et al. (2024b). We caution that this result may be influenced by the metallicity dependence of $[\text{O III}]/\text{H}\beta$, which cannot eas-

ily be constrained by photometry alone, leading to an increase in scatter of scaling relations which convert this quantity to $\xi_{\text{ion},0}$ (see e.g. M. Tang et al. 2019). In addition, we note that this *Bagpipes* setup fails to reproduce simultaneously the $[\text{O III}]+\text{H}\beta$ and $\text{H}\alpha + [\text{N II}]$ fluxes. Nevertheless, the study is comprehensive and it remains challenging to determine the reasons for the difference between our fitted relations.

3.5.2. Spectroscopic studies

Spectroscopic studies appear to show wildly differing results, potentially stemming from the unknown and complex Micro-Shutter Assembly (MSA) selection function. In line with our spectroscopic sample at $z \simeq 6$, many studies appear to show an increasing $\xi_{\text{ion},0}$ towards faint M_{UV} , including those from CEERS, JADES, GLASS, and UNCOVER (M. Llerena et al. 2025; C. Papovich et al. 2025), as well as the Early eXtragalactic Continuum and Emission Line Science (EXCELS; GO 3543; PIs: A. Carnall, F. Cullen; A. C. Carnall et al. 2024, see R. Begley et al. 2025b for the $\xi_{\text{ion},0}$ analysis) program. Presumably these samples include preferentially bursty, faint galaxies, which have been the source of much intrigue. The work of A. J. Pahl et al. (2025a) using CEERS and JADES NIRSpec spectra, and subsequently the Assembly of Ultradeep Observations Revealing Astrophysics (AURORA; PID:1914) sample in A. J. Pahl et al. (2025b), shows an opposing trend. Our photometric observations show a significantly flatter trend than any of these studies would suggest.

3.5.3. Hydrodynamical simulations and SAMs

We additionally compare our results to those from hydrodynamical simulations on large scales from the First Light And Reionization Epoch Simulations (FLARES; C. C. Lovell et al. 2021; A. P. Vijayan et al. 2021; S. M. Wilkins et al. 2023; L. T. C. Seevave et al. 2023), and SPHINX (J. Rosdahl et al. 2018, 2022; H. Katz et al. 2023b) simulations. Results from the Dark matter and the Emergence of gaLaxies in the ePoch of reIonization (DELPHI; P. Dayal et al. 2020; V. Mauerhofer et al. 2025) SAM are also shown in Figure 6 for the fiducial (green) and extended IMF (eIMF; light blue) runs.

Our combined sample is consistent with the fiducial DELPHI run with standard IMF, although our SFG sample is $\sim 0.1 - 0.15$ dex higher, matching the extended IMF model at $M_{\text{UV}} \gtrsim -20$. This sample best matches the FLARES data at $M_{\text{UV}} \lesssim -20$ and overpredicts SPHINX until $M_{\text{UV}} \simeq -18$. The increase in $\xi_{\text{ion},0}$ towards faint M_{UV} values in the SPHINX and eIMF DELPHI run is indicative of exotic starburst populations beginning to dominate the sample. This is observed in spectroscopic samples as well as our stellar

mass complete photometric sample, although with not quite as extreme an inflection point.

3.6. $\xi_{\text{ion},0} - M_{\text{UV}}$ relation as a function of stellar mass

We fit our $\xi_{\text{ion},0} - M_{\text{UV}}$ in fiducial `Bagpipes` stellar mass bins ranging $M_{\star} = 10^{8.5-10.5} M_{\odot}$ in equal width 0.5 dex bins to investigate the origin of the scatter. Since the best-fit parameters and scatter in our star forming subsamples split by mass remains approximately consistent with the total, we focus our discussion on the scatter within our smouldering subsample, with results shown in Figure 7.

Two differences can be observed for our smouldering sample. Firstly, at a given M_{UV} galaxies have reduced $\xi_{\text{ion},0}$ at higher M_{\star} , indicative of increasingly self-regulated systems with less stochastic and more secular star formation. Secondly, the $\sigma_{\xi_{\text{ion},0}}$ scatter additionally reduces with increased M_{\star} , seen in the lower left inset of Figure 7. This may favour a scenario where high mass ($M_{\star} \simeq 10^{9.5-10} M_{\odot}$) mini-quenched systems facilitate LyC escape only from density-bounded nebulae as a result of their reduced ISM porosities. Since more massive systems are on average older and in more overdense environments, they are likely to be gas poor, making this scenario more plausible than the alternative “ionization bounded with holes” which may be more common in lower mass bursty systems (see e.g. E. Zackrisson et al. 2013; K. Duncan & C. J. Conselice 2015, for a further discussion).

4. REIONIZATION BUDGET CONSTRAINTS

4.1. Formulating the contribution of galaxies to reionization

In this work, we determine the total contribution of galaxies to reionization in terms of M_{UV} , which is less prone to the systematics stemming from the assumptions made when performing SED fitting than the stellar mass. While F444W NIRCcam grism spectroscopy has been used to calculate the $\text{H}\alpha$ luminosity function at $z \simeq 6$ (A. Covelo-Paz et al. 2025; X. Lin et al. 2025) in the First Reionization Epoch Spectroscopically Complete Observations (FRESCO; P. A. Oesch et al. 2023) survey, the selection of these sources remains line flux limited. Using deeper JWST/NIRCcam allows us to produce independent measurements in a UV selected sample, which may in theory host a significant number of smouldering galaxies missed by slitless spectroscopy.

Defining \dot{n}_{ion} as the rate of ionizing photon production into the IGM per unit co-moving volume, the total contribution from galaxies in terms of M_{UV} is thus written

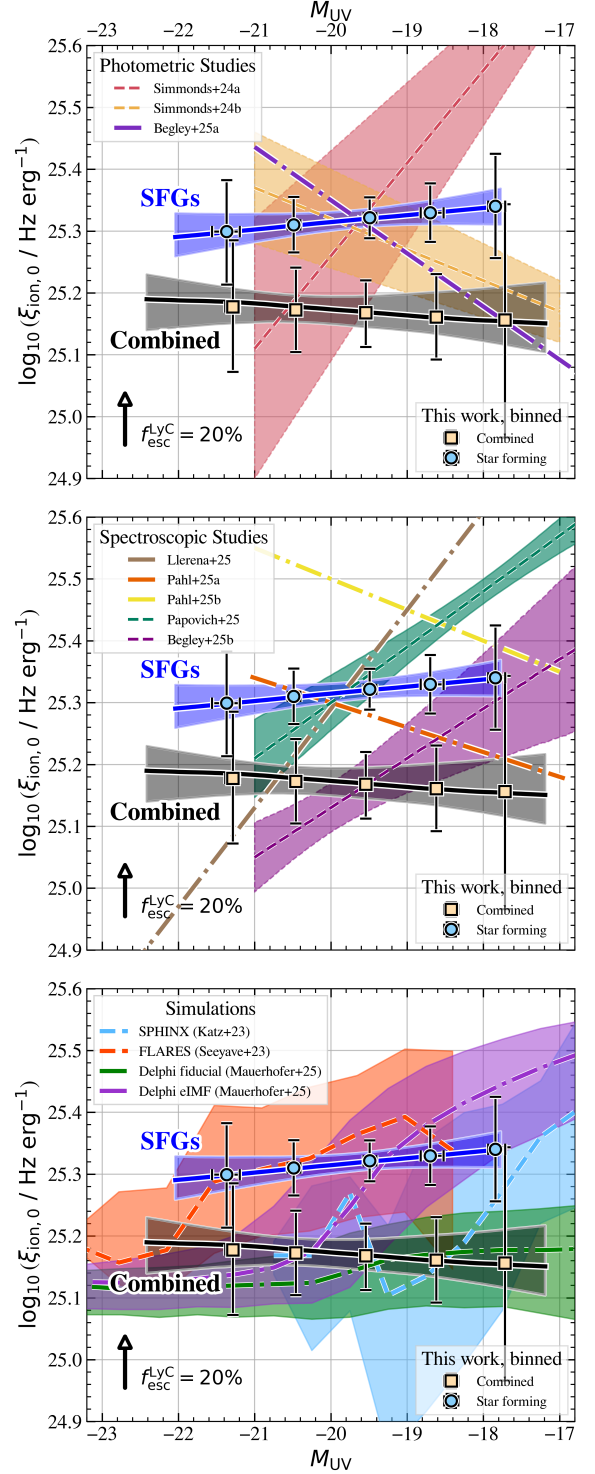


Figure 6. $\xi_{\text{ion},0} - M_{\text{UV}}$ power law fits to our SFG and combined samples, with wild bootstrap bins computed as per Equation 5. The shaded regions show the 16th – 84th percentiles. **Upper panel)** Comparison to photometric studies (C. Simmonds et al. 2024a,b; R. Begley et al. 2025a). **Central panel)** Comparison with spectroscopic studies (M. Llerena et al. 2025; A. J. Pahl et al. 2025a,b; C. Papovich et al. 2025; R. Begley et al. 2025b). **Lower panel)** Comparison to SPHINX (H. Katz et al. 2023b, light blue), FLARES (L. T. C. Seeyave et al. 2023, orange), and DELPHI (V. Mauerhofer et al. 2025, fiducial in dark green, extended IMF in purple) simulations.

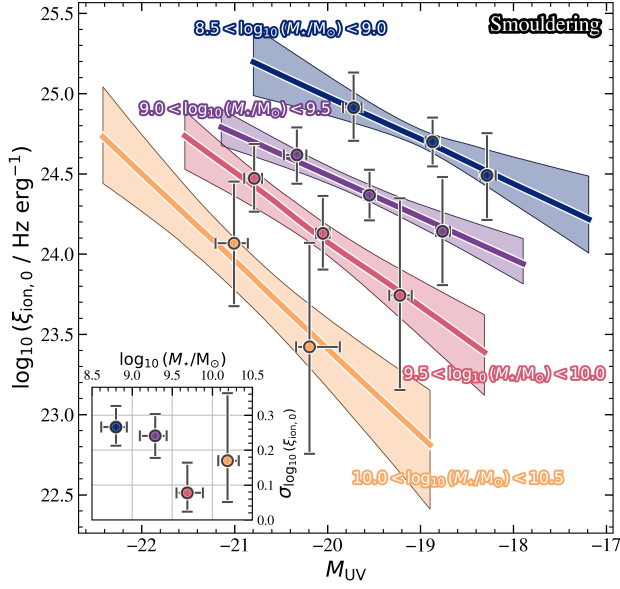


Figure 7. $\xi_{\text{ion},0}-M_{\text{UV}}$ relation for our smouldering subsample in 0.5 dex stellar mass bins across the range $8.5 < \log_{10}(M_*/M_{\odot}) < 10.5$. The symmetric scatter, $\sigma_{\log_{10}(\xi_{\text{ion},0})}$, is given as a function of M_* in the lower left inset panel. Wild bootstrapped binned data points are computed as per Equation 5.

as

$$\dot{n}_{\text{ion}} = \int_{-\infty}^{M_{\text{UV},\text{lim}}} \Phi(M_{\text{UV}}) f_{\text{esc}}(M_{\text{UV}}) \dot{N}_{\text{ion}}(M_{\text{UV}}) dM_{\text{UV}}, \quad (6)$$

where $\Phi(M_{\text{UV}})$ is the UVLF and $M_{\text{UV},\text{lim}}$ is the UV magnitude corresponding to the turnover of the UVLF. In the remainder of this section, we produce M_{UV} dependent scaling relations and UVLFs for our entire combined sample as well as for our star forming and smouldering subsamples, summing their contributions to determine a total.

4.2. $\beta_{\text{UV}} - M_{\text{UV}}$ and a new empirical $f_{\text{esc}}^{\text{LyC}}$ prescription

The dependence of β_{UV} on M_{UV} for our 90% stellar mass complete sample is measured in Figure 8. We utilize Monte Carlo Markov Chain (MCMC) sampling techniques to fit a power law using the `emcee` python package (D. Foreman-Mackey et al. 2013). Wide uniform priors on the amplitude and slope are adopted with limits $\pm 10\sigma$ from the median value of a preliminary linear least squares fit. We model the scatter in amplitude, $\sigma_{\beta,\text{scat}}$, as a constant which is additionally left free in the fitting procedure with a wide, positive, uniform prior. A mild trend of

$$\beta_{\text{UV}} = (-0.040 \pm 0.022)M_{\text{UV}} - 2.88 \pm 0.34 \quad (7)$$

is observed such that fainter galaxies are bluer with $\sigma_{\beta,\text{scat}} = 0.27 \pm 0.02$ scatter. No significant differences in the best fit parameters and scatter are found between the star forming and smouldering subsamples.

Compared with previous HST studies utilizing ACS WFC and WFC3-IR data over the XDF, HUDF, CANDELS, and HFF lensing fields (e.g. S. L. Finkelstein et al. 2012; R. J. Bouwens et al. 2014; R. Bhatawdekar & C. J. Conselice 2021), we find a somewhat shallower slope. This may be due to the fact that we use the ultra-blue “fspi_larson” template set used in the Eazy-py SED fitting procedure, however our analogous sample of spectroscopically confirmed $z \simeq 6$ sources from the DJA suggest that some of these bright ultra-blue sources may be the so-called “blue monsters” from F. Ziparo et al. (2023). Perhaps this unusual population of galaxies have large specific SFRs (sSFR) with strong radiation driven outflows which remove copious amounts of dust from the ISM (A. Ferrara 2024) or are strong leakers of LyC photons, perhaps in a different mode than leaking faint galaxies (H. Katz et al. 2023a).

To first order, the escape fraction of LyC from the ISM of galaxies can be determined from measurements of β_{UV} , albeit with a $\gtrsim 1$ dex scatter (J. Chisholm et al. 2022). Converting the relation in Equation 7 to $f_{\text{esc}}^{\text{LyC}}$ following this prescription, derived from the Low-redshift Lyman Continuum Survey (LzLCS), we find a fairly moderate $\langle f_{\text{esc}}^{\text{LyC}} \rangle \simeq 5\%$ at $M_{\text{UV}} \simeq -19.0$. Fainter galaxies are found to have on average slightly larger $f_{\text{esc}}^{\text{LyC}}$ and vice versa, however since our $\beta_{\text{UV}} - M_{\text{UV}}$ is shallower than previous studies have found, the difference is somewhat reduced. We do not use multivariate models to estimate $f_{\text{esc}}^{\text{LyC}}$ in this work (N. Choustikov et al. 2024a,b; A. E. Jaskot et al. 2024a,b), although this remains a promising future avenue for photometric and spectroscopic studies.

4.3. The relationship of $\dot{N}_{\text{ion},0}$ with M_{UV}

For each source, we compute $\dot{N}_{\text{ion},0}$ directly within the `Bagpipes` “model_galaxy” to produce full Bayesian posteriors following Equation 1 and Equation 3. These $\dot{N}_{\text{ion},0}$ values are subsequently inflated for extended sources following the same methodology as the stellar masses outlined in subsection 2.3.2. As before, we plot the resulting $\dot{N}_{\text{ion},0}-M_{\text{UV}}$ relation in Figure 9, plotting the combined photometric (split by origin survey) and spectroscopic sample in the upper panel and splitting into SFG and smouldering subsamples in the lower panel.

The literature comparison is similar to that shown in Figure 6, although we note that the C. Simmonds et al. (2024b) $\dot{N}_{\text{ion},0}-M_{\text{UV}}$ relation is slightly flatter than our

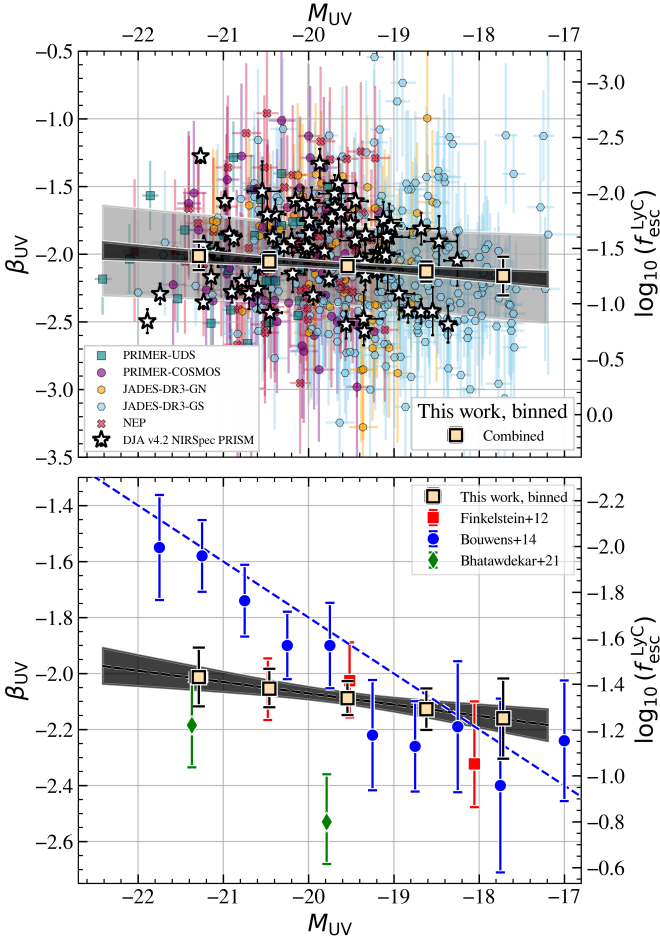


Figure 8. Upper panel) $\beta_{UV} - M_{UV}$ relation for our 90% stellar mass complete sample at $5.6 < z < 6.5$ coloured by EPOCHS-v2 origin survey. Spectroscopic sources from the DJA are shown as white stars. The dark shaded region shows the 16th – 84th percentile of the power law fit, with the light shaded region showing the symmetric $\sigma_{\beta, \text{scat}} = 0.27 \pm 0.02$ scatter. **Lower panel)** Our best-fit model, and wild bootstrap-binned data points (beige squares), compared to *HST* studies from S. L. Finkelstein et al. (2012), R. J. Bouwens et al. (2014), and R. Bhatawdekar & C. J. Conselice (2021) at $z \simeq 6$. The secondary y-axis shows $\log_{10}(f_{\text{esc}}^{\text{LyC}})$ calculated using the LzLCS scaling relation from β_{UV} presented in J. Chisholm et al. (2022).

SFG sample, most likely due to their dust assumptions made when SED fitting with *Prospector*. Our data has a larger dynamic range in UV magnitude, especially at the bright end, due to our inclusion of data from PRIMER-UDS, PRIMER-COSMOS, and NEP fields, as opposed to the JADES (GOODS-South + GOODS-North) data used in C. Simmonds et al. (2024b).

Although clearly visible in the $\xi_{\text{ion},0} - M_{UV}$ relation in Figure 5, the upper envelope of the prior in $\xi_{\text{ion},0}$ is not as apparent in $\dot{N}_{\text{ion},0} - M_{UV}$ space. The likely

culprit is the dust attenuation; the UV luminosity on the denominator of Equation 2 is dust-corrected, which means the upper $\dot{N}_{\text{ion},0} - M_{UV}$ prior envelope no longer follows a power-law since M_{UV} is an observed (non dust-corrected) quantity.

We fit power-law relations to the data in Figure 9 in a similar way to the $\xi_{\text{ion},0} - M_{UV}$ data, additionally including an M_{UV} dependence in the scatter to account for the heteroscedasticity which now exists in this variable (i.e. sources that are faint in $L_{\nu, UV}$ are likely also faint in $L_{H\alpha}$). Results of this fitting procedure are presented in Table 3 in Appendix A. Wild bootstrap-binned data are computed following Equation 5 replacing $\xi_{\text{ion},0,i}$ with $\dot{N}_{\text{ion},0,i}$.

4.4. UV luminosity function

4.4.1. Calculating the UVLF using the $1/V_{\text{max}}$ method

Taking our final sample of 1721 galaxies, we construct the UVLF using the $1/V_{\text{max}}$ method (M. Schmidt 1968; M. Rowan-Robinson 1968) at $z \simeq 6$ for the first time with a JWST/NIRCam selected sample. For each galaxy, we calculate the maximum (z_{max}) and minimum (z_{min}) detectable redshift in each field using the average depth measurements combined with the selection criteria listed in subsection 2.2 in steps of $\delta z = 0.01$. From these z_{min} and z_{max} values, we calculate the comoving $V_{\text{max},i,j}$ for each galaxy, i , in each field, j , in our assumed cosmology using the unmasked areas given in section 2. The maximum detectable volume for each galaxy ($V_{\text{max},i}$) can be determined by simply summing the $V_{\text{max},i,j}$ for each field.

The sample is split into magnitude bins of size $\Delta M_{UV} = 0.5$ and the number density in each bin is calculated as

$$\Phi(M_{UV})d\log_{10}(M_{UV}) = \frac{1}{\Delta M_{UV}} \sum_i \frac{1}{C_i V_{\text{max},i}}, \quad (8)$$

where C_i is the completeness of galaxy i calculated as a function of F115W SNR (corresponding to the rest-frame UV at $z \simeq 6$) following the procedure explained in subsection 2.6. The Poisson uncertainty in each bin is calculated as

$$\delta\Phi(M_{UV}) = \frac{1}{\Delta M_{UV}} \sqrt{\sum_i^N \left(\frac{1}{C_i V_{\text{max},i}} \right)^2}. \quad (9)$$

For magnitude bins with low occupancy ($N \leq 4$) the above formula overestimates the error. In these instances, we adopt the Poisson confidence interval from K. Ulm (1990) based on the χ^2 distribution $I = [0.5\chi_{2N,a/2}^2, 0.5\chi_{2(N+1),1-a/2}^2]$ similarly to N. J. Adams et al. (2024), N. J. Adams et al. (2025), and T. Harvey

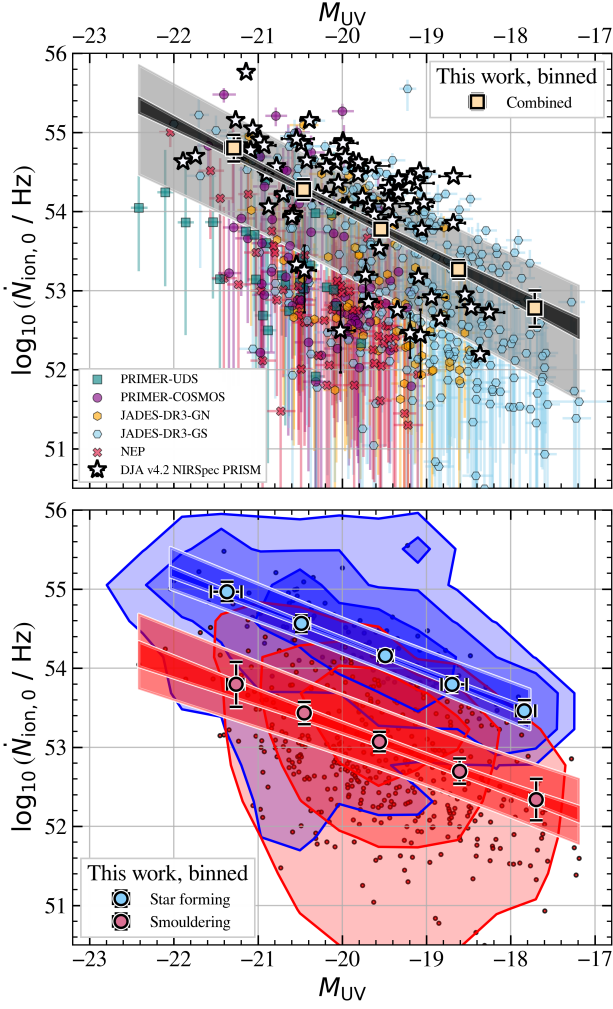


Figure 9. $\dot{N}_{\text{ion}} - M_{\text{UV}}$ relation for our 90% stellar mass complete $5.6 < z < 6.5$ sample in the large area EPOCHS-v2 surveys. The dark shaded regions show the 16th–84th percentile of the power law fit to each subsample, with the light shaded regions showing the asymmetric scatter fitted as a function of both \dot{N}_{ion} and M_{UV} . **Upper panel)** Data is coloured by EPOCHS-v2 origin survey. Spectroscopic sources from the DJA are shown as white stars and wild bootstrap-binned data points are shown as beige squares. **Lower panel)** Results for our star forming (blue) and smouldering (red) subsamples. Contours are shown for $\{1, 2, 3\}\sigma$ significance levels. Wild-bootstrap-binned data is shown as light blue/light red circles.

et al. (2025). The UVLF for our sample, as well as our star forming and smouldering subsamples, is shown in Figure 10 which includes completeness corrections and cosmic variance as explained below.

4.4.2. Estimating completeness

The completeness of the various fields used in this sample is shown in subsection 2.6, where for the UVLF, we use the completeness curves in terms of M_{UV} rather

Table 1. Completeness corrected UV luminosity function bins for the combined, star forming, smouldering samples, as plotted in Figure 10. Amplitudes are measured as per Equation 8 and errors comprise of both Poisson and cosmic variance derived via the prescription given in S. P. Driver & A. S. G. Robotham (2010) assuming square survey geometries in each case.

M_{UV} bin (AB mag)	$\Phi(M_{\text{UV}})$ ($\times 10^{-4} \text{ mag}^{-1} \text{ cMpc}^{-3}$)	N_{gals}
Combined sample		
$[-22.25, -21.75]$	0.08 ± 0.04	5
$[-21.75, -21.25]$	0.32 ± 0.07	19
$[-21.25, -20.75]$	1.06 ± 0.14	60
$[-20.75, -20.25]$	2.63 ± 0.22	149
$[-20.25, -19.75]$	5.03 ± 0.34	263
$[-19.75, -19.25]$	8.19 ± 0.50	318
$[-19.25, -18.75]$	14.84 ± 0.91	312
$[-18.75, -18.25]$	25.21 ± 1.72	280
$[-18.25, -17.75]$	48.07 ± 3.41	213
Star forming		
$[-22.25, -21.75]$	$0.05^{+0.05}_{-0.03}$	3
$[-21.75, -21.25]$	0.15 ± 0.05	9
$[-21.25, -20.75]$	0.45 ± 0.09	27
$[-20.75, -20.25]$	1.45 ± 0.16	83
$[-20.25, -19.75]$	2.83 ± 0.23	156
$[-19.75, -19.25]$	4.69 ± 0.37	187
$[-19.25, -18.75]$	9.85 ± 0.75	207
$[-18.75, -18.25]$	16.58 ± 1.37	188
$[-18.25, -17.75]$	34.41 ± 2.87	153
Smouldering		
$[-22.25, -21.75]$	$0.03^{+0.05}_{-0.02}$	2
$[-21.75, -21.25]$	0.17 ± 0.05	10
$[-21.25, -20.75]$	0.60 ± 0.11	33
$[-20.75, -20.25]$	1.18 ± 0.15	66
$[-20.25, -19.75]$	2.18 ± 0.24	107
$[-19.75, -19.25]$	3.47 ± 0.34	131
$[-19.25, -18.75]$	4.89 ± 0.52	105
$[-18.75, -18.25]$	8.58 ± 1.04	92
$[-18.25, -17.75]$	13.66 ± 1.84	60

than stellar mass. Since our surveys are rarely completely uniform in depth, we define our completeness in bins of F115W SNR corresponding to the rest-frame UV at $z \simeq 6$; correction factors, $C_{i,j}$, are calculated for each galaxy in each survey. We find that our faintest M_{UV} bin is $\lesssim 30 - 50\%$ complete, which we decide not to use in the Schechter fitting procedure explained below.

The detection completeness of smouldering galaxies is expected to better scale with peak $\Sigma_{\text{SFR}_{10\text{Myr}}}$ (R. Endsley et al. 2024), meaning it is quite likely that these galaxies suffer more from detection incompleteness than

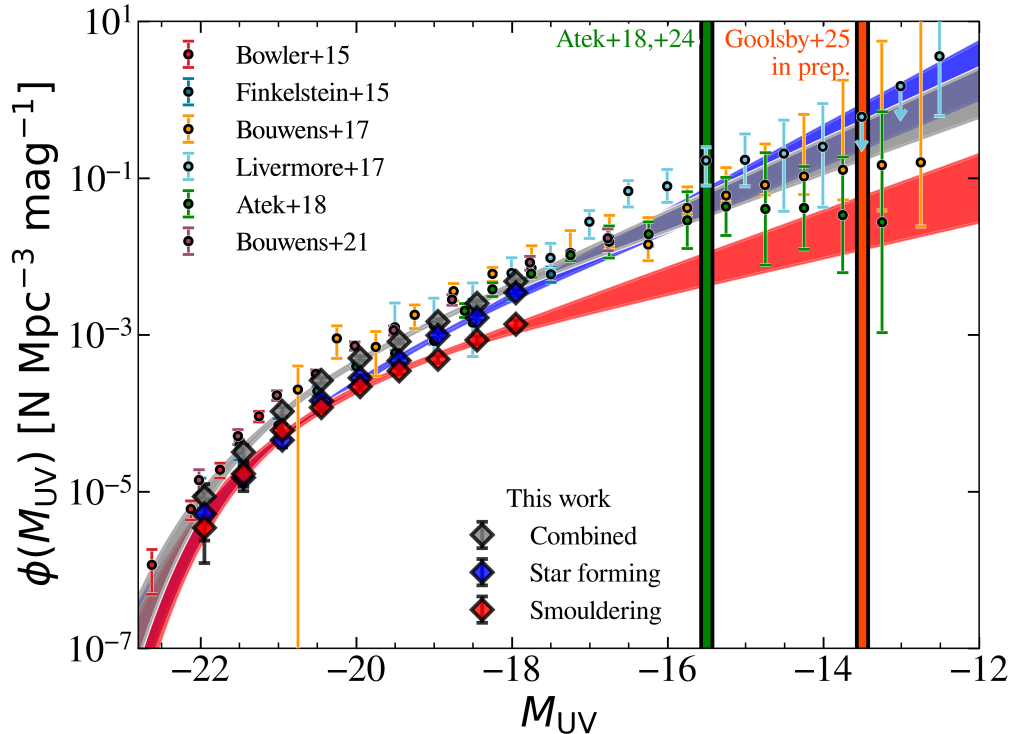


Figure 10. $z \simeq 6$ UVLF for the combined, star forming, and smouldering subsamples plotted as diamonds. P. Schechter (1976) model posterior solutions are plotted for each subsample, with the shaded region highlighting the 1σ errors. Results are compared to measurements of the bright end (R. A. Bowler et al. 2015, from the ground-based UltraVISTA survey), the knee (S. L. Finkelstein et al. 2015; R. J. Bouwens et al. 2021, from *HST* blank fields), and the faint end (R. J. Bouwens et al. 2017; R. C. Livermore et al. 2017; H. Atek et al. 2018, from the HFF strong lensing clusters). Approximate turnover magnitudes from *JWST*-derived measurements by H. Atek et al. (2024) and Goolsby et al. (in prep.) are shown as thick vertical green and orange lines respectively.

our star forming subsample. A thorough analysis using high resolution simulations such as FIRE-2 (P. F. Hopkins et al. 2018) or SPHINX (H. Katz et al. 2023b) is required in order to determine and correct for the full extent of this incompleteness to better constrain the faint end slope of the smouldering galaxy UVLF.

4.4.3. Cosmic variance

In addition to the Poisson errors, we additionally include errors from cosmic variance using the prescription in S. P. Driver & A. S. G. Robotham (2010) and combine the cosmic variance measurements made in each survey using the weighted sum of squares from B. P. Moster et al. (2011). We find that our total cosmic variance measurement at $z \simeq 6$ is 11%. It is worth noting that this value is approximate at this redshift and relies on measurements of galaxy biases from clustering across wide area surveys, which are expected to be strongly dependent on stellar mass and UV luminosity (e.g. I. Zehavi et al. 2011; Y. Harikane et al. 2021). Upcoming galaxy clustering measurements from Euclid should greatly improve the accuracy and precision of these estimates.

4.4.4. Fitting results

We fit our measured $z \simeq 6$ UVLFs with a P. Schechter (1976) luminosity function utilizing a Bayesian MCMC fitting procedure using the `emcee` python package (D. Foreman-Mackey et al. 2013), displaying the resulting corner plot in the upper panel of Figure 11. For consistency, we first check whether fitting results for the sample as a whole agree with previous Schechter luminosity function estimates. Our results are compared to the ground-based UltraVISTA (H. J. McCracken et al. 2012) study by R. A. Bowler et al. (2015), blank field *HST* imaging results (S. L. Finkelstein et al. 2015; R. J. Bouwens et al. 2021), and the strongly lensed Hubble Frontier Field (HFF; R. J. Bouwens et al. 2017; R. C. Livermore et al. 2017; H. Atek et al. 2018).

We find that the amplitude, Φ^* , is slightly lower than the $\log_{10} \Phi^* = -3.1$ measured in R. J. Bouwens et al. (2021), however it remains consistent with a similar study by S. L. Finkelstein et al. (2015), $\log_{10} \Phi^* = -3.7$ across the same field areas. The measured faint-end slopes of $\alpha = -1.93 \pm 0.08$ (R. J. Bouwens et al. 2021) and $\alpha = -2.02 \pm 0.10$ (S. L. Finkelstein et al. 2015)

at $z \simeq 6$ in the literature are consistent with our fitting results of $\alpha = -2.0 \pm 0.2$. As expected, the amplitudes of our subsample UVLF fits are slightly lower than the combined UVLF since there are fewer galaxies in our star forming and smouldering subsamples compared to the combined sample, with M^* remaining approximately consistent. The largest difference between our subsamples lies in the measured faint-end slope, for which we obtain $\alpha_{\text{SFG}} = -2.2 \pm 0.2$ and $\alpha_{\text{sm}} = -1.7 \pm 0.2$.

Since a double power law (DPL) fit has been shown to better match the smooth evolution at the bright end of the UVLF (R. A. Bowler et al. 2014, 2015; R. A. Bowler et al. 2017, 2020), we additionally fit a DPL to our total, star forming, and smouldering UVLFs. Wide uniform priors on the $\Theta = \{\Phi^*, M^*, \alpha, \beta\}$ free parameters are used in the `emcee` fitting procedure, where β is the bright end slope found to be $\beta = -4.4$ by R. A. Bowler et al. (2014) at $z = 6$. The posterior corner plot is shown in the lower panel of Figure 11, where wide β posteriors for each subsample (as well as the total) and a bimodal solution for β_{SFG} is observed, highlighting the need for larger area surveys to properly sample this regime. Nevertheless, our results remain consistent at the faint end, which appears robust to our model choice.

To quantify which model is more appropriate to use, we calculate both the Akaike Information Criterion (AIC) and Bayesian Information Criterion (BIC) for both P. Schechter (1976) and DPL UVLF fits. For the total sample, we find $\Delta\text{AIC} = \text{AIC}_{\text{DPL}} - \text{AIC}_{\text{Sch}} = 0.82$ and $\Delta\text{BIC} = \text{BIC}_{\text{DPL}} - \text{BIC}_{\text{Sch}} = 1.02$, highlighting a slight, but insignificant, favour towards the P. Schechter (1976) model due to its simplicity. The same conclusion is reached for our star forming ($\Delta\text{AIC} = 1.35$; $\Delta\text{BIC} = 1.55$) and smouldering ($\Delta\text{AIC} = 0.51$; $\Delta\text{BIC} = 0.71$) subsamples.

4.5. Reionization contribution as a function of M_{UV} :

Tying it all together

The total rate of production of ionizing photons escaping into the IGM is calculated following Equation 6, the integrand of which is shown as a function of M_{UV} in Figure 12 both for J. Chisholm et al. (2022) derived $f_{\text{esc}}^{\text{LyC}}(M_{\text{UV}})$ and fixed $f_{\text{esc}}^{\text{LyC}} = 10\%$. In both cases, the contribution from SFGs is > 1 dex larger than smouldering galaxies, which reduces as with fainter M_{UV} , potentially due to reduced selectability of smouldering galaxies towards the detection limit of our photometric datasets. The SFG contours additionally highlight that faint galaxies that are currently in a starburst phase contribute the majority of the ionizing photons during the EoR.

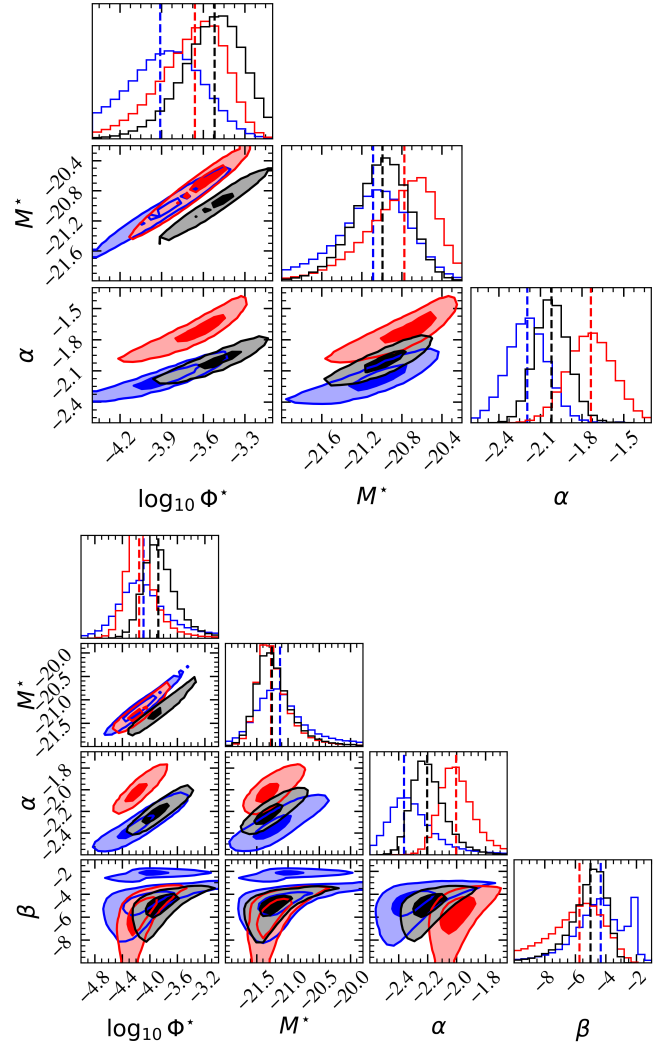


Figure 11. Posterior corner plots for fits to our combined (black), star forming (blue), and smouldering (red) UVLFs at $z \simeq 6$. Dashed vertical lines show the median of each parameter distribution for each subsample. **Upper panel** P. Schechter (1976) model with $\Theta = \{\log_{10} \Phi^*, M^*, \alpha\}$ free parameters. **Lower panel** DPL model with $\Theta = \{\log_{10} \Phi^*, M^*, \alpha, \beta\}$ free parameters

For fixed $f_{\text{esc}}^{\text{LyC}} = 10\%$, our SFG subsample contributes $\sim 0.2 - 0.5$ dex more than the C. Simmonds et al. (2024b) sample, while retaining a similar shape. The amplitude is thus a function of UVLF and $\dot{N}_{\text{ion},0}$ normalizations. Our power law fits to the $\dot{N}_{\text{ion},0} - M_{\text{UV}}$ relation for SFGs displays a higher amplitude than the JADES (GOODS-North + GOODS-South) results from C. Simmonds et al. (2024b). They adopt the R. J. Bouwens et al. (2021) UVLF, which has a larger normalization and shallower faint-end slope than our SFG UVLF shown in Figure 10. This opposes our larger $\dot{N}_{\text{ion},0}$ measurements and leads to our sample producing

an increasing amount faintwards of the UVLF “knee” compared to C. Simmonds et al. (2024b).

In this work, we measure a flatter $\beta_{\text{UV}} - M_{\text{UV}}$ than the work of C. Simmonds et al. (2024b). The impact on \dot{n}_{ion} can be seen when adopting the J. Chisholm et al. (2022) $f_{\text{esc}}^{\text{LyC}}$ parametrization in the lower panel of Figure 12. This increases the prominence of bright galaxies to reionization. Since $f_{\text{esc}}^{\text{LyC}}$ models do not commonly treat SFGs and smouldering galaxies distinctly, our treatment does not highlight the potential differences between LyC escape pathways for different subsamples of galaxies. We note that results assuming alternative $f_{\text{esc}}^{\text{LyC}}$ parametrizations, not shown in this work, may increase the contribution from the brightest “oligarchs” (e.g. R. P. Naidu et al. 2020) and/or change the amplitude of the curves in Figure 12.

4.6. Reionization constraints at $z \simeq 6$

To determine an estimate of the extent to which UV selected galaxies contribute to reionization, we rather arbitrarily define the UVLF turnover to be at $M_{\text{UV,lim}} = -17$. Given this rather crude assumption, we find that our sample as a whole generates $\log_{10} \dot{n}_{\text{ion}} = 50.68 \pm 0.03$ and $\log_{10} \dot{n}_{\text{ion}} = 50.34 \pm 0.04$ for $f_{\text{esc}}^{\text{LyC}} = 0.1$ and J. Chisholm et al. (2022) $f_{\text{esc}}^{\text{LyC}}$ respectively, and that in both cases the smouldering subsample accounts for < 10% of the combined budget.

Results of this integration are shown in Figure 13, where we additionally compare to observational constraints from galaxies (G. D. Becker & J. S. Bolton 2013; R. J. Bouwens et al. 2015b; C. A. Mason et al. 2015, 2019; R. P. Naidu et al. 2020; P. Gaikwad et al. 2023; C. Simmonds et al. 2024b; N. Choustikov et al. 2025; C. Papovich et al. 2025), as well as inferences from the AGN luminosity function (G. Kulkarni et al. 2019), and the late reionization model from the ATON-HE reionization simulation (S. Asthana et al. 2024). Contours showing the required ionizing budget to produce a fully stably ionized Universe with given volume-averaged H II clumping factors, $C_{\text{HII,rec}} = \{1, 3, 10\}$, are calculated following the prescription in P. Madau et al. (1999),

$$\dot{n}_{\text{ion}} = 10^{51.2} \left(\frac{C_{\text{HII,rec}}}{30} \right) \left(\frac{1+z}{6} \right)^3 \left(\frac{\Omega_b h_{50}^2}{0.08} \right)^2 [\text{s}^{-1} \text{Mpc}^{-3}], \quad (10)$$

and are additionally plotted in Figure 13.

Consistent results are found with the observational studies in the literature for fixed $f_{\text{esc}}^{\text{LyC}} = 10\%$, however we measure an $\dot{n}_{\text{ion}} \sim 0.3$ dex lower adopting the J. Chisholm et al. (2022) $f_{\text{esc}}^{\text{LyC}}$ relation from β_{UV} due to our flatter $\beta_{\text{UV}} - M_{\text{UV}}$ relation which produces on average $f_{\text{esc}}^{\text{LyC}} \simeq 5\%$.

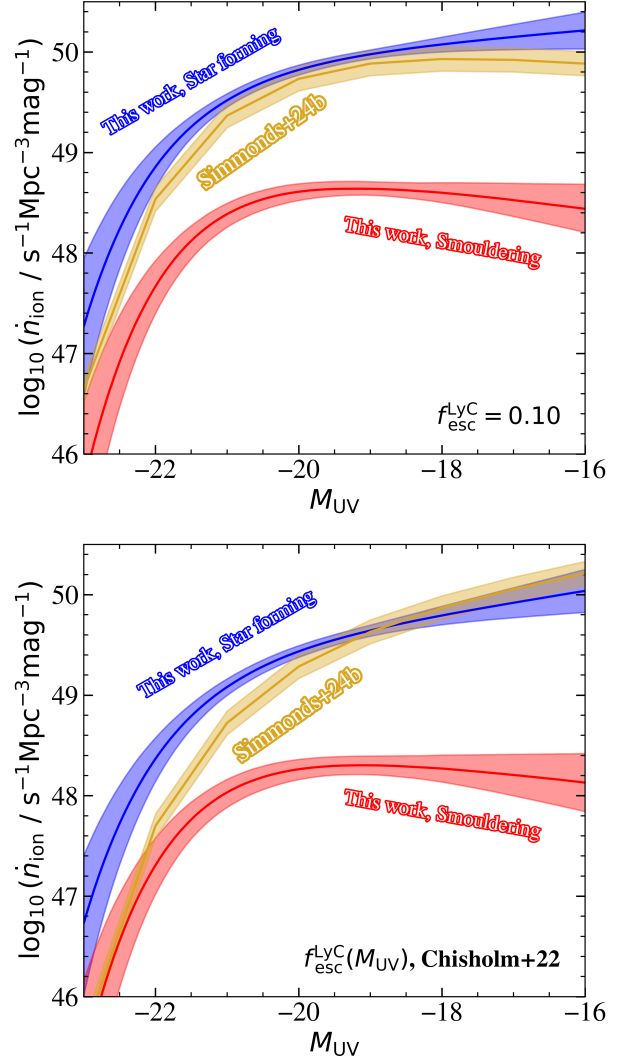


Figure 12. Total contribution to reionization as a function of M_{UV} for our star forming (blue), and smouldering (red) subsamples compared to the C. Simmonds et al. 2024b results (yellow) using the same $f_{\text{esc}}^{\text{LyC}}$ parametrization. The total contribution closely resembles the star forming subsample, which dominates the ionizing photon budget, and is therefore not shown. **Upper panel)** Results use fixed $f_{\text{esc}}^{\text{LyC}} = 10\%$. **Lower panel)** Results use J. Chisholm et al. (2022) derived $f_{\text{esc}}^{\text{LyC}}(M_{\text{UV}})$.

5. IMPLICATIONS FOR IGM H II CLUMPING

5.1. Hydrogen reionization formulation

The reionization of hydrogen has long since been modelled analytically in terms of the ionized fraction, $x_{\text{HII}} \equiv n_{\text{HII}}/n_{\text{H}}$, defined in terms of the number densities of both atomic (HI), and ionized (HII) hydrogen such that $n_{\text{H}} = n_{\text{HI}} + n_{\text{HII}}$. The evolution of this x_{HII} is commonly modelled via the volume-filling factor of HII, Q_{HII} . This is approximately equivalent to x_{HII} pre-overlap of ionized bubbles; $Q_{\text{HII}} > x_{\text{HII}}$ post-overlap due

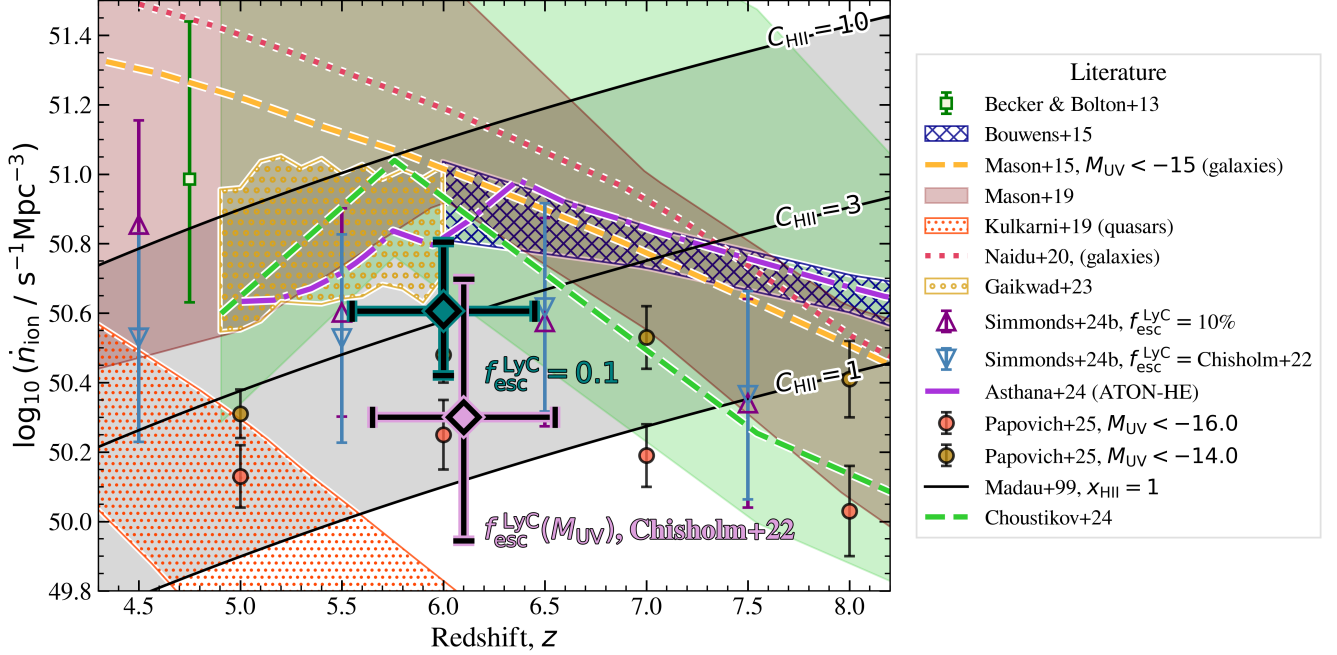


Figure 13. Total rate of ionizing photon production integrated to $M_{\text{UV},\text{lim}} = -17.0$. Results are compared to observations of galaxies (G. D. Becker & J. S. Bolton 2013; R. J. Bouwens et al. 2015a; C. A. Mason et al. 2015, 2019; R. P. Naidu et al. 2020; P. Gaikwad et al. 2023; C. Simmonds et al. 2024b; N. Choustikov et al. 2025; C. Papovich et al. 2025), AGN (G. Kulkarni et al. 2019), and the ATON-HE simulation (S. Asthana et al. 2024). Results adopting our M_{UV} dependent escape fractions derived from the J. Chisholm et al. (2022) scaling relation from β_{UV} are shown as a pink diamond, shifted by $\Delta z = +0.1$ for clarity, and our $f_{\text{esc}}^{\text{LyC}} = 10\%$ result is in teal.

to residual neutral hydrogen remaining within ionized regions. The evolution of Q_{HII} is modelled following the simple ordinary differential equation (ODE) prescription of P. Madau et al. (1999),

$$\frac{dQ_{\text{HII}}}{dt} = \dot{n}_{\text{ion}} - \frac{Q_{\text{HII}}}{\langle t_{\text{rec}} \rangle}, \quad (11)$$

where $\langle t_{\text{rec}} \rangle$ is the volume-averaged recombination timescale (denoted by triangular brackets) given by

$$\langle t_{\text{rec}} \rangle = \left[(1 + x_{\text{He}}) \langle n_{\text{H}} \rangle \langle \alpha_{\text{rec}}(T_e) \rangle C_{\text{HII},\text{rec}} \right]^{-1}, \quad (12)$$

in terms of the electron temperature dependent recombination co-efficient, $\alpha_{\text{rec}}(T_e)$, and recombination-weighted *global* clumping factor, $C_{\text{HII},\text{rec}}$. This equation accounts for the contribution of electrons available for recombination with H II from singly-ionized helium, HeII, with ionization energy 24.6 eV. At $z \simeq 6$ we are in the regime where all helium is singly ionized before the epoch of HeII reionization, which occurs at $z \sim 3 - 4$ (J. S. B. Wyithe & A. Loeb 2002; N. Y. Gnedin & P. Madau 2022), meaning this additional electron density amounts to $x_{\text{He}} \equiv n_{\text{He}}/n_{\text{H}} = Y/[4(1 - Y)] \simeq 0.08$.

For hydrogen reionization equilibrium, where the total rates of ionization and recombination equate (i.e. $dQ_{\text{HII}}/dt = 0$), the fraction of the Universe that can

remain stably ionized is thus given by

$$Q_{\text{HII}} = \frac{\dot{n}_{\text{ion}}(1+z)^3}{\langle n_{\text{H}} \rangle^2 \langle \alpha_{\text{rec}}(T_e) \rangle C_{\text{HII},\text{rec}}} \frac{4(1-Y)}{(4-3Y)}. \quad (13)$$

In this work, we assume case B recombination and an electron temperature $T_e = 10^4$ K typical of H II regions in star-forming galaxies¹⁵, leading to a recombination co-efficient $\alpha_{\text{rec}} \equiv \alpha_{\text{B}} = 2.59 \times 10^{-13} \text{ cm}^3 \text{ s}^{-1}$ (D. E. Osterbrock & G. J. Ferland 2006). In the remainder of this paper, we use Equation 13 to infer the $C_{\text{HII},\text{rec}}$ IGM clumping factor, and discuss this in the context of cosmic reionization.

5.2. Indirect clumping factor constraints

We propagate the $\dot{n}_{\text{ion}}(M_{\text{UV}})$ curves from Figure 12, extrapolated to $M_{\text{UV}} = -12$, through Equation 13 to determine the total fraction of the Universe’s hydrogen that is stably ionized as a function of $C_{\text{HII},\text{rec}}$ and UVLF turnover, $M_{\text{UV},\text{lim}}$, shown in Figure 14. Curves for H II fractions, $x_{\text{HII}} \simeq Q_{\text{HII}} = \{0.7, 1.0\}$ are shown, and although the neutral content of the Universe at $z \simeq 6$ is dependent on whether reionization occurs early (R. H.

¹⁵ At these temperatures the electron density, n_e , makes a minimal impact on α_{B}

Becker et al. 2001; X. Fan et al. 2006; J. Yang et al. 2020, e.g.) or late (e.g. L. C. Keating et al. 2020; S. E. I. Bosman et al. 2022; L. C. Keating et al. 2024; Y. Zhu et al. 2024), Q_{HII} is expected to fall within these bounds. While we obtain similar results to C. Simmonds et al. (2024b) at $M_{\text{UV,lim}} \lesssim -17$, the largest differences appear when extrapolating to fainter M_{UV} .

Simulations suggest the UVLF flattens and turns over due to suppression of faint galaxy formation by reionization. The limit at which this occurs, however, is not well known. The H_2 model of J. Jaacks et al. (2013) suggests this could occur as early as $M_{\text{UV,lim}} = -16.0$, although the DRAGONS (C. Liu et al. 2016) simulation series predict a flattening at -14 and full turnover at $-12 \lesssim M_{\text{UV}} \lesssim -10$ (P. W. Angel et al. 2016; S. J. Mutch et al. 2016; G. B. Poole et al. 2016). The CoDa II simulations also suggest that this turnover occurs at $-12 \lesssim M_{\text{UV}} \lesssim -11$ (P. Ocvirk et al. 2020; T. Dawoodbhoy et al. 2023).

The most recent strong-lensing results from the GLIMPSE survey at $z \simeq 6$ by Goolsby et al. (in prep.) suggest no turnover as faint as $M_{\text{UV,lim}} = -13.5$. Adopting this UVLF integration limit, we require $C_{\text{HII,rec}} = 8.8_{-2.5}^{+4.3}$ ($f_{\text{esc}}^{\text{LyC}} = 10\%$) or $C_{\text{HII,rec}} = 6.2_{-2.1}^{+4.1}$ (J. Chisholm et al. (2022) $f_{\text{esc}}^{\text{LyC}}$) for a fully stably ionized Universe (i.e. with $Q_{\text{HII}} = 1$ and $\dot{Q}_{\text{HII}} = 0$), corresponding to a departure from the J. M. Shull et al. (2012) model at 2.5σ and 1.8σ significance respectively. The Bayes factor, $B = \mathcal{L}_{\text{Shull+12}}/\mathcal{L}_{\text{Davies+24}}$, denoting the favourability of the F. B. Davies et al. (2024) $C_{\text{HII,rec}} = 12$ value over the J. M. Shull et al. (2012) model assuming a fixed $M_{\text{UV,lim}} = -13.5$, is measured in each case to be $\ln B = -5.36$ and $\ln B = -0.52$. The UV turnover required to favour the F. B. Davies et al. (2024) model (i.e. the limit when $\ln B = 0$) are $M_{\text{UV,lim}} > -14.2$ and $M_{\text{UV,lim}} > -12.7$.

If we were instead to assume a late-reionization model with $Q_{\text{HII}}(z = 6) = 0.7$ and retain $M_{\text{UV,lim}} = -13.5$, which remains fully consistent with direct Q_{HII} constraints (see e.g. I. D. McGreer et al. 2015; X. Jin et al. 2023; F. B. Davies et al. 2025, for dark pixel fraction constraints), we would need $C_{\text{HII,rec}} = 12.6_{-3.5}^{+6.1}$ ($f_{\text{esc}}^{\text{LyC}} = 0.1$) or $C_{\text{HII,rec}} = 8.9_{-3.1}^{+5.8}$ (J. Chisholm et al. (2022) $f_{\text{esc}}^{\text{LyC}}$), providing even more significant 2.9σ and 2.1σ deviations. This reduces the turnover limit required to favour the F. B. Davies et al. (2024) results for $M_{\text{UV,lim}} > -15.7$ and $M_{\text{UV,lim}} > -13.7$. We thus conclude a moderate favourability of the F. B. Davies et al. (2024) model except in the case of low $f_{\text{esc}}^{\text{LyC}} \lesssim 5\%$.

Table 2 additionally shows the scatter in \dot{n}_{ion} represented by $\sigma_{\log_{10} \dot{n}_{\text{ion}}}$. While it is likely that the patchiness of reionization will contribute non-negligibly, this

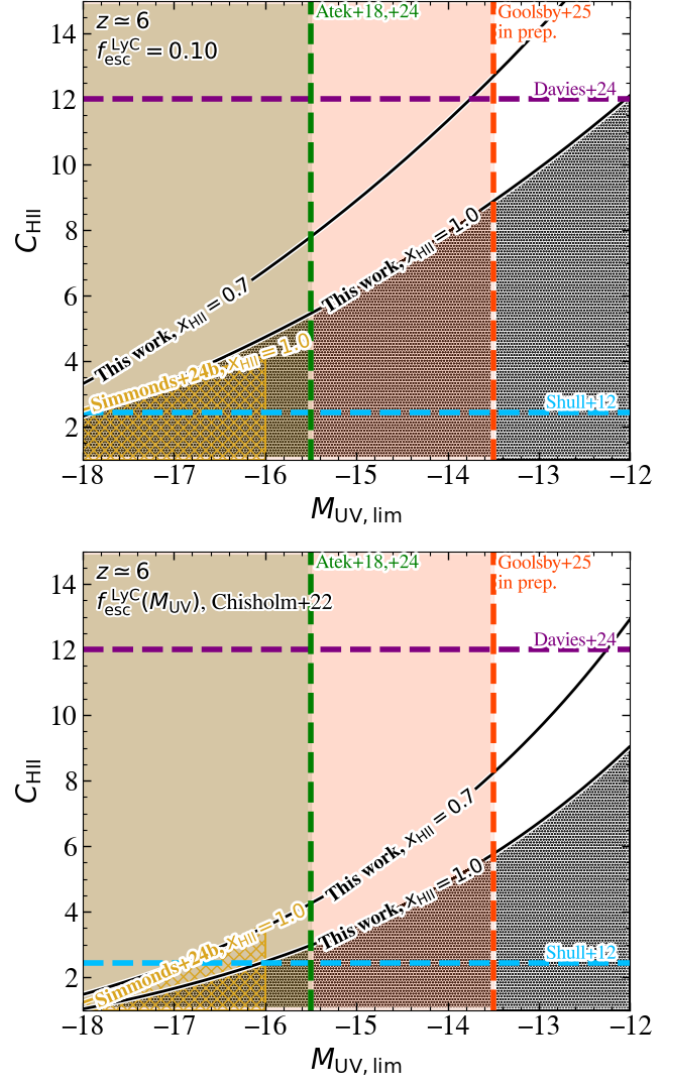


Figure 14. IGM HII clumping factor constraints as a function of UVLF turnover magnitude, $M_{\text{UV,lim}}$, at $z \simeq 6$. Clumping factor constraints from simulations by J. M. Shull et al. (2012) (light blue) and F. B. Davies et al. (2024) (purple), and approximate observational $M_{\text{UV,lim}}$ limits at $z \sim 6-7$ by H. Atek et al. 2018, 2024 (green) and are shown. x_{HII} contours showing the contribution from the full (combined) sample as well as from SFGs in our work are shown in black and blue respectively, while the full sample results from C. Simmonds et al. (2024b) is shown in yellow. **Upper panel)** Contours assume a fixed $f_{\text{esc}}^{\text{LyC}} = 10\%$. **Lower panel)** Contours assume an M_{UV} dependent $f_{\text{esc}}^{\text{LyC}}$ derived from the J. Chisholm et al. (2022) LzLCS conversion from β_{UV} .

scatter is likely instead dominated by the uncertainty in D. Calzetti et al. (2000) dust attenuation estimates determined by our SED fitting procedure. Since it remains challenging to quantify the impact of dust on our observed scatter, we do not attempt to decouple the

$f_{\text{esc}}^{\text{LyC}}$ model	$M_{\text{UV,lim}}$	$\log_{10}(\dot{n}_{\text{ion}}/\text{s}^{-1}\text{Mpc}^{-3})$	$\sigma_{\log_{10} \dot{n}_{\text{ion}}}$	$C_{\text{HII,rec}} (\dot{Q}_{\text{HII}} = 0)$		
				$Q_{\text{HII}} = 1.00$	$Q_{\text{HII}} = 0.85$	$Q_{\text{HII}} = 0.70$
10%	-17.0	$50.61^{+0.05}_{-0.05}$	+0.19 - 0.18	$3.4^{+0.4}_{-0.4}$	$4.0^{+0.5}_{-0.4}$	$4.9^{+0.6}_{-0.5}$
	-15.5	$50.82^{+0.09}_{-0.08}$	+0.20 - 0.18	$5.5^{+1.3}_{-1.0}$	$6.4^{+1.6}_{-1.1}$	$7.8^{+1.9}_{-1.4}$
	-13.5	$51.03^{+0.17}_{-0.14}$	+0.20 - 0.18	$8.8^{+4.3}_{-2.5}$	$10.4^{+5.0}_{-2.9}$	$12.6^{+6.1}_{-3.5}$
Chisholm+22	-17.0	$50.31^{+0.07}_{-0.06}$	+0.39 - 0.36	$1.7^{+0.3}_{-0.2}$	$2.0^{+0.3}_{-0.3}$	$2.4^{+0.4}_{-0.3}$
	-15.5	$50.58^{+0.13}_{-0.11}$	+0.40 - 0.37	$3.1^{+1.0}_{-0.6}$	$3.7^{+1.2}_{-0.8}$	$4.5^{+1.5}_{-0.9}$
	-13.5	$50.87^{+0.23}_{-0.20}$	+0.40 - 0.39	$6.2^{+4.1}_{-2.1}$	$7.3^{+4.8}_{-2.5}$	$8.9^{+5.8}_{-3.1}$

Table 2. \dot{n}_{ion} and $C_{\text{HII,rec}}$ values determined as the summation of star forming and smouldering $\dot{n}_{\text{ion}}-M_{\text{UV}}$ curves from Figure 12 integrated to UVLF turnover magnitudes, $M_{\text{UV,lim}} = \{-17.0, -15.5, -13.5\}$ for our fixed $f_{\text{esc}}^{\text{LyC}} = 0.1$ and J. Chisholm et al. (2022) derived $f_{\text{esc}}^{\text{LyC}}(M_{\text{UV}})$ models. The median scatter in \dot{n}_{ion} is given by $\sigma_{\log_{10} \dot{n}_{\text{ion}}}$. $C_{\text{HII,rec}}$ values are computed assuming three different H II volume filling factors $Q_{\text{HII}} = \{1.00, 0.85, 0.70\}$ consistent with more direct measurements of the neutral fraction at $z = 6$.

intrinsic scatter in IGM H II clumping from that induced by our observational methodology, and hence do not quote the observed scatter on the measurement of $C_{\text{HII,rec}}$. We note that our $\sigma_{\log_{10} \dot{n}_{\text{ion}}}$ measurements for the J. Chisholm et al. (2022) $f_{\text{esc}}^{\text{LyC}}$ model do not include the scatter in the conversion between β_{UV} and $f_{\text{esc}}^{\text{LyC}}$ within the LzLCS sample, which would add to this observed scatter.

5.3. Modelling caveats

5.3.1. Self-shielding “sinks” for ionizing photons at the end of the EoR

The reionization ODE given by Equation 11 balances the rates of hydrogen-only ionization and recombination assuming that all emitted photons escaping the ISM of their host galaxy also escape the CGM and ionize HI residing in the IGM. This approximation breaks down rapidly towards the end of reionization when the *average* mean free path of ionizing photons, $\langle\lambda_{\text{mfp}}\rangle$, rapidly increases during the epoch of ionized bubble overlap.

The source of reionization “sinks” is dominated by Lyman-Limit Systems (LLSs) with HI column densities $N_{\text{HI}} \gtrsim 10^{17}\text{cm}^{-2}$ due to their relative abundance over damped Lyman alpha systems (S. R. Furlanetto & A. Mesinger 2009; F. Haardt & P. Madau 2012; E. Sobacchi & A. Mesinger 2014). These LLSs are self-shielded, dominating the mean free path of ionizing photons; the mean opacity ($\kappa_{\nu} \propto \lambda_{\text{mfp},\nu}^{-1}$) of photons at the Lyman-limit ($\nu = \nu_{\text{L}} = 3.29 \times 10^{15}$ Hz) is thus given by $\langle\kappa_{\nu_{\text{L}}}\rangle = \langle\kappa_{\nu_{\text{L}}}^{\text{LLS}}\rangle + \langle\kappa_{\nu_{\text{L}}}^{\text{IGM}}\rangle$.

This can be used to modify the source term of the reionization ODE in Equation 11 by a factor $(1 + \langle\kappa_{\nu_{\text{L}}}^{\text{LLS}}\rangle/\langle\kappa_{\nu_{\text{L}}}^{\text{IGM}}\rangle)$ in the denominator, suppressing our inferred $C_{\text{HII,rec}}$ by the same factor (P. Madau 2017). Since $\langle\kappa_{\nu_{\text{L}}}^{\text{IGM}}\rangle \propto \langle x_{\text{HI}}\rangle$, this factor only becomes important during the end stages of the EoR when the HI content is low; it remains critically dependent on the residual HI content within ionized bubbles, estimated to be

$\langle x_{\text{HI}}\rangle \sim 10^{-4}$ at $z \simeq 6$ by observations of the Gunn-Peterson trough in SDSS quasar spectra by X. Fan et al. (2006). The $\langle\kappa_{\nu_{\text{L}}}^{\text{LLS}}\rangle$ term is dependent on the number density of LLSs, obtained by stacked quasar spectra at $z \lesssim 5.5$ (e.g. J. X. Prochaska et al. 2009; J. M. O’Meara et al. 2013; G. Worseck et al. 2014).

Combining these results yields $(1 + \langle\kappa_{\nu_{\text{L}}}^{\text{LLS}}\rangle/\langle\kappa_{\nu_{\text{L}}}^{\text{IGM}}\rangle) \sim 3$ at $z \simeq 6$, which increases with time reaching ~ 2.8 at $z \simeq 5$ and $\rightarrow \infty$ at $z \simeq 4.3$. This indicates that our inferred values for $C_{\text{HII,rec}}$ may be a factor ~ 3 overestimated; a faint UVLF turnover limit of $M_{\text{UV,lim}} \gtrsim -12.3$ would thus be required to favour the H II clumping prescription in F. B. Davies et al. (2024) over the J. M. Shull et al. (2012) model assuming $f_{\text{esc}}^{\text{LyC}} = 0.1$ and total stable reionization. We note that in the case of later reionization models with $Q_{\text{HII}}(z = 6) \neq 1$, the overlap of ionized bubbles is not sufficient to provide a notable difference in the estimated value of $C_{\text{HII,rec}}$.

5.3.2. The topology of reionization

It is important to note that as we determine the clumping factor from the timescale required to equate the photoionization and recombination rates in a stably reionized Universe with given Q_{HII} , we are specifically inferring the *recombination-averaged global* hydrogen clumping factor, defined mathematically as

$$C_{\text{HII,rec}} = \frac{\langle n_{\text{H}}^2(1 + x_{\text{He}})x_{\text{HII}}\alpha_{\text{rec}}(T_e)\rangle}{\langle n_{\text{H}}\rangle^2\langle(1 + x_{\text{He}})\rangle\langle x_{\text{HII}}\rangle\langle\alpha_{\text{rec}}(T_e)\rangle}. \quad (14)$$

Crucially, this is not equivalent to the physical clumping of the gas distribution of hydrogen, $C_{\text{H}} = \langle n_{\text{H}}^2\rangle/\langle n_{\text{H}}\rangle^2$, since it dependent upon both the inhomogeneous temperature distribution and the topology of reionization for both hydrogen and, to a lesser extent, helium.

The topology of reionization, remains critically important for inferences regarding the clumping of gas. Two plausible scenarios exist, namely “inside-out”, where the Universe reionizes hierarchically from the most to the

least-dense regions, and “outside-in”, which is exactly the opposite. Should reionization indeed be “inside-out”, the velocity of ionization fronts will be increased towards the end of the EoR as the less dense voids finish filling in, making our $dQ_{\text{HII}}/dt = 0$ assumption made between Equation 11 and Equation 13 increasingly invalid. While cosmological hydrodynamical simulations favour this “inside-out” reionization (e.g. A. H. Pawlik et al. 2009; K. Finlator et al. 2011; J. M. Shull et al. 2012; M. McQuinn et al. 2011; A. H. Pawlik et al. 2015), the pioneering work of J. Miralda-Escudé et al. (2000) strongly favours the “outside in” model where the clumping falls below unity (i.e. the gas recombines more efficiently than in an homogeneous IGM) when all gas below an overdensity $\Delta = \rho/\bar{\rho} \sim 10$ at $z \simeq 6$ is reionized.

The $C_{\text{HII,rec}}$ weighting in Equation 14 is made more complex by the $\alpha_{\text{rec}}(T_e) \propto T_e^{-0.7}$ temperature dependence. Since overdense regions are on average hotter (L. Hui & N. Y. Gnedin 1997), recombination timescales should be longer in these regions, favouring “inside-out” reionization and observed clumping factors. In contrast, the Jeans length temperature dependence, $\lambda_J \propto T^{1/2}$, means that the smallest mass clumps are “smoothed” out as the temperature increases, reducing $C_{\text{HII,rec}}$ in a process known as photoevaporation. Nevertheless, we note that our elevated $C_{\text{HII,rec}}$ measurements could in part be due to reionization being more “inside-out” than described by simulations.

5.3.3. Considering the reionization history

The requirement of reionization to progress over time means that our $dQ_{\text{HII}}/dt = 0$ assumption made in Equation 13 is incorrect by construction. To evaluate the impact of this on our inferred $C_{\text{HII,rec}}$ values, we compute the full integral in Equation 11 to calculate Q_{HII} at $z = 6$ on the same $\{C_{\text{HII,rec}}, M_{\text{UV,lim}}\}$ grid as plotted in Figure 14 numerically using `scipy.integrate.solve_ivp`. This takes into account the previous reionization history; we assume a starting redshift, $z_{\text{start}} = 15$, redshift independent $C_{\text{HII,rec}}$, constant IGM electron temperature $T_e = 10^4$ K. Three runs are performed assuming a different \dot{n}_{ion} redshift dependence, $d \log_{10} \dot{n}_{\text{ion}}/dz \in [0.0, -0.2, -0.4]$, consistent with the evolution presented in R. J. Bouwens et al. (2015a) and S. L. Finkelstein et al. (2019).

The $Q_{\text{HII}} = \{1.00, 0.85, 0.70\}$ contours from the numerical integration are compared to the $dQ_{\text{HII}}/dt = 0$ fiducial values to produce a correction term, $\Delta C_{\text{HII,rec}} = C_{\text{HII,rec}}^{Q_{\text{HII}} \neq 0} - C_{\text{HII,rec}}^{Q_{\text{HII}} = 0}$, to account for the reionization history, given by

$$\Delta C_{\text{HII,rec}} \simeq 19.1 \times \frac{d \log_{10} \dot{n}_{\text{ion}}}{dz} - 2.5. \quad (15)$$

Our $dQ_{\text{HII}}/dt = 0$ assumption is thus only valid for the physically unmotivated $d \log_{10} \dot{n}_{\text{ion}}/dz \simeq 0.13$. The observed $d \log_{10} \dot{n}_{\text{ion}}/dz \simeq -0.2$ from R. J. Bouwens et al. (2015a) and $d \log_{10} \dot{n}_{\text{ion}}/dz \simeq 0.0$ from S. L. Finkelstein et al. (2019) would suggest $\Delta C_{\text{HII,rec}} \simeq -6.3$ and $\Delta C_{\text{HII,rec}} \simeq -2.5$ respectively.

It is noteworthy that the clumping factor correction in Equation 15 holds only in the $C_{\text{HII,rec}} > 0$ regime where enough ionizing photons are released into the IGM cumulatively during the entire history of reionization by galaxies to produce a Universe with neutral content Q_{HII} without recombinations. A comprehensive comparison of early and late reionization models is presented in C. Cain et al. (2025).

5.3.4. The contribution by AGN

It is known that AGN provide the dominant source of ionizing photons for the HeII reionization at $z \sim 4$ and a non-negligible contribution to HI reionization (e.g. L. Y. A. Yung et al. 2021; S. Asthana et al. 2024; P. Dayal et al. 2025). In this work we have implicitly assumed that galaxies contribute 100% to hydrogen reionization; any additional contribution from AGN will increase the total $\dot{n}_{\text{ion}}^{\text{tot}} = \dot{n}_{\text{ion}}^{\text{gal}} + \dot{n}_{\text{ion}}^{\text{AGN}}$ and thus the inferred $C_{\text{HII,rec}}$ required for stable reionization. Our $C_{\text{HII,rec}}$ measurements should therefore be taken as lower limits as a result of this unknown AGN contribution.

By integrating the AGN luminosity function to determine the emissivity of LyC sources (see e.g. F. Haardt & P. Madau 2012; P. Madau & F. Haardt 2015), several studies have suggested that AGN contribute $\lesssim 10\%$ of the ionizing photon budget (e.g. G. Kulkarni et al. 2019), backed up by results from simulations, including DELPHI (P. Dayal et al. 2020; V. Mauerhofer et al. 2025) and OBELISK (M. Trebitsch et al. 2021). More recent studies, however, highlight that either an increased AGN $f_{\text{esc}}^{\text{LyC}} \gtrsim 60\%$ (P. Madau et al. 2024; J. C. J. D’Silva et al. 2025) or independent modelling of faint, Type I, unobscured AGN (M. Singha et al. 2025) could increase the contribution of AGN to more than this fiducial 10%.

Integrating the $\dot{n}_{\text{ion}}-z$ relations from G. Kulkarni et al. (2019) and J. C. J. D’Silva et al. (2025) over the redshift range used in this work ($5.6 < z < 6.5$) yields $\log_{10}(\dot{n}_{\text{ion}}^{\text{AGN}}/\text{s}^{-1}\text{Mpc}^{-3}) = 49.27 \pm 0.50$ and $\log_{10}(\dot{n}_{\text{ion}}^{\text{AGN}}/\text{s}^{-1}\text{Mpc}^{-3}) = 50.53 \pm 0.10$ $\text{s}^{-1}\text{Mpc}^{-3}$ respectively. Comparing these to our $f_{\text{esc}}^{\text{LyC}} = 0.1$, $M_{\text{UV,lim}} = -13.5$ galaxy $\dot{n}_{\text{ion}}^{\text{gal}}$ presented in Table 2 gives AGN which provide 2% (G. Kulkarni et al. 2019) and 24% (J. C. J. D’Silva et al. 2025) of the total ionizing photon budget. An increase in $C_{\text{HII,rec}}$ by factors of 1.02 and 1.32 respectively are required to increase the number of recombinations to stabilize reionization against

the increased emissivity. Should we instead relax our UVLF turnover limit to $M_{\text{UV},\text{lim}} = -17.0$, the AGN contributions ($C_{\text{HII,rec}}$ multiplicative factors) changes to 4% (1.05) for G. Kulkarni et al. (2019) and 45% (1.83) for J. C. J. D’Silva et al. (2025). It is worth noting that these fractions are lower limits due to the unknown contribution from obscured Type II AGN.

6. CONCLUSIONS

In summary, we present indirect H II clumping factor results at $5.6 < z < 6.5$ using a sample of 1721 candidate Lyman Break Galaxies (LBGs) at $5.6 < z < 6.5$ across $550^{\prime 2}$ of unmasked sky area across the JADES (GOODS-North/South), PRIMER (UDS/COSMOS), and NEP surveys collated in EPOCHS-v2 (Austin et al. in prep). We use `Bagpipes` with BPASS v2.2.1 SPS templates and a “continuity bursty” SFH with an additional 3 – 10 Myr age bin to compute $\xi_{\text{ion},0}$ and $\dot{N}_{\text{ion},0}$ for our sample, which is split by star formation burstiness, $\text{SFR}_{10}/\text{SFR}_{100}$ into star forming and smouldering subsamples. We perform a 90% stellar mass cut, with limits measured between $\log_{10}(M_{\star,\text{lim}}/M_{\odot}) \in [8.1, 9.2]$ using the JAGUAR mock catalogue.

We measure a flatter

$$\beta_{\text{UV}} = (-0.040 \pm 0.022)M_{\text{UV}} - 2.88_{-0.44}^{+0.43},$$

than measured previously with *HST* at $z \simeq 6$ (e.g. R. J. Bouwens et al. 2012), with 0.27 dex scatter. This highlights the new population of intrinsically bright, dust free sources which may leak copious amounts of LyC photons.

The ionizing photon production efficiency, $\xi_{\text{ion},0}$, is computed from the H α recombination line flux. Our `Bagpipes` models reach a maximum $\log_{10}(\xi_{\text{ion},0}/\text{Hz erg}^{-1}) = 25.75$, highlighting the limitations of SED fitting which cannot reproduce the extreme values $\log_{10}(\xi_{\text{ion},0}/\text{Hz erg}^{-1}) \gtrsim 25.8$ observed spectroscopically with JWST/NIRSpec. We find no trend of $\xi_{\text{ion},0}$ with M_{UV} , measuring

$$\log_{10}(\xi_{\text{ion},0}/\text{Hz erg}^{-1}) = -0.006_{-0.017}^{+0.019} M_{\text{UV}} + 25.05_{-0.34}^{+0.39}$$

for the full sample, consistent with canonical $\xi_{\text{ion},0} \simeq 10^{25.2} \text{ Hz erg}^{-1}$ values at $z \simeq 6$. Our SFG subsample produces results 0.1 – 0.15 dex higher. The gradient of this relation differs from recent observational results suggesting either an increasing (C. Simmonds et al. 2024a; R. Begley et al. 2025b; C. Papovich et al. 2025; M. Llerena et al. 2025) or decreasing (C. Simmonds et al. 2024b; R. Begley et al. 2025a; A. J. Pahl et al. 2025a,b) $\xi_{\text{ion},0}$ for fainter galaxies.

We calculate the $z \simeq 6$ UVLF for our combined, star forming, and smouldering samples, complete down to

$M_{\text{UV}} \simeq -18$ in the deepest regions of JADES-GOODS-South. We find results consistent with *HST* HFF and CANDELS studies, although the SFG subsample has a steeper faint-end slope ($\alpha_{\text{SF}} = -2.2 \pm 0.2$) than our smouldering sources ($\alpha_{\text{sm}} = -1.7 \pm 0.2$).

Combining our measured $\dot{N}_{\text{ion},0} - M_{\text{UV}}$ relation with our Schechter fits to the $z \simeq 6$ UVLFs, we compute the total contribution to reionization, \dot{n}_{ion} . Assuming the UVLF turnover occurs at $M_{\text{UV}} = -17$, we find $\log_{10}(\dot{n}_{\text{ion}}/\text{s}^{-1}\text{Mpc}^{-3}) = 50.31_{-0.06}^{+0.07}$ adopting the M_{UV} dependent $f_{\text{esc}}^{\text{LyC}}$ relation derived from our β_{UV} measurements, and $\log_{10}(\dot{n}_{\text{ion}}/\text{s}^{-1}\text{Mpc}^{-3}) = 50.61_{-0.05}^{+0.05}$ with fixed $f_{\text{esc}}^{\text{LyC}} = 10\%$. These results are consistent with previous JWST studies by C. Simmonds et al. (2024b).

Assuming stable reionization ($dQ_{\text{HII}}/dt = 0$), the UVLF turnover constraints from GLIMPSE (i.e. $M_{\text{UV},\text{lim}} \simeq -13.5$, Goolsby et al. in prep.) suggest a clumping factor $C_{\text{HII,rec}} = 6.2_{-2.1}^{+4.1}$ is required to fully reionize the Universe by $z \simeq 6$. If we instead assume a constant $f_{\text{esc}}^{\text{LyC}} = 10\%$, we measure $C_{\text{HII,rec}} = 8.8_{-2.5}^{+4.3}$. Clumping factors of this magnitude resolve the ionizing photon budget crisis outlined by J. B. Muñoz et al. (2024).

Our fiducial results favor the F. B. Davies et al. (2024) clumping factor measurements derived observationally from mean free path measurements in stacked quasar spectra over the more traditional J. M. Shull et al. (2012) relation at $z \simeq 6$ for UVLF turnover magnitudes $M_{\text{UV},\text{lim}} > -12.7$ ($M_{\text{UV},\text{lim}} > -14.2$ for $f_{\text{esc}}^{\text{LyC}} = 10\%$). While these are intriguing, we note that our results are sensitive to $f_{\text{esc}}^{\text{LyC}}$, x_{HI} , the contribution of self-shielded LLSs within ionized bubbles, the topology and history of reionization, and the contribution from AGN. None of these factors are well constrained and can lead to dramatically different $C_{\text{HII,rec}}$ results.

Nevertheless, our methodology paves the way for future $C_{\text{HII,rec}}$ constraints pre-overlap where more direct quasar analyses become impossible due to the saturation of the Ly α forest. Future ξ_{ion} measurements from JWST/NIRCam at $6.5 < z < 7.6$ utilizing the [O III]+H β optical emission line complex will constrain the reionization history and allow for a more robust measurement of $C_{\text{HII,rec}}$.

ACKNOWLEDGMENTS

We acknowledge support from the ERC Advanced Investigator Grant EPOCHS (788113), as well as two studentships from STFC for DA and TH. LW acknowledges funding from the Faculty of Science & Engineering at the University of Manchester. RAW, SHC, and

RAJ acknowledge support from NASA JWST Interdisciplinary Scientist grants NAG5 12460, NNX14AN10G and 80NSSC18K0200 from GSFC.

This work is based on observations made with the NASA/ESA *Hubble Space Telescope* (HST) and NASA/ESA/CSA *James Webb Space Telescope* (JWST) obtained from the *Mikulski Archive for Space Telescopes* (MAST) at the *Space Telescope Science Institute* (STScI), which is operated by the Association of Universities for Research in Astronomy, Inc., under NASA contract NAS 5-03127 for JWST, and NAS 5-26555 for HST. Some of the data products presented herein were retrieved from the Dawn JWST Archive (DJA). DJA is an initiative of the Cosmic Dawn Center, which is funded by the Danish National Research Foundation under grant No. 140. The authors thank all involved in the construction and operations of the telescope as well as those who designed and executed these observations, their number are too large to list here and without each of their continued efforts such work would not be possible.

The authors thank Anthony Holloway and Sotirios Sanidas for their providing their expertise in high performance computing and other IT support throughout this work.

AUTHOR CONTRIBUTIONS

We list here the roles and contributions of the authors according to the Contributor Roles Taxonomy (CRediT)¹⁶.

Duncan A. Austin: Conceptualization, Data curation, Formal analysis, Investigation, Methodology, Project Administration, Resources, Software, Validation, Visualization, Writing - original draft, Writing - review & editing

Thomas Harvey: Software, Writing - review & editing

Christopher J. Conselice: Funding Acquisition, Project Administration, Supervision, Writing - review & editing

Nathan J. Adams: Data curation, Resources

Vadim Rusakov: Investigation, Resources, Software

Sophie L. Newman, Louise T. C. Seeyave: Data curation, Writing - review & editing

Massimo Ricotti: Methodology, Writing - review & editing

Caio Goolsby, James Trussler, Brenda Frye, Norman A. Grogin, Rolf A. Jansen, Anton M. Koekemoer, Michael Rutkowski, Rogier A.

Windhorst: Writing - review & editing

DATA AVAILABILITY

Photometric imaging and catalogues will be made available upon reasonable request to the corresponding author.

Facilities: HST(ACS-WFC), JWST(NIRCam)

Software: astropy (Astropy Collaboration et al. 2013, 2018, 2022), CLOUDY (G. J. Ferland et al. 2013), PyMC (J. Salvatier et al. 2015), SExtractor (E. Bertin & S. Arnouts 1996)

¹⁶ <https://credit.niso.org>

APPENDIX

A. POWER LAW FITTING RESULTS

Throughout this paper we have fit power laws,

$$Y = \frac{dY}{dM_{UV}} M_{UV} + Y_0, \quad (\text{A1})$$

to produce scaling relations for $Y = \{\beta_{UV}, \xi_{ion,0}, \dot{N}_{ion,0}\}$ in terms of intrinsic UV magnitude, M_{UV} . The scatter in our relation is measured in general in terms of some normalization, σ_c , some Y -dependent scatter, σ_Y , and some M_{UV} -dependent scatter, $\sigma_{M_{UV}}$, which can be modelled as

$$\sigma(M_{UV}, Y) = |\sigma_c + Y\sigma_Y + M_{UV}\sigma_{M_{UV}}|. \quad (\text{A2})$$

For $Y = \beta_{UV}$ our errors are Gaussian, hence we include only σ_c dependence, whereas the heteroscedasticity in H α luminosity measurements prompts us to include σ_Y dependence for $Y = \xi_{ion,0}$, and both σ_Y and $\sigma_{M_{UV}}$ dependence for $Y = \dot{N}_{ion,0}$. In each case we perform Bayesian MCMC fitting using Equation A1 and Equation A2 adopting wide uniform priors using the `emcee` python package (D. Foreman-Mackey et al. 2013). We restrict the bounds of the scatter to exclude the possibility of bimodal solutions. Results for our combined, SFG and smouldering samples at $z \simeq 6$ are presented in Table 3.

Table 3. Power law fitting posteriors for our $\beta_{UV} - M_{UV}$ (Figure 8), $\xi_{ion,0} - M_{UV}$ (Figure 5), and $\dot{N}_{ion,0} - M_{UV}$ (Figure 9) relations. Here we parametrize the fit as $Y = (dY/dM_{UV})M_{UV} + Y_0$ and the scatter as $\sigma(M_{UV}, Y) = |\sigma_c + Y\sigma_Y + M_{UV}\sigma_{M_{UV}}|$

Independent variable, Y	Sample	dY/dM_{UV}	Y_0	σ_c	σ_Y	$\sigma_{M_{UV}}$
β	Total	-0.040 ± 0.022	$-2.88^{+0.43}_{-0.44}$	0.27 ± 0.02	—	—
	Star-forming	$-0.007^{+0.035}_{-0.031}$	$-2.25^{+0.70}_{-0.61}$	$0.25^{+0.05}_{-0.04}$	—	—
	Smouldering	$-0.051^{+0.025}_{-0.026}$	$-3.07^{+0.49}_{-0.50}$	0.28 ± 0.03	—	—
$\xi_{ion,0}$	Total	$-0.006^{+0.019}_{-0.017}$	$25.05^{+0.39}_{-0.34}$	$18.98^{+1.13}_{-1.07}$	$-0.754^{+0.019}_{-0.017}$	—
	Star-forming	$0.011^{+0.013}_{-0.015}$	$25.54^{+0.25}_{-0.29}$	$17.74^{+3.45}_{-3.04}$	$-0.701^{+0.120}_{-0.136}$	—
	Smouldering	-0.001 ± 0.015	$24.43^{+0.31}_{-0.30}$	$13.49^{+1.89}_{-1.83}$	$-0.556^{+0.074}_{-0.078}$	—
$\dot{N}_{ion,0}$	Total	$-0.542^{+0.047}_{-0.039}$	$43.20^{+0.96}_{-0.78}$	$34.26^{+2.30}_{-2.35}$	$-0.800^{+0.046}_{-0.044}$	$-0.444^{+0.056}_{-0.051}$
	Star-forming	$-0.417^{+0.026}_{-0.027}$	$46.02^{+0.52}_{-0.55}$	$40.94^{+4.41}_{-4.17}$	$-0.889^{+0.090}_{-0.096}$	$-0.370^{+0.048}_{-0.054}$
	Smouldering	$-0.391^{+0.049}_{-0.041}$	$45.43^{+0.92}_{-0.78}$	$25.07^{+3.76}_{-3.73}$	$-0.561^{+0.075}_{-0.077}$	$-0.235^{+0.059}_{-0.058}$

B. DETERMINING THE $\xi_{ion,0}$ SENSITIVITY LIMIT AT $5.6 < z < 6.5$

From the right hand panel in Figure 4, it is apparent that there exists some sensitivity limit below which we cannot precisely measure $\xi_{ion,0}$ from the photometric data. We investigate this limit by producing mock photometry at $5.6 < z < 6.5$ from the first realization of the JAGUAR catalogues introduced in subsection 2.6 using the same mock depths and filterset as for the mock photometry from the spectra described above. Following this, we run the catalogue through our selection criteria; we are left with 2,064 sources which are then run through `Bagpipes` to calculate $\xi_{ion,0}$ values. Results are shown in Figure 15, where we can see that 1σ and 2σ sensitivities reside at $\log_{10}(\xi_{ion,0}/\text{Hz erg}^{-1}) \simeq 25.0$ and $\log_{10}(\xi_{ion,0}/\text{Hz erg}^{-1}) \simeq 25.25$ respectively.

Taking the more conservative 2σ limit, we note that anything below $\log_{10}(\xi_{ion,0}/\text{Hz erg}^{-1}) \simeq 25.25$ can be considered an upper limit (as opposed to a lower limit due as a consequence of the larger UV continuum SNRs compared to the corresponding H α line SNRs). Further studies incorporating shallower but more sensitive narrow or medium bands at $\gtrsim 4\mu\text{m}$, for instance with the JWST Emission Line Survey (JELS; see e.g. K. J. Duncan et al. 2025; C. A. Pirie et al. 2025), will improve the $\xi_{ion,0}$ sensitivity of our measurements.

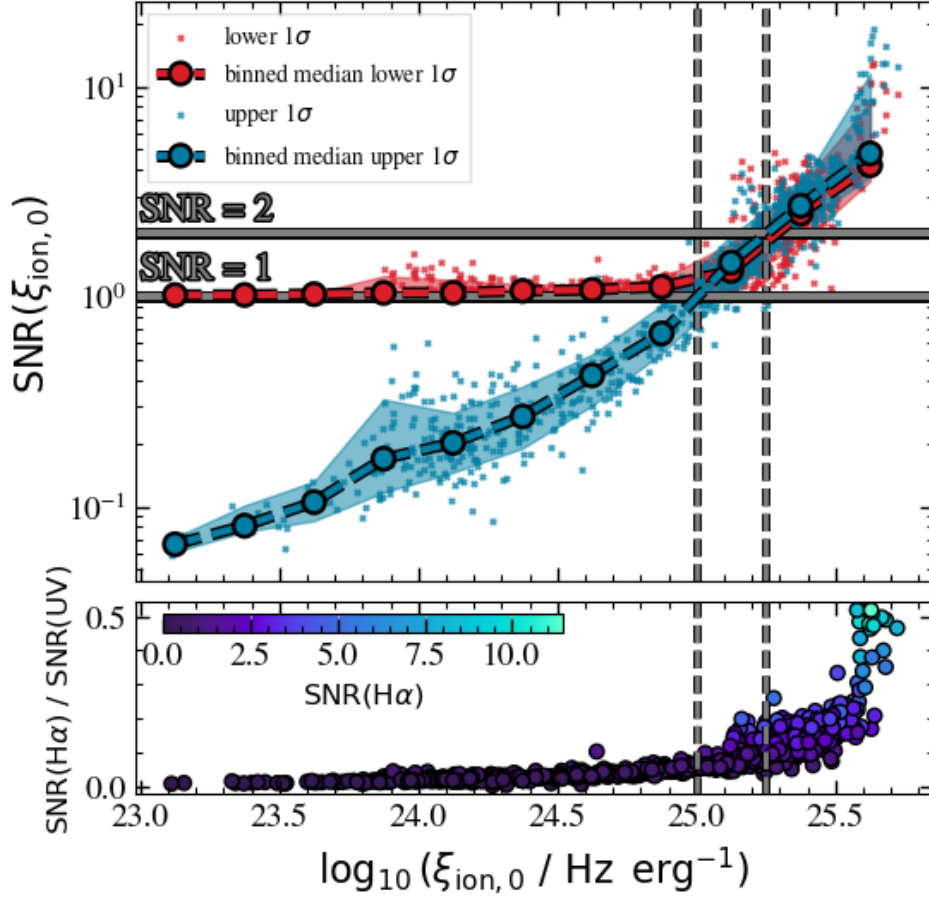


Figure 15. Limiting sensitivity of $\xi_{\text{ion},0}$ measurements at $5.6 < z < 6.5$. Vertical dashed lines show the approximate limiting 1σ ($\log_{10}(\xi_{\text{ion},0}/\text{Hz erg}^{-1}) \simeq 25.0$) and 2σ ($\log_{10}(\xi_{\text{ion},0}/\text{Hz erg}^{-1}) \simeq 25.25$) sensitivities. SNRs are calculated using the lower (red) and upper (blue) 1σ errors, where the large circular points and shaded regions show the median and $16^{\text{th}} - 84^{\text{th}}$ percentiles in 0.25 dex bins. The ratio of $\text{H}\alpha$ to UV continuum SNRs are shown in the lower inset.

C. THE EFFICIENCY OF OUR BURSTINESS SELECTION CRITERIA WITH SPECTROSCOPY

To estimate the spectroscopic burstiness values, we fit 75 NIRSpect PRISM/CLEAR spectra at $5.6 < z < 6.5$ collated from the DJA v4.2 (explained in more detail in subsection 3.2) directly with `Bagpipes` at their fixed DJA catalogued redshifts. The same fiducial prior setup as with the photometry is used and we adopt the default spectral resolution curve distributed by STScI. A comparison of photometric and spectroscopic burstiness estimates are presented in Figure 16.

We find that $35/44$ ($\simeq 80\%$) of photometrically selected star forming sources (with $\Phi > 1$) are correctly identified, compared to only $22/31$ ($\simeq 70\%$) of photometrically smouldering sources. This technique assumes, as always, that our SFH prescription adequately describes our sources, meaning these values are more likely the best-case scenario. Nevertheless, we conclude that our star forming subsample has marginally more purity, although both subsamples remain relatively interloper-free.

D. THE IMPACT OF $[\text{N II}]$ ON MEASUREMENTS OF $\xi_{\text{ion},0}$

Our conclusions in this work are dependent in part on the measured $\text{H}\alpha$ line fluxes, which are determined from the photometric boost in the F444W bandpass compared to the continuum which is traced by F410M. It is important, therefore, to determine the contribution to this F410M–F444W colour by nearby emission lines other than the $\text{H}\alpha$ recombination line. Most notable of which are the $[\text{N II}]_{\lambda 6548}$ and $[\text{N II}]_{\lambda 6584}$ collisionally excited lines arising from N^+ .

We calculate the $[\text{N II}]/\text{H}\alpha$ ratio ($[\text{N II}] \equiv [\text{N II}]_{\lambda 6548} + [\text{N II}]_{\lambda 6584}$) from mock galaxies produced by the `SYNTHESIZER` python package (C. C. Lovell et al. 2025; W. J. Roper et al. 2025) as a function of ionization parameter $\log U \in [-4, -1]$

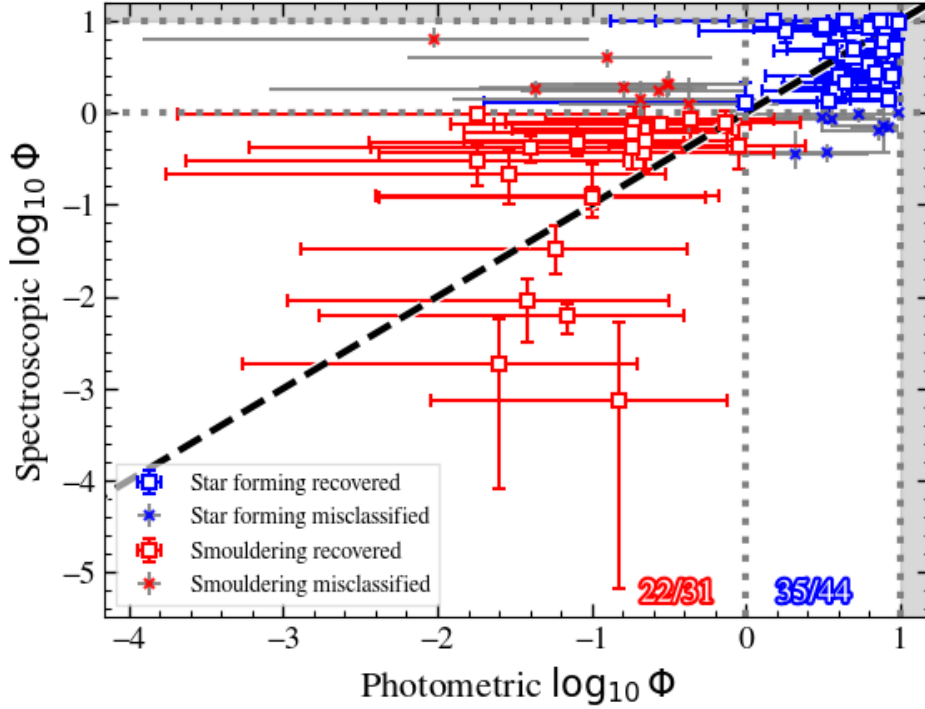


Figure 16. Comparison of photometric and spectroscopic estimates of star formation burstiness from 71 NIRSpc PRISM/CLEAR spectra at $5.6 < z < 6.5$ and via photometric and spectroscopic **Bagpipes** SED fitting. The purity of our subsamples is estimated to be $\simeq 80\%$ (star forming) and $\simeq 70\%$ (smouldering).

using the grids computed in *S. L. Newman et al. (2025)*. These models use the **BPASS-2.2.1** SPS binary star models run through **CLOUDY-v23.01** assuming a *G. Chabrier (2003)* IMF with mass limits $M_{\star} = [0.1, 300] M_{\odot}$, and are computed at fixed metallicities $\log_{10} Z \in [10^{-4}, 0.04]$ and ages 1 Myr – 1 Gyr. Results are shown in the main panel of *Figure 17*. There is a strong correlation such that high metallicity systems have larger $[\text{N II}]/\text{H}\alpha$. $[\text{N II}]/\text{H}\alpha$ falls with increasing $\log_{10} U$ in systems with subsolar metallicity which also exhibit little age dependence; at $Z = 0.04$, the $\log_{10} U$ dependence turns over in the oldest systems.

The right-hand panel in *Figure 17* shows results from G395M/F290LP medium resolution ($R \sim 1000$) grating spectra from NIRSpc. We collate 126 spectra from DJA v4.2 at $5.6 < z < 6.5$, calculating $[\text{N II}]/\text{H}\alpha$ from Gaussian fits to the emission lines using **specFitMSA**. We find $N_{\text{spec}} = \{23, 10, 3\}$ spectra with $[\text{N II}]_{\lambda 6548}$ and $[\text{N II}]_{\lambda 6584}$ detected at $\{1, 2, 3\}\sigma$. While we do not compute the ionization parameter for these sources, we find $[\text{N II}]/\text{H}\alpha = 12.7^{+2.8}_{-0.4}\%$ for the $\text{SNR}_{[\text{N II}]} > 3$ sample. Relaxing to $\text{SNR}_{[\text{N II}]} > \{2, 1\}$, we measure $\{9.1^{+5.6}_{-4.0}, 7.0^{+4.7}_{-6.4}\}\%$.

Our best-fitting **Bagpipes** templates output this $[\text{N II}]/\text{H}\alpha$ value, however not enough information is contained within the photometry to constrain this. This makes the inferred values extremely sensitive to systematics in the SED fitting process which are already substantial for measuring the much stronger $\text{H}\alpha$ line fluxes/EWs. Since what is important is how much **Bagpipes** gets this value wrong by, and these measured ratios are on average $\simeq 10\%$, we ignore the impact of this on our measured $\xi_{\text{ion},0}$.

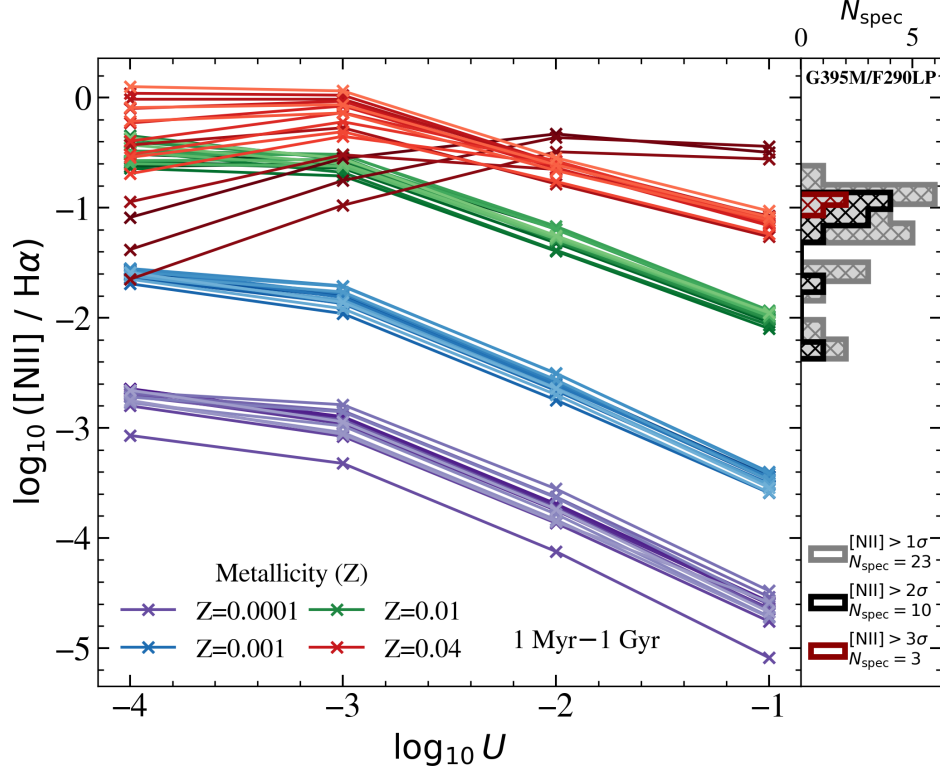


Figure 17. $[\text{NII}]/\text{H}\alpha$ ratio as a function of ionization parameter $\log_{10} U \in [-4, -1]$ for metallicities $Z \in [10^{-4}, 0.04]$ and ages 1 Myr – 1 Gyr (with darker lines showing older models) computed using SYNTHESIZER (C. C. Lovell et al. 2025; W. J. Roper et al. 2025). These models use the BPASS-2.2.1 SPS binary-star models run through CLOUDY-v23.01 assuming a G. Chabrier (2003) IMF with mass limits $M_{\star} = [0.1, 300]M_{\odot}$ following the prescription in S. L. Newman et al. (2025). The right hand panel shows observational results from JWST/NIRSpec G395M/F290LP spectra at $5.6 < z < 6.5$, $\{23, 10, 3\}$ of which have both $[\text{NII}]_{\lambda 6548}$ and $[\text{NII}]_{\lambda 6584}$ detected at $\{1, 2, 3\}\sigma$.

REFERENCES

- Adams, N. J., Conselice, C. J., Austin, D., et al. 2024, *ApJ*, 965, 169, doi: [10.3847/1538-4357/ad2a7b](https://doi.org/10.3847/1538-4357/ad2a7b)
- Adams, N. J., Austin, D., Harvey, T., et al. 2025, arXiv e-prints, arXiv:2502.10282, doi: [10.48550/arXiv.2502.10282](https://doi.org/10.48550/arXiv.2502.10282)
- Angel, P. W., Poole, G. B., Ludlow, A. D., et al. 2016, *MNRAS*, 459, 2106, doi: [10.1093/mnras/stw737](https://doi.org/10.1093/mnras/stw737)
- Asada, Y., Desprez, G., Willott, C. J., et al. 2025, *ApJL*, 983, L2, doi: [10.3847/2041-8213/adc388](https://doi.org/10.3847/2041-8213/adc388)
- Asthana, S., Haehnelt, M. G., Kulkarni, G., et al. 2024, arXiv e-prints, arXiv:2409.15453, doi: [10.48550/arXiv.2409.15453](https://doi.org/10.48550/arXiv.2409.15453)
- Astropy Collaboration, Robitaille, T. P., Tollerud, E. J., et al. 2013, *A&A*, 558, A33, doi: [10.1051/0004-6361/201322068](https://doi.org/10.1051/0004-6361/201322068)
- Astropy Collaboration, Price-Whelan, A. M., Sipőcz, B. M., et al. 2018, *AJ*, 156, 123, doi: [10.3847/1538-3881/aabc4f](https://doi.org/10.3847/1538-3881/aabc4f)
- Astropy Collaboration, Price-Whelan, A. M., Lim, P. L., et al. 2022, *ApJ*, 935, 167, doi: [10.3847/1538-4357/ac7c74](https://doi.org/10.3847/1538-4357/ac7c74)
- Atek, H., Richard, J., Kneib, J.-P., & Schaerer, D. 2018, *MNRAS*, 479, 5184, doi: [10.1093/mnras/sty1820](https://doi.org/10.1093/mnras/sty1820)
- Atek, H., Labbé, I., Furtak, L. J., et al. 2024, *Nature*, 626, 975, doi: [10.1038/s41586-024-07043-6](https://doi.org/10.1038/s41586-024-07043-6)
- Atek, H., Chisholm, J., Kokorev, V., et al. 2025, arXiv e-prints, arXiv:2511.07542, doi: [10.48550/arXiv.2511.07542](https://doi.org/10.48550/arXiv.2511.07542)
- Austin, D., Conselice, C. J., Adams, N. J., et al. 2024, arXiv e-prints, arXiv:2404.10751, doi: [10.48550/arXiv.2404.10751](https://doi.org/10.48550/arXiv.2404.10751)
- Bagley, M. B., Finkelstein, S. L., Koekemoer, A. M., et al. 2023a, *ApJL*, 946, L12, doi: [10.3847/2041-8213/acbb08](https://doi.org/10.3847/2041-8213/acbb08)
- Bagley, M. B., Pirzkal, N., Finkelstein, S. L., et al. 2023b, arXiv e-prints, arXiv:2302.05466, doi: [10.48550/arXiv.2302.05466](https://doi.org/10.48550/arXiv.2302.05466)
- Barrufet, L., Oesch, P. A., Marques-Chaves, R., et al. 2025, *MNRAS*, 537, 3453, doi: [10.1093/mnras/staf013](https://doi.org/10.1093/mnras/staf013)
- Becker, G. D., & Bolton, J. S. 2013, *MNRAS*, 436, 1023, doi: [10.1093/mnras/stt1610](https://doi.org/10.1093/mnras/stt1610)

- Becker, R. H., Fan, X., White, R. L., et al. 2001, *AJ*, 122, 2850, doi: [10.1086/324231](https://doi.org/10.1086/324231)
- Begley, R., McLure, R. J., Cullen, F., et al. 2025a, *MNRAS*, 537, 3245, doi: [10.1093/mnras/staf211](https://doi.org/10.1093/mnras/staf211)
- Begley, R., McLure, R. J., Cullen, F., et al. 2025b, arXiv e-prints, arXiv:2509.26591, doi: [10.48550/arXiv.2509.26591](https://doi.org/10.48550/arXiv.2509.26591)
- Bertin, E., & Arnouts, S. 1996, *A&AS*, 117, 393, doi: [10.1051/aas:1996164](https://doi.org/10.1051/aas:1996164)
- Bezanson, R., Labbe, I., Whitaker, K. E., et al. 2024, *ApJ*, 974, 92, doi: [10.3847/1538-4357/ad66cf](https://doi.org/10.3847/1538-4357/ad66cf)
- Bhatawdekar, R., & Conselice, C. J. 2021, *ApJ*, 909, 144, doi: [10.3847/1538-4357/abdd3f](https://doi.org/10.3847/1538-4357/abdd3f)
- Bosman, S. E. I., Davies, F. B., Becker, G. D., et al. 2022, *MNRAS*, 514, 55, doi: [10.1093/mnras/stac1046](https://doi.org/10.1093/mnras/stac1046)
- Boulade, O., Charlot, X., Abbon, P., et al. 2003, in *Society of Photo-Optical Instrumentation Engineers (SPIE) Conference Series*, Vol. 4841, Instrument Design and Performance for Optical/Infrared Ground-based Telescopes, ed. M. Iye & A. F. M. Moorwood, 72–81, doi: [10.1117/12.459890](https://doi.org/10.1117/12.459890)
- Bouwens, R. J., Illingworth, G. D., Oesch, P. A., et al. 2015a, *ApJ*, 811, 140, doi: [10.1088/0004-637X/811/2/140](https://doi.org/10.1088/0004-637X/811/2/140)
- Bouwens, R. J., Oesch, P. A., Illingworth, G. D., Ellis, R. S., & Stefanon, M. 2017, *ApJ*, 843, 129, doi: [10.3847/1538-4357/aa70a4](https://doi.org/10.3847/1538-4357/aa70a4)
- Bouwens, R. J., Smit, R., Labbé, I., et al. 2016, *ApJ*, 831, 176, doi: [10.3847/0004-637X/831/2/176](https://doi.org/10.3847/0004-637X/831/2/176)
- Bouwens, R. J., Illingworth, G. D., Oesch, P. A., et al. 2012, *ApJ*, 754, 83, doi: [10.1088/0004-637X/754/2/83](https://doi.org/10.1088/0004-637X/754/2/83)
- Bouwens, R. J., Illingworth, G. D., Oesch, P. A., et al. 2014, *ApJ*, 793, 115, doi: [10.1088/0004-637X/793/2/115](https://doi.org/10.1088/0004-637X/793/2/115)
- Bouwens, R. J., Illingworth, G. D., Oesch, P. A., et al. 2015b, *ApJ*, 803, 34, doi: [10.1088/0004-637X/803/1/34](https://doi.org/10.1088/0004-637X/803/1/34)
- Bouwens, R. J., Oesch, P. A., Stefanon, M., et al. 2021, arXiv e-prints, arXiv:2102.07775, <https://arxiv.org/abs/2102.07775>
- Bowler, R. A., Dunlop, J. S., McLure, R. J., & McLeod, D. J. 2017, *MNRAS*, 466, 3612, doi: [10.1093/mnras/stw3296](https://doi.org/10.1093/mnras/stw3296)
- Bowler, R. A., Jarvis, M. J., Dunlop, J. S., et al. 2020, *MNRAS*, 493, 2059, doi: [10.1093/mnras/staa313](https://doi.org/10.1093/mnras/staa313)
- Bowler, R. A., Dunlop, J. S., McLure, R. J., et al. 2014, *MNRAS*, 440, 2810, doi: [10.1093/mnras/stu449](https://doi.org/10.1093/mnras/stu449)
- Bowler, R. A., Dunlop, J. S., McLure, R. J., et al. 2015, *MNRAS*, 452, 1817, doi: [10.1093/mnras/stv1403](https://doi.org/10.1093/mnras/stv1403)
- Brammer, G. B., van Dokkum, P. G., & Coppi, P. 2008, *ApJ*, 686, 1503, doi: [10.1086/591786](https://doi.org/10.1086/591786)
- Bunker, A. J., Cameron, A. J., Curtis-Lake, E., et al. 2023, arXiv e-prints, arXiv:2306.02467, doi: [10.48550/arXiv.2306.02467](https://doi.org/10.48550/arXiv.2306.02467)
- Cain, C., Lopez, G., D'Aloisio, A., et al. 2025, *ApJ*, 980, 83, doi: [10.3847/1538-4357/ada152](https://doi.org/10.3847/1538-4357/ada152)
- Calzetti, D., Armus, L., Bohlin, R. C., et al. 2000, *ApJ*, 533, 682, doi: [10.1086/308692](https://doi.org/10.1086/308692)
- Calzetti, D., Kinney, A. L., & Storchi-Bergmann, T. 1994, *ApJ*, 429, 582, doi: [10.1086/174346](https://doi.org/10.1086/174346)
- Carnall, A. C., McLure, R. J., Dunlop, J. S., & Davé, R. 2018, *MNRAS*, 480, 4379, doi: [10.1093/mnras/sty2169](https://doi.org/10.1093/mnras/sty2169)
- Carnall, A. C., Cullen, F., McLure, R. J., et al. 2024, *MNRAS*, 534, 325, doi: [10.1093/mnras/stae2092](https://doi.org/10.1093/mnras/stae2092)
- Chabrier, G. 2003, *PASP*, 115, 763, doi: [10.1086/376392](https://doi.org/10.1086/376392)
- Chen, Z., Stark, D. P., Mason, C., et al. 2024, *MNRAS*, doi: [10.1093/mnras/stae455](https://doi.org/10.1093/mnras/stae455)
- Chisholm, J., Prochaska, J. X., Schaerer, D., Gazagnes, S., & Henry, A. 2020, *MNRAS*, 498, 2554, doi: [10.1093/mnras/staa2470](https://doi.org/10.1093/mnras/staa2470)
- Chisholm, J., Saldana-Lopez, A., Flury, S., et al. 2022, *MNRAS*, 517, 5104, doi: [10.1093/mnras/stac2874](https://doi.org/10.1093/mnras/stac2874)
- Choustikov, N., Stiskalek, R., Saxena, A., et al. 2025, *MNRAS*, 537, 2273, doi: [10.1093/mnras/staf126](https://doi.org/10.1093/mnras/staf126)
- Choustikov, N., Katz, H., Saxena, A., et al. 2024a, *MNRAS*, 529, 3751, doi: [10.1093/mnras/stae776](https://doi.org/10.1093/mnras/stae776)
- Choustikov, N., Katz, H., Saxena, A., et al. 2024b, *MNRAS*, 532, 2463, doi: [10.1093/mnras/stae1586](https://doi.org/10.1093/mnras/stae1586)
- Conselice, C. J., Adams, N., Harvey, T., et al. 2025, *ApJ*, 983, 30, doi: [10.3847/1538-4357/ada608](https://doi.org/10.3847/1538-4357/ada608)
- Covelo-Paz, A., Giovanazzo, E., Oesch, P. A., et al. 2025, *A&A*, 694, A178, doi: [10.1051/0004-6361/202452363](https://doi.org/10.1051/0004-6361/202452363)
- Cullen, F., McLure, R. J., McLeod, D. J., et al. 2023, *MNRAS*, 520, 14, doi: [10.1093/mnras/stad073](https://doi.org/10.1093/mnras/stad073)
- Cullen, F., McLeod, D. J., McLure, R. J., et al. 2024, *MNRAS*, 531, 997, doi: [10.1093/mnras/stae1211](https://doi.org/10.1093/mnras/stae1211)
- Davies, F. B., Bosman, S. E. I., & Furlanetto, S. R. 2024, arXiv e-prints, arXiv:2406.18186, doi: [10.48550/arXiv.2406.18186](https://doi.org/10.48550/arXiv.2406.18186)
- Davies, F. B., Bosman, S. E. I., D'Odorico, V., et al. 2025, arXiv e-prints, arXiv:2510.25829, doi: [10.48550/arXiv.2510.25829](https://doi.org/10.48550/arXiv.2510.25829)
- Dawoodbhoy, T., Shapiro, P. R., Ocvirk, P., et al. 2023, arXiv e-prints, arXiv:2302.08523, doi: [10.48550/arXiv.2302.08523](https://doi.org/10.48550/arXiv.2302.08523)
- Dayal, P., Volonteri, M., Choudhury, T. R., et al. 2020, *MNRAS*, 495, 3065, doi: [10.1093/mnras/staa1138](https://doi.org/10.1093/mnras/staa1138)
- Dayal, P., Volonteri, M., Greene, J. E., et al. 2025, *A&A*, 697, A211, doi: [10.1051/0004-6361/202449331](https://doi.org/10.1051/0004-6361/202449331)

- de Graaff, A., Brammer, G., Weibel, A., et al. 2024, arXiv e-prints, arXiv:2409.05948, doi: [10.48550/arXiv.2409.05948](https://doi.org/10.48550/arXiv.2409.05948)
- D'Eugenio, F., Cameron, A. J., Scholtz, J., et al. 2025, ApJS, 277, 4, doi: [10.3847/1538-4365/ada148](https://doi.org/10.3847/1538-4365/ada148)
- Donnan, C. T., McLeod, D. J., Dunlop, J. S., et al. 2023, MNRAS, 518, 6011, doi: [10.1093/mnras/stac3472](https://doi.org/10.1093/mnras/stac3472)
- Donnan, C. T., McLure, R. J., Dunlop, J. S., et al. 2024, arXiv e-prints, arXiv:2403.03171, doi: [10.48550/arXiv.2403.03171](https://doi.org/10.48550/arXiv.2403.03171)
- Driver, S. P., & Robotham, A. S. G. 2010, MNRAS, 407, 2131, doi: [10.1111/j.1365-2966.2010.17028.x](https://doi.org/10.1111/j.1365-2966.2010.17028.x)
- D'Silva, J. C. J., Driver, S. P., Lagos, C. D. P., et al. 2025, arXiv e-prints, arXiv:2507.16112, doi: [10.48550/arXiv.2507.16112](https://doi.org/10.48550/arXiv.2507.16112)
- Duncan, K., & Conselice, C. J. 2015, MNRAS, 451, 2030, doi: [10.1093/mnras/stv1049](https://doi.org/10.1093/mnras/stv1049)
- Duncan, K. J., McLeod, D. J., Best, P. N., et al. 2025, MNRAS, 541, 1329, doi: [10.1093/mnras/staf1061](https://doi.org/10.1093/mnras/staf1061)
- Eisenstein, D. J., Willott, C., Alberts, S., et al. 2023, arXiv e-prints, arXiv:2306.02465, doi: [10.48550/arXiv.2306.02465](https://doi.org/10.48550/arXiv.2306.02465)
- Eldridge, J. J., Stanway, E. R., Xiao, L., et al. 2017, PASA, 34, e058, doi: [10.1017/pasa.2017.51](https://doi.org/10.1017/pasa.2017.51)
- Endsley, R., Stark, D. P., Whitler, L., et al. 2024, MNRAS, 533, 1111, doi: [10.1093/mnras/stae1857](https://doi.org/10.1093/mnras/stae1857)
- Fan, X., Strauss, M. A., Richards, G. T., et al. 2006, AJ, 131, 1203, doi: [10.1086/500296](https://doi.org/10.1086/500296)
- Ferland, G. J., Porter, R. L., van Hoof, P. A. M., et al. 2013, RMxAA, 49, 137. <https://arxiv.org/abs/1302.4485>
- Ferland, G. J., Chatzikos, M., Guzmán, F., et al. 2017, RMxAA, 53, 385, doi: [10.48550/arXiv.1705.10877](https://doi.org/10.48550/arXiv.1705.10877)
- Ferrara, A. 2024, A&A, 684, A207, doi: [10.1051/0004-6361/202348321](https://doi.org/10.1051/0004-6361/202348321)
- Finkelstein, S. L., Papovich, C., Salmon, B., et al. 2012, ApJ, 756, 164, doi: [10.1088/0004-637X/756/2/164](https://doi.org/10.1088/0004-637X/756/2/164)
- Finkelstein, S. L., Ryan, R. E., Papovich, C., et al. 2015, ApJ, 810, 71, doi: [10.1088/0004-637X/810/1/71](https://doi.org/10.1088/0004-637X/810/1/71)
- Finkelstein, S. L., D'Aloisio, A., Paardekooper, J.-P., et al. 2019, ApJ, 879, 36, doi: [10.3847/1538-4357/ab1ea8](https://doi.org/10.3847/1538-4357/ab1ea8)
- Finlator, K., Davé, R., & Özel, F. 2011, ApJ, 743, 169, doi: [10.1088/0004-637X/743/2/169](https://doi.org/10.1088/0004-637X/743/2/169)
- Flury, S. R., Jaskot, A. E., Ferguson, H. C., et al. 2022a, ApJS, 260, 1, doi: [10.3847/1538-4365/ac5331](https://doi.org/10.3847/1538-4365/ac5331)
- Flury, S. R., Jaskot, A. E., Ferguson, H. C., et al. 2022b, ApJ, 930, 126, doi: [10.3847/1538-4357/ac61e4](https://doi.org/10.3847/1538-4357/ac61e4)
- Foreman-Mackey, D., Hogg, D. W., Lang, D., & Goodman, J. 2013, PASP, 125, 306, doi: [10.1086/670067](https://doi.org/10.1086/670067)
- Furlanetto, S. R., & Mesinger, A. 2009, MNRAS, 394, 1667, doi: [10.1111/j.1365-2966.2009.14449.x](https://doi.org/10.1111/j.1365-2966.2009.14449.x)
- Gaikwad, P., Haehnelt, M. G., Davies, F. B., et al. 2023, MNRAS, 525, 4093, doi: [10.1093/mnras/stad2566](https://doi.org/10.1093/mnras/stad2566)
- Gazagnes, S., Chisholm, J., Schaerer, D., Verhamme, A., & Izotov, Y. 2020, A&A, 639, A85, doi: [10.1051/0004-6361/202038096](https://doi.org/10.1051/0004-6361/202038096)
- Gnedin, N. Y., & Madau, P. 2022, Living Reviews in Computational Astrophysics, 8, 3, doi: [10.1007/s41115-022-00015-5](https://doi.org/10.1007/s41115-022-00015-5)
- Greene, J. E., Labbe, I., Goulding, A. D., et al. 2024, ApJ, 964, 39, doi: [10.3847/1538-4357/ad1e5f](https://doi.org/10.3847/1538-4357/ad1e5f)
- Grogin, N. A., Kocevski, D. D., Faber, S. M., et al. 2011, ApJS, 197, 35, doi: [10.1088/0067-0049/197/2/35](https://doi.org/10.1088/0067-0049/197/2/35)
- Gunn, J. E., & Peterson, B. A. 1965, ApJ, 142, 1633, doi: [10.1086/148444](https://doi.org/10.1086/148444)
- Haardt, F., & Madau, P. 2012, ApJ, 746, 125, doi: [10.1088/0004-637X/746/2/125](https://doi.org/10.1088/0004-637X/746/2/125)
- Hainline, K. N., Johnson, B. D., Robertson, B., et al. 2024, ApJ, 964, 71, doi: [10.3847/1538-4357/ad1ee4](https://doi.org/10.3847/1538-4357/ad1ee4)
- Harikane, Y., Ouchi, M., Shibuya, T., et al. 2018, ApJ, 859, 84, doi: [10.3847/1538-4357/aabd80](https://doi.org/10.3847/1538-4357/aabd80)
- Harikane, Y., Ono, Y., Ouchi, M., et al. 2021, arXiv e-prints, arXiv:2108.01090. <https://arxiv.org/abs/2108.01090>
- Harikane, Y., Ouchi, M., Oguri, M., et al. 2023, ApJS, 265, 5, doi: [10.3847/1538-4365/acaaa9](https://doi.org/10.3847/1538-4365/acaaa9)
- Harvey, T., Conselice, C. J., Adams, N. J., et al. 2025, ApJ, 978, 89, doi: [10.3847/1538-4357/ad8c29](https://doi.org/10.3847/1538-4357/ad8c29)
- He, C.-C., Ricotti, M., & Geen, S. 2020, MNRAS, 492, 4858, doi: [10.1093/mnras/staa165](https://doi.org/10.1093/mnras/staa165)
- Henry, A., Berg, D. A., Scarlata, C., Verhamme, A., & Erb, D. 2018, ApJ, 855, 96, doi: [10.3847/1538-4357/aab099](https://doi.org/10.3847/1538-4357/aab099)
- Hopkins, P. F., Wetzel, A., Kereš, D., et al. 2018, MNRAS, 480, 800, doi: [10.1093/mnras/sty1690](https://doi.org/10.1093/mnras/sty1690)
- Hui, L., & Gnedin, N. Y. 1997, MNRAS, 292, 27, doi: [10.1093/mnras/292.1.27](https://doi.org/10.1093/mnras/292.1.27)
- Illingworth, G., Magee, D., Bouwens, R., et al. 2016, arXiv e-prints, arXiv:1606.00841, doi: [10.48550/arXiv.1606.00841](https://doi.org/10.48550/arXiv.1606.00841)
- Inoue, A. K., Shimizu, I., Iwata, I., & Tanaka, M. 2014, MNRAS, 442, 1805, doi: [10.1093/mnras/stu936](https://doi.org/10.1093/mnras/stu936)
- Izotov, Y. I., Guseva, N. G., Fricke, K. J., et al. 2021, A&A, 646, A138, doi: [10.1051/0004-6361/202039772](https://doi.org/10.1051/0004-6361/202039772)
- Izotov, Y. I., Schaerer, D., Worseck, G., et al. 2018a, MNRAS, 474, 4514, doi: [10.1093/mnras/stx3115](https://doi.org/10.1093/mnras/stx3115)
- Izotov, Y. I., Schaerer, D., Worseck, G., et al. 2020, MNRAS, 491, 468, doi: [10.1093/mnras/stz3041](https://doi.org/10.1093/mnras/stz3041)
- Izotov, Y. I., Worseck, G., Schaerer, D., et al. 2018b, MNRAS, 478, 4851, doi: [10.1093/mnras/sty1378](https://doi.org/10.1093/mnras/sty1378)
- Jaacks, J., Thompson, R., & Nagamine, K. 2013, ApJ, 766, 94, doi: [10.1088/0004-637X/766/2/94](https://doi.org/10.1088/0004-637X/766/2/94)

- Jansen, R. A., & Windhorst, R. A. 2018, *PASP*, 130, 124001, doi: [10.1088/1538-3873/aae476](https://doi.org/10.1088/1538-3873/aae476)
- Jaskot, A. E., & Oey, M. S. 2013, *ApJ*, 766, 91, doi: [10.1088/0004-637X/766/2/91](https://doi.org/10.1088/0004-637X/766/2/91)
- Jaskot, A. E., Silveyra, A. C., Plantinga, A., et al. 2024a, *ApJ*, 972, 92, doi: [10.3847/1538-4357/ad58b9](https://doi.org/10.3847/1538-4357/ad58b9)
- Jaskot, A. E., Silveyra, A. C., Plantinga, A., et al. 2024b, *ApJ*, 973, 111, doi: [10.3847/1538-4357/ad5557](https://doi.org/10.3847/1538-4357/ad5557)
- Jiang, D., Jiang, L., Sun, S., Liu, W., & Fu, S. 2025, arXiv e-prints, arXiv:2502.03683, doi: [10.48550/arXiv.2502.03683](https://doi.org/10.48550/arXiv.2502.03683)
- Jin, X., Yang, J., Fan, X., et al. 2023, *ApJ*, 942, 59, doi: [10.3847/1538-4357/aca678](https://doi.org/10.3847/1538-4357/aca678)
- Karalidi, T., Marley, M., Fortney, J. J., et al. 2021, *ApJ*, 923, 269, doi: [10.3847/1538-4357/ac3140](https://doi.org/10.3847/1538-4357/ac3140)
- Katz, H., Ďurovčiková, D., Kimm, T., et al. 2020, *MNRAS*, 498, 164, doi: [10.1093/mnras/staa2355](https://doi.org/10.1093/mnras/staa2355)
- Katz, H., Garel, T., Rosdahl, J., et al. 2022, *MNRAS*, 515, 4265, doi: [10.1093/mnras/stac1437](https://doi.org/10.1093/mnras/stac1437)
- Katz, H., Saxena, A., Rosdahl, J., et al. 2023a, *MNRAS*, 518, 270, doi: [10.1093/mnras/stac3019](https://doi.org/10.1093/mnras/stac3019)
- Katz, H., Rosdahl, J., Kimm, T., et al. 2023b, *The Open Journal of Astrophysics*, 6, 44, doi: [10.21105/astro.2309.03269](https://doi.org/10.21105/astro.2309.03269)
- Keating, L. C., Bolton, J. S., Cullen, F., et al. 2024, *MNRAS*, 532, 1646, doi: [10.1093/mnras/stae1530](https://doi.org/10.1093/mnras/stae1530)
- Keating, L. C., Weinberger, L. H., Kulkarni, G., et al. 2020, *MNRAS*, 491, 1736, doi: [10.1093/mnras/stz3083](https://doi.org/10.1093/mnras/stz3083)
- Kennicutt, Jr., R. C. 1998, *ARA&A*, 36, 189, doi: [10.1146/annurev.astro.36.1.189](https://doi.org/10.1146/annurev.astro.36.1.189)
- Koekemoer, A. M., Faber, S. M., Ferguson, H. C., et al. 2011, *ApJS*, 197, 36, doi: [10.1088/0067-0049/197/2/36](https://doi.org/10.1088/0067-0049/197/2/36)
- Kokorev, V., Caputi, K. I., Greene, J. E., et al. 2024, arXiv e-prints, arXiv:2401.09981, doi: [10.48550/arXiv.2401.09981](https://doi.org/10.48550/arXiv.2401.09981)
- Komiyama, Y., Obuchi, Y., Nakaya, H., et al. 2018, *PASJ*, 70, S2, doi: [10.1093/pasj/psx069](https://doi.org/10.1093/pasj/psx069)
- Kriek, M., Shapley, A. E., Reddy, N. A., et al. 2015, *ApJS*, 218, 15, doi: [10.1088/0067-0049/218/2/15](https://doi.org/10.1088/0067-0049/218/2/15)
- Kron, R. G. 1980, *ApJS*, 43, 305, doi: [10.1086/190669](https://doi.org/10.1086/190669)
- Kroupa, P. 2001, *MNRAS*, 322, 231, doi: [10.1046/j.1365-8711.2001.04022.x](https://doi.org/10.1046/j.1365-8711.2001.04022.x)
- Kulkarni, G., Worseck, G., & Hennawi, J. F. 2019, *MNRAS*, 488, 1035, doi: [10.1093/mnras/stz1493](https://doi.org/10.1093/mnras/stz1493)
- Lambrides, E., Garofali, K., Larson, R., et al. 2024, arXiv e-prints, arXiv:2409.13047, doi: [10.48550/arXiv.2409.13047](https://doi.org/10.48550/arXiv.2409.13047)
- Larson, R. L., Hutchison, T. A., Bagley, M., et al. 2023, *ApJ*, 958, 141, doi: [10.3847/1538-4357/acfed4](https://doi.org/10.3847/1538-4357/acfed4)
- Leja, J., Carnall, A. C., Johnson, B. D., Conroy, C., & Speagle, J. S. 2019, *ApJ*, 876, 3, doi: [10.3847/1538-4357/ab133c](https://doi.org/10.3847/1538-4357/ab133c)
- Lin, X., Egami, E., Sun, F., et al. 2025, arXiv e-prints, arXiv:2504.08028, doi: [10.48550/arXiv.2504.08028](https://doi.org/10.48550/arXiv.2504.08028)
- Liu, C., Mutch, S. J., Angel, P. W., et al. 2016, *MNRAS*, 462, 235, doi: [10.1093/mnras/stw1015](https://doi.org/10.1093/mnras/stw1015)
- Livermore, R. C., Finkelstein, S. L., & Lotz, J. M. 2017, *ApJ*, 835, 113, doi: [10.3847/1538-4357/835/2/113](https://doi.org/10.3847/1538-4357/835/2/113)
- Llerena, M., Pentericci, L., Napolitano, L., et al. 2025, *A&A*, 698, A302, doi: [10.1051/0004-6361/202453251](https://doi.org/10.1051/0004-6361/202453251)
- Lovell, C. C., Roper, W. J., Vijayan, A. P., et al. 2025, *The Open Journal of Astrophysics*, 8, 152, doi: [10.33232/001c.145766](https://doi.org/10.33232/001c.145766)
- Lovell, C. C., Vijayan, A. P., Thomas, P. A., et al. 2021, *MNRAS*, 500, 2127, doi: [10.1093/mnras/staa3360](https://doi.org/10.1093/mnras/staa3360)
- Madau, P. 2017, *ApJ*, 851, 50, doi: [10.3847/1538-4357/aa9715](https://doi.org/10.3847/1538-4357/aa9715)
- Madau, P., Giallongo, E., Grazian, A., & Haardt, F. 2024, *ApJ*, 971, 75, doi: [10.3847/1538-4357/ad5ce8](https://doi.org/10.3847/1538-4357/ad5ce8)
- Madau, P., & Haardt, F. 2015, *ApJL*, 813, L8, doi: [10.1088/2041-8205/813/1/L8](https://doi.org/10.1088/2041-8205/813/1/L8)
- Madau, P., Haardt, F., & Rees, M. J. 1999, *ApJ*, 514, 648, doi: [10.1086/306975](https://doi.org/10.1086/306975)
- Maiolino, R., Scholtz, J., Curtis-Lake, E., et al. 2024, *A&A*, 691, A145, doi: [10.1051/0004-6361/202347640](https://doi.org/10.1051/0004-6361/202347640)
- Marley, M., Saumon, D., Morley, C., et al. 2021, Zenodo, doi: [10.5281/zenodo.5063476](https://doi.org/10.5281/zenodo.5063476)
- Maseda, M. V., Bacon, R., Lam, D., et al. 2020, *MNRAS*, 493, 5120, doi: [10.1093/mnras/staa622](https://doi.org/10.1093/mnras/staa622)
- Maseda, M. V., de Graaff, A., Franx, M., et al. 2024, *A&A*, 689, A73, doi: [10.1051/0004-6361/202449914](https://doi.org/10.1051/0004-6361/202449914)
- Mason, C. A., Naidu, R. P., Tacchella, S., & Leja, J. 2019, *MNRAS*, 489, 2669, doi: [10.1093/mnras/stz2291](https://doi.org/10.1093/mnras/stz2291)
- Mason, C. A., Trenti, M., & Treu, T. 2015, *ApJ*, 813, 21, doi: [10.1088/0004-637X/813/1/21](https://doi.org/10.1088/0004-637X/813/1/21)
- Matthee, J., Sobral, D., Best, P., et al. 2017, *MNRAS*, 465, 3637, doi: [10.1093/mnras/stw2973](https://doi.org/10.1093/mnras/stw2973)
- Mauerhofer, V., Dayal, P., Haehnelt, M. G., et al. 2025, *A&A*, 696, A157, doi: [10.1051/0004-6361/202554042](https://doi.org/10.1051/0004-6361/202554042)
- McCracken, H. J., Milvang-Jensen, B., Dunlop, J., et al. 2012, *A&A*, 544, A156, doi: [10.1051/0004-6361/201219507](https://doi.org/10.1051/0004-6361/201219507)
- McGreer, I. D., Mesinger, A., & D'Odorico, V. 2015, *MNRAS*, 447, 499, doi: [10.1093/mnras/stu2449](https://doi.org/10.1093/mnras/stu2449)
- McLeod, D. J., McLure, R. J., & Dunlop, J. S. 2016, *MNRAS*, 459, 3812, doi: [10.1093/mnras/stw904](https://doi.org/10.1093/mnras/stw904)
- McLeod, D. J., McLure, R. J., Dunlop, J. S., et al. 2015, *MNRAS*, 450, 3032, doi: [10.1093/mnras/stv780](https://doi.org/10.1093/mnras/stv780)

- McLeod, D. J., Donnan, C. T., McLure, R. J., et al. 2024, *MNRAS*, 527, 5004, doi: [10.1093/mnras/stad3471](https://doi.org/10.1093/mnras/stad3471)
- McQuinn, M., Oh, S. P., & Faucher-Giguère, C.-A. 2011, *ApJ*, 743, 82, doi: [10.1088/0004-637X/743/1/82](https://doi.org/10.1088/0004-637X/743/1/82)
- Meisner, A. M., Schneider, A. C., Burgasser, A. J., et al. 2021, *ApJ*, 915, 120, doi: [10.3847/1538-4357/ac013c](https://doi.org/10.3847/1538-4357/ac013c)
- Meurer, G. R., Heckman, T. M., & Calzetti, D. 1999, *ApJ*, 521, 64, doi: [10.1086/307523](https://doi.org/10.1086/307523)
- Miralda-Escudé, J., Haehnelt, M., & Rees, M. J. 2000, *ApJ*, 530, 1, doi: [10.1086/308330](https://doi.org/10.1086/308330)
- Miyazaki, S., Komiyama, Y., Kawanomoto, S., et al. 2018, *PASJ*, 70, S1, doi: [10.1093/pasj/psx063](https://doi.org/10.1093/pasj/psx063)
- Morley, C. V., Mukherjee, S., Marley, M. S., et al. 2024, *ApJ*, 975, 59, doi: [10.3847/1538-4357/ad71d5](https://doi.org/10.3847/1538-4357/ad71d5)
- Moster, B. P., Somerville, R. S., Newman, J. A., & Rix, H.-W. 2011, *ApJ*, 731, 113, doi: [10.1088/0004-637X/731/2/113](https://doi.org/10.1088/0004-637X/731/2/113)
- Muñoz, J. B., Mirocha, J., Chisholm, J., Furlanetto, S. R., & Mason, C. 2024, *MNRAS*, 535, L37, doi: [10.1093/mnras/slac086](https://doi.org/10.1093/mnras/slac086)
- Mukherjee, S., Fortney, J. J., Morley, C. V., et al. 2024, *ApJ*, 963, 73, doi: [10.3847/1538-4357/ad18c2](https://doi.org/10.3847/1538-4357/ad18c2)
- Mutch, S. J., Geil, P. M., Poole, G. B., et al. 2016, *MNRAS*, 462, 250, doi: [10.1093/mnras/stw1506](https://doi.org/10.1093/mnras/stw1506)
- Naidu, R. P., Tacchella, S., Mason, C. A., et al. 2020, *ApJ*, 892, 109, doi: [10.3847/1538-4357/ab7cc9](https://doi.org/10.3847/1538-4357/ab7cc9)
- Nakajima, K., Ellis, R. S., Iwata, I., et al. 2016, *ApJL*, 831, L9, doi: [10.3847/2041-8205/831/1/L9](https://doi.org/10.3847/2041-8205/831/1/L9)
- Nakajima, K., & Ouchi, M. 2014, *MNRAS*, 442, 900, doi: [10.1093/mnras/stu902](https://doi.org/10.1093/mnras/stu902)
- Nanayakkara, T., Glazebrook, K., Schreiber, C., et al. 2025, *ApJ*, 981, 78, doi: [10.3847/1538-4357/ada6ac](https://doi.org/10.3847/1538-4357/ada6ac)
- Newman, S. L., Lovell, C. C., Maraston, C., et al. 2025, *MNRAS*, doi: [10.1093/mnras/staf1866](https://doi.org/10.1093/mnras/staf1866)
- O'Brien, R., Jansen, R. A., Grogin, N. A., et al. 2024, arXiv e-prints, arXiv:2401.04944, doi: [10.48550/arXiv.2401.04944](https://doi.org/10.48550/arXiv.2401.04944)
- Ocvirk, P., Aubert, D., Sorce, J. G., et al. 2020, *MNRAS*, 496, 4087, doi: [10.1093/mnras/staa1266](https://doi.org/10.1093/mnras/staa1266)
- Oesch, P. A., Bouwens, R. J., Illingworth, G. D., Labbé, I., & Stefanon, M. 2018, *ApJ*, 855, 105, doi: [10.3847/1538-4357/aab03f](https://doi.org/10.3847/1538-4357/aab03f)
- Oesch, P. A., Bouwens, R. J., Illingworth, G. D., et al. 2014, *ApJ*, 786, 108, doi: [10.1088/0004-637X/786/2/108](https://doi.org/10.1088/0004-637X/786/2/108)
- Oesch, P. A., Brammer, G., Naidu, R. P., et al. 2023, *MNRAS*, 525, 2864, doi: [10.1093/mnras/stad2411](https://doi.org/10.1093/mnras/stad2411)
- Oke, J. B. 1974, *ApJS*, 27, 21, doi: [10.1086/190287](https://doi.org/10.1086/190287)
- Oke, J. B., & Gunn, J. E. 1983, *ApJ*, 266, 713, doi: [10.1086/160817](https://doi.org/10.1086/160817)
- O'Meara, J. M., Prochaska, J. X., Worseck, G., Chen, H.-W., & Madau, P. 2013, *ApJ*, 765, 137, doi: [10.1088/0004-637X/765/2/137](https://doi.org/10.1088/0004-637X/765/2/137)
- Osterbrock, D. E., & Ferland, G. J. 2006, *Astrophysics of gaseous nebulae and active galactic nuclei*
- Pahl, A. J., Shapley, A., Steidel, C. C., Chen, Y., & Reddy, N. A. 2021, *MNRAS*, 505, 2447, doi: [10.1093/mnras/stab1374](https://doi.org/10.1093/mnras/stab1374)
- Pahl, A. J., Topping, M. W., Shapley, A., et al. 2025a, *ApJ*, 981, 134, doi: [10.3847/1538-4357/adb1ab](https://doi.org/10.3847/1538-4357/adb1ab)
- Pahl, A. J., Shapley, A., Reddy, N. A., et al. 2025b, arXiv e-prints, arXiv:2510.12177, doi: [10.48550/arXiv.2510.12177](https://doi.org/10.48550/arXiv.2510.12177)
- Papovich, C., Cole, J. W., Hu, W., et al. 2025, arXiv e-prints, arXiv:2505.08870, doi: [10.48550/arXiv.2505.08870](https://doi.org/10.48550/arXiv.2505.08870)
- Pawlik, A. H., Schaye, J., & Dalla Vecchia, C. 2015, *MNRAS*, 451, 1586, doi: [10.1093/mnras/stv976](https://doi.org/10.1093/mnras/stv976)
- Pawlik, A. H., Schaye, J., & van Scherpenzeel, E. 2009, *MNRAS*, 394, 1812, doi: [10.1111/j.1365-2966.2009.14486.x](https://doi.org/10.1111/j.1365-2966.2009.14486.x)
- Perrin, M. D., Sivaramakrishnan, A., Lajoie, C.-P., et al. 2014, in *Society of Photo-Optical Instrumentation Engineers (SPIE) Conference Series*, Vol. 9143, *Space Telescopes and Instrumentation 2014: Optical, Infrared, and Millimeter Wave*, ed. J. Oschmann, Jacobus M., M. Clampin, G. G. Fazio, & H. A. MacEwen, 91433X, doi: [10.1117/12.2056689](https://doi.org/10.1117/12.2056689)
- Perrin, M. D., Soummer, R., Elliott, E. M., Lallo, M. D., & Sivaramakrishnan, A. 2012, in *Society of Photo-Optical Instrumentation Engineers (SPIE) Conference Series*, Vol. 8442, *Space Telescopes and Instrumentation 2012: Optical, Infrared, and Millimeter Wave*, ed. M. C. Clampin, G. G. Fazio, H. A. MacEwen, & J. Oschmann, Jacobus M., 84423D, doi: [10.1117/12.925230](https://doi.org/10.1117/12.925230)
- Pirie, C. A., Best, P. N., Duncan, K. J., et al. 2025, *MNRAS*, 541, 1348, doi: [10.1093/mnras/staf1006](https://doi.org/10.1093/mnras/staf1006)
- Planck Collaboration, Aghanim, N., Akrami, Y., et al. 2020, *A&A*, 641, A6, doi: [10.1051/0004-6361/201833910](https://doi.org/10.1051/0004-6361/201833910)
- Poole, G. B., Angel, P. W., Mutch, S. J., et al. 2016, *MNRAS*, 459, 3025, doi: [10.1093/mnras/stw674](https://doi.org/10.1093/mnras/stw674)
- Prieto-Lyon, G., Strait, V., Mason, C. A., et al. 2023, *A&A*, 672, A186, doi: [10.1051/0004-6361/202245532](https://doi.org/10.1051/0004-6361/202245532)
- Prochaska, J. X., Worseck, G., & O'Meara, J. M. 2009, *ApJL*, 705, L113, doi: [10.1088/0004-637X/705/2/L113](https://doi.org/10.1088/0004-637X/705/2/L113)
- Reddy, N. A., Oesch, P. A., Bouwens, R. J., et al. 2018, *ApJ*, 853, 56, doi: [10.3847/1538-4357/aaa3e7](https://doi.org/10.3847/1538-4357/aaa3e7)
- Ricotti, M. 2002, *MNRAS*, 336, L33, doi: [10.1046/j.1365-8711.2002.05990.x](https://doi.org/10.1046/j.1365-8711.2002.05990.x)

- Robertson, B. E., Furlanetto, S. R., Schneider, E., et al. 2013, *ApJ*, 768, 71, doi: [10.1088/0004-637X/768/1/71](https://doi.org/10.1088/0004-637X/768/1/71)
- Roper, W. J., Lovell, C., Vijayan, A., et al. 2025, arXiv e-prints, arXiv:2506.15811, doi: [10.48550/arXiv.2506.15811](https://doi.org/10.48550/arXiv.2506.15811)
- Rosdahl, J., Katz, H., Blaizot, J., et al. 2018, *MNRAS*, 479, 994, doi: [10.1093/mnras/sty1655](https://doi.org/10.1093/mnras/sty1655)
- Rosdahl, J., Blaizot, J., Katz, H., et al. 2022, *MNRAS*, 515, 2386, doi: [10.1093/mnras/stac1942](https://doi.org/10.1093/mnras/stac1942)
- Rowan-Robinson, M. 1968, *MNRAS*, 138, 445, doi: [10.1093/mnras/138.4.445](https://doi.org/10.1093/mnras/138.4.445)
- Salvatier, J., Wiecki, T., & Fonnesbeck, C. 2015, Probabilistic Programming in Python using PyMC, <https://arxiv.org/abs/1507.08050>
- Saxena, A., Bunker, A. J., Jones, G. C., et al. 2024, *A&A*, 684, A84, doi: [10.1051/0004-6361/202347132](https://doi.org/10.1051/0004-6361/202347132)
- Schechter, P. 1976, *ApJ*, 203, 297, doi: [10.1086/154079](https://doi.org/10.1086/154079)
- Schmidt, M. 1968, *ApJ*, 151, 393, doi: [10.1086/149446](https://doi.org/10.1086/149446)
- Seeyave, L. T. C., Wilkins, S. M., Kuusisto, J. K., et al. 2023, *MNRAS*, 525, 2422, doi: [10.1093/mnras/stad2487](https://doi.org/10.1093/mnras/stad2487)
- Shivaei, I., Reddy, N. A., Siana, B., et al. 2018, *ApJ*, 855, 42, doi: [10.3847/1538-4357/aaad62](https://doi.org/10.3847/1538-4357/aaad62)
- Shull, J. M., Harness, A., Trenti, M., & Smith, B. D. 2012, *ApJ*, 747, 100, doi: [10.1088/0004-637X/747/2/100](https://doi.org/10.1088/0004-637X/747/2/100)
- Simmonds, C., Tacchella, S., Hainline, K., et al. 2024a, *MNRAS*, 527, 6139, doi: [10.1093/mnras/stad3605](https://doi.org/10.1093/mnras/stad3605)
- Simmonds, C., Tacchella, S., Hainline, K., et al. 2024b, *MNRAS*, 535, 2998, doi: [10.1093/mnras/stae2537](https://doi.org/10.1093/mnras/stae2537)
- Singha, M., Malhotra, S., & Ely Rhoads, J. 2025, arXiv e-prints, arXiv:2510.26990, <https://arxiv.org/abs/2510.26990>
- Sobacchi, E., & Mesinger, A. 2014, *MNRAS*, 440, 1662, doi: [10.1093/mnras/stu377](https://doi.org/10.1093/mnras/stu377)
- Stanway, E. R., & Eldridge, J. J. 2018, *MNRAS*, 479, 75, doi: [10.1093/mnras/sty1353](https://doi.org/10.1093/mnras/sty1353)
- Stefanon, M., Bouwens, R. J., Illingworth, G. D., et al. 2022, *ApJ*, 935, 94, doi: [10.3847/1538-4357/ac7e44](https://doi.org/10.3847/1538-4357/ac7e44)
- Steidel, C. C., Bogosavljević, M., Shapley, A. E., et al. 2018, *ApJ*, 869, 123, doi: [10.3847/1538-4357/aaed28](https://doi.org/10.3847/1538-4357/aaed28)
- Tacchella, S., Finkelstein, S. L., Bagley, M., et al. 2022, *ApJ*, 927, 170, doi: [10.3847/1538-4357/ac4cad](https://doi.org/10.3847/1538-4357/ac4cad)
- Tang, M., Stark, D. P., Chevillard, J., & Charlot, S. 2019, *MNRAS*, 489, 2572, doi: [10.1093/mnras/stz2236](https://doi.org/10.1093/mnras/stz2236)
- Topping, M. W., Stark, D. P., Endsley, R., et al. 2024, *MNRAS*, 529, 4087, doi: [10.1093/mnras/stae800](https://doi.org/10.1093/mnras/stae800)
- Trebitsch, M., Dubois, Y., Volonteri, M., et al. 2021, *A&A*, 653, A154, doi: [10.1051/0004-6361/202037698](https://doi.org/10.1051/0004-6361/202037698)
- Trussler, J. A. A., Conselice, C. J., Adams, N., et al. 2024, *MNRAS*, 527, 11627, doi: [10.1093/mnras/stad3877](https://doi.org/10.1093/mnras/stad3877)
- Ulm, K. 1990, *American journal of epidemiology*, 131, 373
- Vanzella, E., Claeysens, A., Welch, B., et al. 2023, *ApJ*, 945, 53, doi: [10.3847/1538-4357/acb59a](https://doi.org/10.3847/1538-4357/acb59a)
- Verhamme, A., Orlitová, I., Schaerer, D., & Hayes, M. 2015, *A&A*, 578, A7, doi: [10.1051/0004-6361/201423978](https://doi.org/10.1051/0004-6361/201423978)
- Verhamme, A., Orlitová, I., Schaerer, D., et al. 2017, *A&A*, 597, A13, doi: [10.1051/0004-6361/201629264](https://doi.org/10.1051/0004-6361/201629264)
- Vijayan, A. P., Lovell, C. C., Wilkins, S. M., et al. 2021, *MNRAS*, 501, 3289, doi: [10.1093/mnras/staa3715](https://doi.org/10.1093/mnras/staa3715)
- Wang, B., Heckman, T. M., Amorín, R., et al. 2021, *ApJ*, 916, 3, doi: [10.3847/1538-4357/ac0434](https://doi.org/10.3847/1538-4357/ac0434)
- Wang, F., Yang, J., Fan, X., et al. 2019, *ApJ*, 884, 30, doi: [10.3847/1538-4357/ab2be5](https://doi.org/10.3847/1538-4357/ab2be5)
- Whitaker, K. E., Ashas, M., Illingworth, G., et al. 2019, *ApJS*, 244, 16, doi: [10.3847/1538-4365/ab3853](https://doi.org/10.3847/1538-4365/ab3853)
- Wilkins, S. M., Vijayan, A. P., Lovell, C. C., et al. 2023, *MNRAS*, 519, 3118, doi: [10.1093/mnras/stac3280](https://doi.org/10.1093/mnras/stac3280)
- Williams, C. C., Curtis-Lake, E., Hainline, K. N., et al. 2018, *ApJS*, 236, 33, doi: [10.3847/1538-4365/aabcb](https://doi.org/10.3847/1538-4365/aabcb)
- Windhorst, R. A., Cohen, S. H., Jansen, R. A., et al. 2023, *AJ*, 165, 13, doi: [10.3847/1538-3881/aca163](https://doi.org/10.3847/1538-3881/aca163)
- Worseck, G., Prochaska, J. X., O'Meara, J. M., et al. 2014, *MNRAS*, 445, 1745, doi: [10.1093/mnras/stu1827](https://doi.org/10.1093/mnras/stu1827)
- Wyithe, J. S. B., & Loeb, A. 2002, *ApJ*, 581, 886, doi: [10.1086/344249](https://doi.org/10.1086/344249)
- Xu, X., Henry, A., Heckman, T., et al. 2022, *ApJ*, 933, 202, doi: [10.3847/1538-4357/ac7225](https://doi.org/10.3847/1538-4357/ac7225)
- Yang, J., Wang, F., Fan, X., et al. 2020, *ApJL*, 897, L14, doi: [10.3847/2041-8213/ab9c26](https://doi.org/10.3847/2041-8213/ab9c26)
- Yung, L. Y. A., Somerville, R. S., Finkelstein, S. L., et al. 2021, *MNRAS*, 508, 2706, doi: [10.1093/mnras/stab2761](https://doi.org/10.1093/mnras/stab2761)
- Zackrisson, E., Inoue, A. K., & Jensen, H. 2013, *ApJ*, 777, 39, doi: [10.1088/0004-637X/777/1/39](https://doi.org/10.1088/0004-637X/777/1/39)
- Zehavi, I., Zheng, Z., Weinberg, D. H., et al. 2011, *ApJ*, 736, 59, doi: [10.1088/0004-637X/736/1/59](https://doi.org/10.1088/0004-637X/736/1/59)
- Zhu, Y., Becker, G. D., Bosman, S. E. I., et al. 2024, *MNRAS*, 533, L49, doi: [10.1093/mnras/lsae061](https://doi.org/10.1093/mnras/lsae061)
- Ziparo, F., Ferrara, A., Sommovigo, L., & Kohandel, M. 2023, *MNRAS*, 520, 2445, doi: [10.1093/mnras/stad125](https://doi.org/10.1093/mnras/stad125)